LNL-INFN (REP) 97/95

CRYSTAL STORAGE RING

Conceptual Design Report

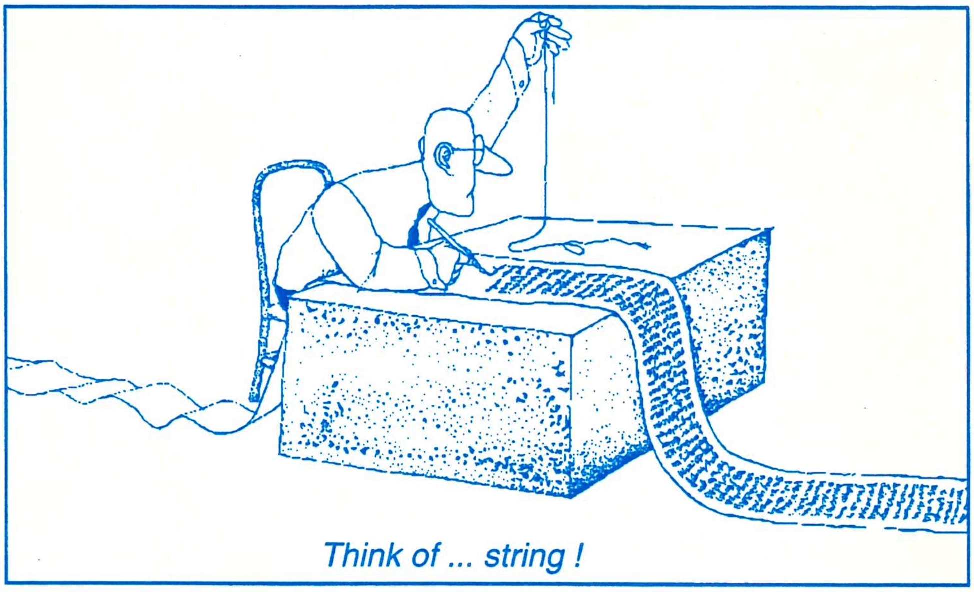

Think of ... string !

ISTITUTO NAZIONALE DI FISICA NUCLEARE
LABORATORI NAZIONALI DI LEGNARO

Via Romea, 4 I-35020 Legnaro (Padova)

LNL-INFN (REP) 97/95

CRYSTAL STORAGE RING

Conceptual Design Report

ISTITUTO NAZIONALE DI FISICA NUCLEARE
LABORATORI NAZIONALI DI LEGNARO

Via Romea, 4 I-35020 Legnaro (Padova)

The following persons have contributed to the Conceptual Design Report of the CRYSTAL Storage Ring:

G. Bisoffi	INFN-LNL
A. Burov	BINP-Novosibirsk
R. Calabrese	INFN and University of Ferrara
G. Ciullo	INFN-LNL
T. Clauser	INFN and University of Bari
A. Dainelli	INFN-LNL
N.S. Dikansky	BINP-Novosibirsk
G. Di Massa	INFN and University of Napoli
M. Fedotov	BINP-Novosibirsk
M. Greiser	MPI-Heidelberg
B. Grishanov	BINP-Novosibirsk
V. Guidi	INFN and University of Ferrara
S. Gustafsson	INFN-LNL
I. Hofmann	GSI-Darmstadt
G. Lamanna	INFN-LNL and PROEL Tecnologie
P. Lenisa	INFN and University of Ferrara
E. Mariotti	University of Siena and INFN-Pisa
F. Masoli	INFN and University of Ferrara
M.R. Masullo	INFN-Napoli
L. Moi	University of Siena and INFN-Pisa
M.F. Moisio	INFN-LNL
V. Parkhomchuk	BINP-Novosibirsk
D.V. Pestrikov	BINP-Novosibirsk
F. Petrucci	INFN and University of Ferrara
M. Pilati	INFN-LNL and University of Ferrara
A. Pisent	INFN-LNL
M. Poggi	INFN-LNL
M. Rutigliano	INFN and University of Bari
V. Shamovsky	BINP-Novosibirsk
A. Sharapa	BINP-Novosibirsk
A. Shemyakin	BINP-Novosibirsk
V. Stagno	INFN and University of Bari
U. Tambini	INFN and University of Ferrara
L. Tecchio	INFN and University of Torino
B. Tiveron	INFN-LNL
V.G. Vaccaro	INFN and University of Napoli
V. Variale	INFN-Bari
B. Yang	INFN-LNL and PROEL Tecnologie

CONTENTS

Introduction

The Conceptual Design Report of the low-energy heavy-ion storage ring, called CRYSTAL, proposed for a experimental demonstration of Crystalline Beams is here presented. Respect the Feasibility Study done in 1994 [LNL-INFN (REP) 80/94], it represents a deepen investigation on the technical aspects of the storage ring. A more realistic design of the magnetic lattice and some improvements of the proposed cooling system are shown.

The design of the project (*Fig. 1*) has been optimized for the study of crystalline beams; but provisions have also been made for carrying out experiments of different nature in nuclear, atomic and molecular physics. The Tandem-ALPI heavy-ion facility of the Laboratori Nazionali di Legnaro is assumed as injector for the storage ring. For the Crystalline mode the possibility to inject particles from an independent low energy source is also considered.

The storage ring has a circumference of *70 meters*, small enough to be installed in an experimental building located in proximity of the ALPI area (*Fig. 2*), and yet large enough to allow a maximum magnetic rigidity of *3.8 Tm*. It has a periodicity of eight, made of eight dipole magnets surrounded by quadrupole doublets, sextupoles and a *3.4 meters* long drift space free of magnets. A summary of the major parameters for Crystalline Beams is given in *Table 1*.

The existence of stable ground states for Crystalline Beams has been demonstrated by computer simulations. The basic structures are the helices and twisted multiplets. The ground state configuration depends on the focusing parameters of the storage ring. The transition thresholds from one ground state to another depend on the focusing parameters and the particles density. Since simulations demand a large amount of computing time, the possibility to obtain a phase transition from the hot beam to a Crystalline Beam is carried out for low

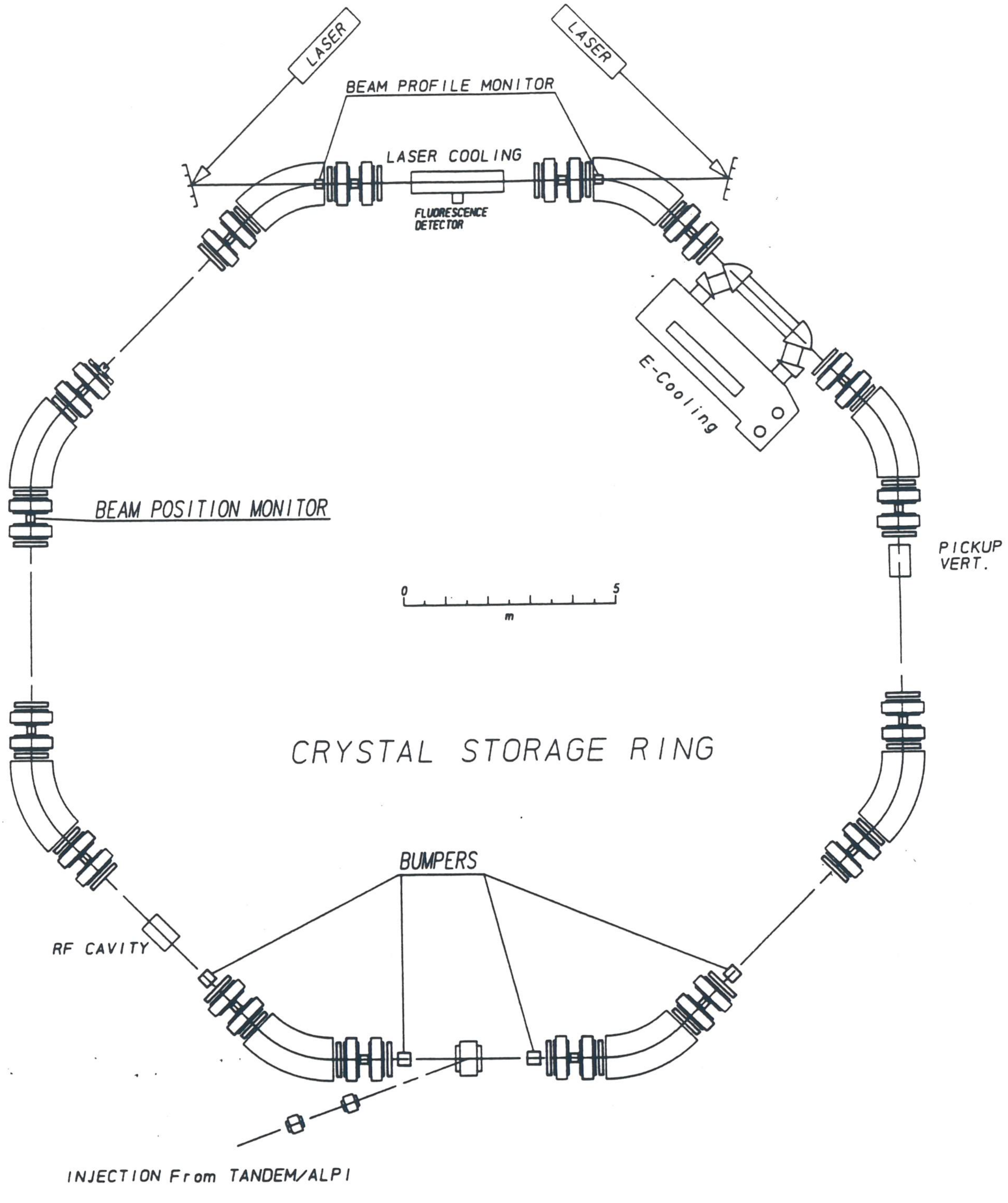

Fig. 1 - Layout of the CRYSTAL Storage Ring.

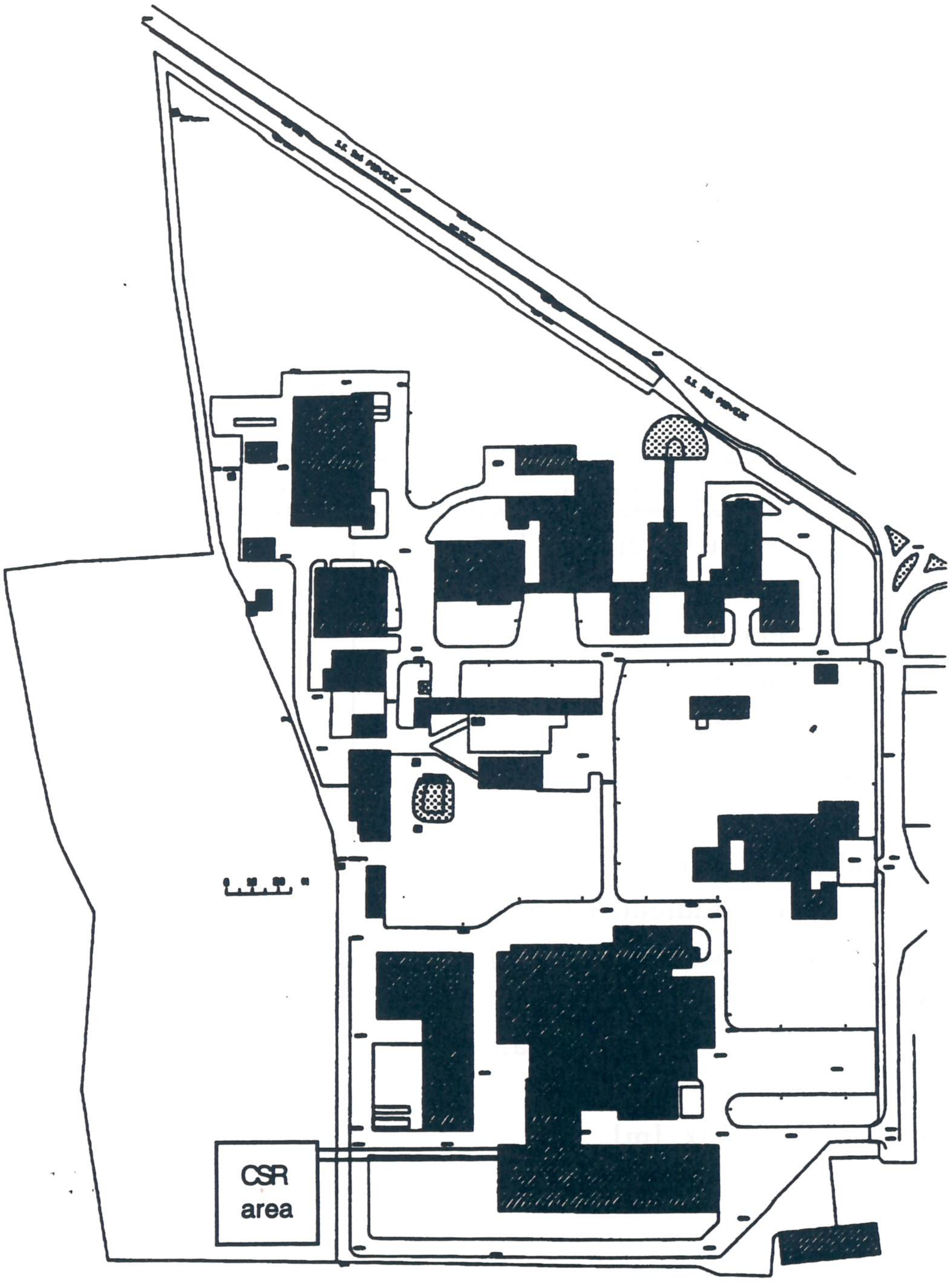

Fig. 2 - The CRYSTAL Storage Ring on the LNL Site.

density beams. Realistic simulations for phase transitions to crystalline state can be done for simple structures such as string and zig-zag (double string). The demonstration of Crystalline Beams is feasible with very effective electron and laser cooling and requires dedicated diagnostics. In the following only Lithium, Beryllium and Magnesium ions, that can be cooled with laser, will be considered for the study of Crystalline Beams.

Table 1 - Lattice Parameters of CRYSTAL Storage Ring.

Description	Crystalline Mode
Max. Magnetic Rigidity [Tm]	3.8
Circumference [m]	68.8
Lattice Periodicity	8
Bending Radius [m]	2.55
Max. Dipole Field [T]	1.5
Dipole Vertical Gap [cm]	8
Quadrupole Gradient [T/m]	0.72
Quadrupole Bore Radius [cm]	6.5
Sextupole Gradient [T/m^{-2}]	5.41
Sextupole Bore Radius [cm]	6.5
Phase Advance per Period:	
Horizontal	83^0
Vertical	53^0
Dispersion max [m]	3.6
Gamma Transition	1.76
Betatron Tunes:	
Q_h	1.85
Q_v	1.185
Natural Chromaticity:	
ξ_h	-0.72
ξ_v	0.21
Momentum Compaction	0.32

The unique feature of the CSR which makes it quite different from storage rings of similar size is an optimization of the ring parameters in order achieve the crystallization phase with the minimum possible cooling performance. In that sense the CSR will indeed be a storage ring dedicated to these studies, The research on Crystalline Beams is quite recent, hence the other storage rings were not optimized for them. The rest of the CSR research program, with applications of different nature, will complement in range and performance the existing facilities.

The construction of the project is foreseen to take a period of *five* years, from the beginning of *1997*, and has a total cost of *28 billions* of Italian Lire (quotation May 1995).

1

The Physics of Crystalline Beams

1.1 Introduction

After the successful exploitation of several heavy ion storage rings with electron cooling, the possibility of generating Crystalline Ion Beams, i.e. beams with particles located at fixed positions relative to one another has gained the interest of particle accelerator physicists [SCH1].

Moreover, new cooling methods like laser cooling [HAE1], give further opportunity to reach ultra cold system of particles necessary for the state transition to the Crystalline configuration.

Crystalline Beams will give knowledge on a completely new research field, reaching new heights in precision measurements and techniques. The applicative potentialities of Crystalline Beams would justify a careful investigation on this subject.

Apart from the pioneering work performed by E.N. Dementiev *et al.* in 1980 [DEM1], only recently [STE1] some indications of longitudinal order in a storage ring has been detected, for very low intensity ion beams.

During the last decade computer simulations [RAH1, HAS1, HAS2] have been carried out and their results showed various kinds of Crystalline structures in an equally focused straight channel. The properties of Crystalline ion beam were studied both analytically and numerically in a model where the beam was considered as at rest in a pipe with longitudinally homogeneous and transversely isotropic external focusing.

The predicted Crystalline structures were experimentally achieved in a small ring-like ion trap by employing laser cooling [BIR1, WAK1].

Only recently the feasibility of Crystalline Beams in realistic storage rings had been suggested by the result of numerical simulations [BIS1, LI1], where the particle trajectory curvature and the inhomogeneity of AG focusing were taken into account in deriving the Hamiltonian [BUR1, WEI1]. This Hamiltonian was used to study the existence and properties of Crystalline Beams. Periodic ground states of a Crystalline Beam were achieved and are very similar to the ones experimentally observed in the ion traps. Other authors demonstrated [RUG1, WEI1], in an independent way, that only in an alternating gradient storage ring Crystalline Beams may exist.

In addition, it was found that crystalline structures can be created at any density if the beam energy is lower than the transition energy of the storage ring. Above transition energy the negative mass instability prevent the formation of Crystalline Beams [WEI1, RUG1]. Furthermore, since the Hamiltonian is time-dependent, the total energy of the system is not a constant of motion and heat will transfer into the system. If the cooling is insufficient the increase of temperature will influence the particle correlation and the Crystalline Beam will reach its melting point.

Numerical calculations were performed by simulation on CSR [TEC1] where the ground state of Crystalline Beams were achieved. Although applied to a specific case, simulations have a general validity and can be useful for any storage ring.

Electron and laser cooling techniques are applied to cool down the ion beams to reach Crystalline states. In spite of the viscous heating by the shear induced in the bending fields, simulations indicate that even high density Crystalline Beams can exist in a storage ring: particles undergo oscillations due to the lattice function variations (breathing), with small amplitudes for a smooth machine.

A serious limitation of transverse beam temperature, which prevent the formation of Crystalline structures, is due to two phenomena appearing in the transport of very intense ion beams: the envelope instability [HOF1] and the intrabeam scattering. Both phenomena have been numerically investigated. Simulations show that the heating of the beam due to envelope instability is even stronger than the heating from intrabeam scattering. By an independent analysis of both phenomena the required conditions to avoid envelope instability was found [HOF2]. The effect of intrabeam scattering cannot be avoided, but only compensated by the cooling and reduced by the smoothness of the lattice.

1.2 The Physics of Crystalline Beams

In the rest frame, particles in a storage ring are described by the following Hamiltonian [BUR1, WEI1]:

$$H = \frac{1}{2}\left(p_x^2 + p_y^2 + p_z^2\right) - \gamma h x p_x + g_x \frac{x^2}{2} + g_y \frac{y^2}{2} + \xi \sum_i \frac{1}{r_i}$$

where p_x, p_y and p_z are the canonical momenta and x, y, z are the coordinates of a particle. $h(\theta)=R/\rho(\theta)$ is the dimensionless curvature, θ is the azimuth (time), $g_x(\theta)=(1-k/h^2)h^2$, $g_y(\theta)=k$ are the focusing functions and r_i is the distance between particles. The last term takes into account the Coulombian interactions between particles, where

$$\xi = \frac{Z^2}{A}\frac{R^2 r_p}{d^3\beta^2\gamma^2}$$

is the dimensionless space charge parameter, r_p is the classical radius of the proton, $d=2\pi R/N$ is the inverse longitudinal density where N is the number of particles, Z and A are the ion charge and mass respectively.

In the limit of smooth approximation, the focusing functions g_x, g_y can be replaced by the correspondent betatron tunes Q_x, Q_y and the new Hamiltonian becomes time-independent:

$$H = \frac{1}{2}\left(p_x^2 + p_y^2 + p_z^2\right) - \gamma x p_z + \frac{1}{2}\left(Q_x^2 x^2 + Q_y^2 y^2\right) + \xi V$$

This Hamiltonian is positively defined only if $Q_x > \gamma$, which lead to the conclusion that Crystalline Beams can be found only in an alternating gradient storage ring operating below the transition energy [BUR1, WEI1, RUG1].

Equations of motion following from the Hamiltonian are:

$$
\begin{aligned}
x'' &= \gamma p_z - Q_x^2 x - \xi \frac{\partial V}{\partial x} \\
y'' &= -Q_y^2 y - \xi \frac{\partial V}{\partial y} \\
z' &= p_z - \gamma x \\
p' &= -\xi \frac{\partial V}{\partial z}
\end{aligned}
$$

The equilibrium positions of a particle $i(x_i = a_i, y_i = b_i, z_i = c_i)$ have to satisfy the equations of motion. In particular the third equation gives the condition with the left hand side equal to zero:

$$p_{z,i} = \gamma a_i$$

It means that, at the equilibrium, the longitudinal momentum must be proportional to the transverse displacement, this is the condition of equal revolution frequency for all the particles of the crystal. The other conditions are:

$$
\begin{aligned}
a_i &= \frac{\xi}{\left(Q_x^2 - \gamma^2\right)} \sum_{j \neq i} \frac{a_i - a_j}{r_{ij}^3} \\
b_i &= \frac{\xi}{Q_y^2} \sum_{j \neq i} \frac{b_i - b_j}{r_{ij}^3} \\
0 &= \sum_{j \neq i} \frac{c_i - c_j + i - j}{r_{ij}^3}
\end{aligned}
$$

The series are fast converging for the cases with defined symmetry. According to the case studied by Hasse and Schiffer [HAS1] we have analogous structure parameters:

$$\lambda_x = \left[\frac{3\xi}{2\left(Q_x^2 - \gamma^2\right)}\right]^{1/3}, \lambda_y = \left(\frac{3\xi}{2Q_y^2}\right)^{1/3}$$

but different in the two planes. For the case of zero curvature and isotropic focusing these parameters turn to the parameter introduced by Hasse [HAS1], as shown by simulations using the PARMT code [BOI1, STR1].

Crystallization has been simulated in a very smooth test lattice, which is a FODO channel almost equivalent to a rectilinear infinite pipe with isotropic focusing. The results listed in *Table 1.1* show the same ground state configurations as those obtained by Hasse [HAS1].

It is interesting to observe that the condition for isotropic focusing $(\lambda_x = \lambda_y)$ for isochronous particles is that $Q_x^2 - \gamma^2 = Q_y^2$, instead of $Q_x = Q_y$ as for isoenergetic particles. Both structure parameters are proportional to the linear density $1/d$, through a constant that depends on focusing, main energy and ion kind. Every Crystalline structure is defined in a domain of λ_x, λ_y, and therefore in a range of density. The extreme values (critical values) of such a range corresponds to the stability limits. The Crystalline structure in examination become unstable when a limit is reached and a new structure appears. The particles are aligned along the direction of motion at very low densities, at higher densities more complicated structures appear.

This situation is well described by numerical simulations. The simulations are mostly applied to the CRYSTAL Storage Ring (CSR) [TEC1] in the following, but they have a general validity. The main parameters of a CSR cell are listed in *Table 1.2*. The configurations achieved, projected onto the x - y, z - x and z - y planes, are shown in *Fig. 1.1a* for various linear densities. At very low linear densities the particles are strung along the z - *axis*. At higher densities a zig-zag appears in the relatively weaker focusing plane z - y. Coulomb repulsion then splits the zig-zag and a rectangular tetrahedron can be seen. This is followed first by a rhombic tetrahedron and by a twisted quadruplet.

This sequence of structures differs from the one found in the equally focusing pipe, since the structure parameters λ_x, λ_y of these two cases are different. In this case, up to a certain linear density all structures are twisted multiplets, then a first helix appears and afterwards a shell with a central string is

Table 1.1 - Simulation results for a rectilinear pipe.

Structures	Ref. [HAS1]	PARMT
STRING	$0 < \lambda < 0.709$	$0 < \lambda < 0.7$
ZIG - ZAG	$0.709 < \lambda < 0.964$	$0.73 < \lambda < 0.96$
1st HELIX	$0.964 < \lambda < 1.23$	$1.02 < \lambda < 1.35$
TETRAHEDRON	$1.23 < \lambda < 1.47$	$1.40 < \lambda < 1.51$
HELIX	$1.47 < \lambda < 1.63$	$1.56 < \lambda < 1.87$
TETRAHEDRON	$1.63 < \lambda < 2.24$	$1.92 < \lambda < 2.29$
2nd HELIX	$2.24 < \lambda < 2.52$	$2.34 < \lambda < 2.60$
HELIX	$2.52 < \lambda < 2.96$	$2.65 < \lambda < 2.96$
3nd HELIX	$2.96 < \lambda < 3.10$	$3.02 < \lambda < 3.17$
SHELL + STRING	$3.10 < \lambda < 5.70$	$3.24 < \lambda < 8.30$
2 SHELLS	$5.70 < \lambda < 9.50$	$8.37 < \lambda < 11.4$
2 SHELLS + STRING	$9.50 < \lambda < 13.0$	$11.9 < \lambda < 15.6$
3 SHELLS + STRING	$\lambda = 19.1$	$\lambda = 21.4$
4 SHELLS	$\lambda = 26.6$	$\lambda = 28.2$
6 SHELLS	$\lambda = 66.4$	$\lambda = 70.3$

observed. The dependence of the Crystalline configurations on the structure parameters λ_x,λ_y is shown in *Table 1.3*. In order to show them more clearly, the last two structures are plotted in *Fig.1.1b* as if the mantles were the plane of the drawing. The patterns of particles on the mantles are of a hexagonal order, the transverse shapes of the shells differ somewhat from ellipses.

1.2.1 Eigenmodes of a Crystalline Beam

The equations of motion connect the oscillations of each ion with the oscillations of the others and the eigenmodes of the beam are not incoherent (single-particle) but coherent.

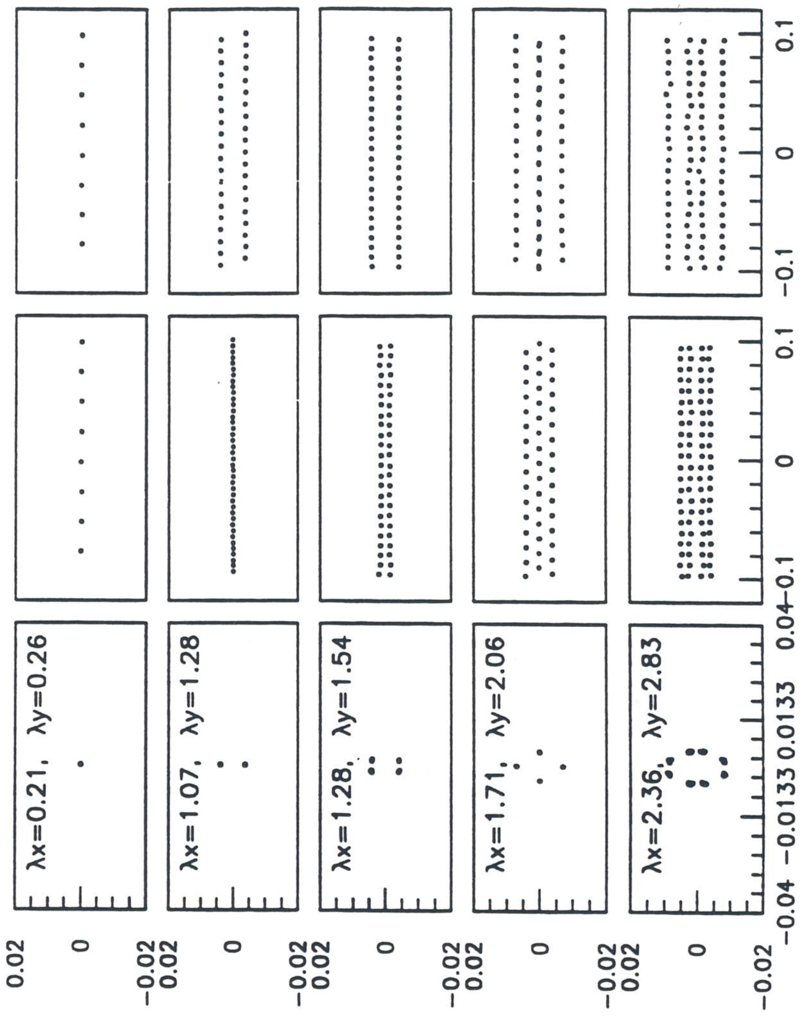

Fig. 1.1a - Crystalline configurations for different values of the structure parameters λ_x, λ_y, for $^9Be^+$ and β = *0.07*. From left to right, projection of particles onto the x - y, z - x and z - y planes are shown for five different Crystalline structures. All dimensions are in centimeters.

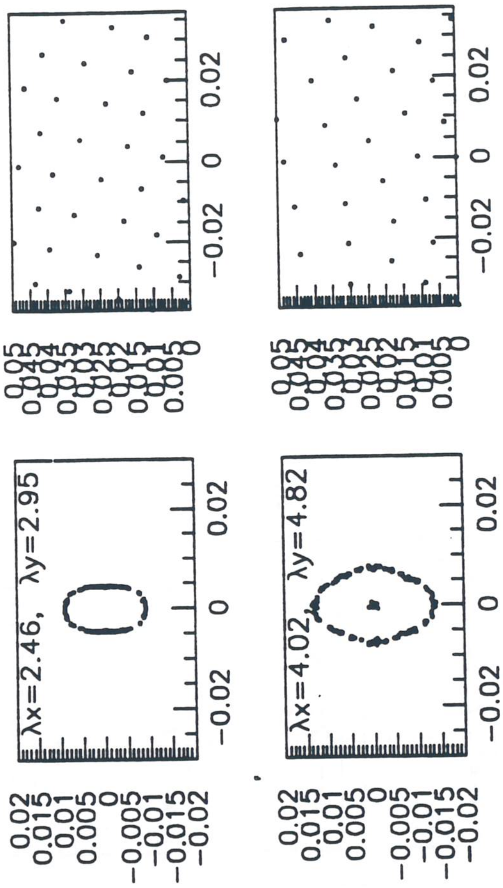

Fig. 1.1b - Crystalline configurations for different values of the structure parameters λ_x, λ_y, for $^9Be^+$ and $\beta = 0.07$. On the left is an x - y plane projection and on the right the particles from the outer shell are plotted as if the mantle were the plane of the drawing. All dimensions are in centimeters.

Table 1.2 - Main parameters of the CRYSTAL Storage Ring.

Elements of a cell	Length (m)	Strength (G/cm)
DRIFT	2.0	
QUADRUPOLE	0.25	40
DRIFT	0.40	
QUADRUPOLE	0.25	- 63
DRIFT	0.40	
SECTOR MAGNET	2.0	angle = $\pi/4$
DRIFT	0.40	
QUADRUPOLE	0.25	- 63
DRIFT	0.40	
QUADRUPOLE	0.25	40
DRIFT	2.0	
Lattice parameters		
PERIODICITY	8	
TUNES Q_x, Q_y	1.85 ; 1.185	
$(\beta_{x,y})_{max}$ (m)	8.4 ; 10.4	
DISPERSION (m)	3.6	

Table 1.3 - Crystalline structures for the CSR working point, for $^9Be^+$ and $\beta = 0.07$.

Structures	λ_x	λ_y
STRING	$0 < \lambda_x < 0.59$	$0 < \lambda_y < 0.71$
ZIG - ZAG	$0.64 < \lambda_x < 1.23$	$0.77 < \lambda_y < 1.48$
RECT. TETRA	$1.28 < \lambda_x < 1.37$	$1.54 < \lambda_y < 1.64$
RHOMB. TETRA	$1.61 < \lambda_x < 2.25$	$1.92 < \lambda_y < 2.7$
TWISTED 4-PLET	$2.33 < \lambda_x < 2.41$	$2.79 < \lambda_y < 2.89$
HELIX	$2.43 < \lambda_x < 3.64$	$2.92 < \lambda_y < 4.37$
SHELL + STRING	$4.02 < \lambda_x < 4.82$	$4.82 < \lambda_y < 5.78$

Considering small deviations $\tilde{x},\tilde{y},\tilde{z}$ around the equilibrium position (a_j,b_j,c_j) of the particles the Coulombian potential V can be linearized. In the smooth approximation, external conditions after averaging are constant along the beam, which give mutual independence of the Fourier harmonics:

$$\tilde{x}_q = \frac{1}{N}\sum_j \tilde{x}_j e^{-iqj}$$

$$\tilde{x}_j = \sum_q x_q e^{iqj}$$

with $q = 2\pi l / N$, l-integer, $|l| \leq N/2$; the same goes for the other degrees of freedom.

After this transformation equations of motion become decoupled; thus longitudinal Fourier harmonics are eigenmodes of the multiparticle system. Their dynamics is described by the following equations (subscript q is omitted):

$$\tilde{x}'' = \gamma\tilde{p}_z - Q_x^2\tilde{x} + \xi C_x\tilde{x}$$

$$\tilde{y}'' = -Q_y^2\tilde{y} + \xi C_y\tilde{y}$$

$$\tilde{p}_z'' = -\xi C_z(\tilde{p}_z - \gamma\tilde{x})$$

where:

$$C_x = 2\sum_{j\geq 1}(1-\cos(qj))\left[\frac{1}{r_j^3} - \frac{12a^2\delta_j}{r_j^5}\right]$$

$$C_x = 2\sum_{j\geq 1}(1-\cos(qj))\left[\frac{1}{r_j^3} - \frac{12b^2\delta_j}{r_j^5}\right]$$

$$C_x = 2\sum_{j\geq 1}(1-\cos(qj))\left[\frac{3j^2}{r_j^5} - \frac{1}{r_j^3}\right]$$

$$\delta_j = \begin{cases} 1, j=odd \\ 0, j=even \end{cases}$$

The eigenmodes, with frequency ν_+, ν_-, ν_ν, of coherent oscillations, in function of the wave number q, can be easily deduced from the relation dispersion. For one and two dimensional ground state structures (low density), the eigenmodes can be calculated analytically:

$$\nu_{\pm}^{2}=\frac{1}{2}\left\{Q_{x}^{2}-\xi C_{x}+\xi C_{z}\pm\left[\left(Q_{x}^{2}-\xi C_{x}+\xi C_{z}\right)^{2}-4\xi C_{z}\left(Q_{x}^{2}-\xi C_{x}-\gamma^{2}\right)\right]^{\frac{1}{2}}\right\}$$

$$\nu_{v}^{2}=Q_{y}^{2}-\xi C_{y}$$

The only approximation used in the derivation is the smooth approximation; here the contribution of longitudinal motion in coherent oscillations is taken into account as well as the oscillation of all particles in comparison to the test particle itself.

For a one-dimensional structure the constants read:

$$C_{z}/2=C_{x}=C_{y}=C_{\perp}$$

$$C_{\perp}=2\sum_{j\geq 1}\frac{1-\cos(qj)}{j^{3}}$$

which enable us to calculate the dispersion curves for the eigenmodes of a string configuration.

The string eigenfrequencies depend on the space charge parameter ξ as well as the mode factor $C_{\perp}$. This last achieves its maximum value for a wave number $q=\pi$, which corresponds to a movement of neighboring particles in opposite directions:

$$\max C_{\perp}=C_{\perp}(q=\pi)=C_{0}$$

Therefore all information about the string spectrum is contained in the frequency dependence on the space charge parameter $\nu(\xi)$ at the wave number $q=\pi$, where the space charge effect is maximum.

Far away from the zig-zag threshold when $\xi \ll \xi_{1}$ (ξ_{1} is the space charge value for the zig-zag threshold), the longitudinal mode $(+)$ corresponds to slightly shifted betatron oscillations:

$$\nu_{+}^{2}=Q_{x}^{2}-\xi C_{\perp}\left(1-\frac{2\gamma^{2}}{Q_{x}^{2}}\right);$$

while the horizontal mode *(-)* describes slow oscillations of the beam density with the frequency:

$$\nu_-^2 = 2\xi C_\perp\left(1-\frac{\gamma^2}{Q_x^2}\right).$$

From this last equation it follows that the density oscillations become unstable for $Q_x < \gamma$, in agreement with Refs. [RUG1, WEI1]. String oscillations are stable before the zig-zag threshold and become unstable (for mode $q=\pi$) just after it. In the case of dominating vertical focusing $Q_x^2-\gamma^2<Q_y^2$, the frequencies of string and zig-zag near the threshold can be found by expanding the square root in the equation of eigenmodes (mode $q=\pi$):

$$\nu_-^2 = \frac{2\left(Q_x^2-\gamma^2\right)}{2Q_x^2-\gamma^2}C_0\begin{cases}(\xi_1-\xi);\xi\le\xi_1\\(\xi-\xi_1);\xi\ge\xi_1\end{cases}$$

In the opposite situation, when $Q_x^2-\gamma^2>Q_y^2$, the zig-zag is vertical. In this case the vertical oscillation frequency goes to zero and inflects at the zig-zag origin, where $\xi=\xi_1=\frac{Q_y^2}{C_0}$:

$$\nu_v^2 = C_0\begin{cases}(\xi_1-\xi);\xi\le\xi_1\\(\xi-\xi_1);\xi\ge\xi_1\end{cases}$$

For any given betatron tunes, the point $\xi=\xi_1$ corresponds to a transition between two stable configurations, string and zig-zag. The only condition of stability for these configurations, in their own regions of space charge parameter, is that the effective mass has to be positive.

Some examples of string and zig-zag spectra for the proposed working point of the CRYSTAL Storage Ring are displayed in *Fig.1.2* and *Fig. 1.3*. More complicated structures, i.e. three-dimensional configurations, can be found only by numerical calculations.

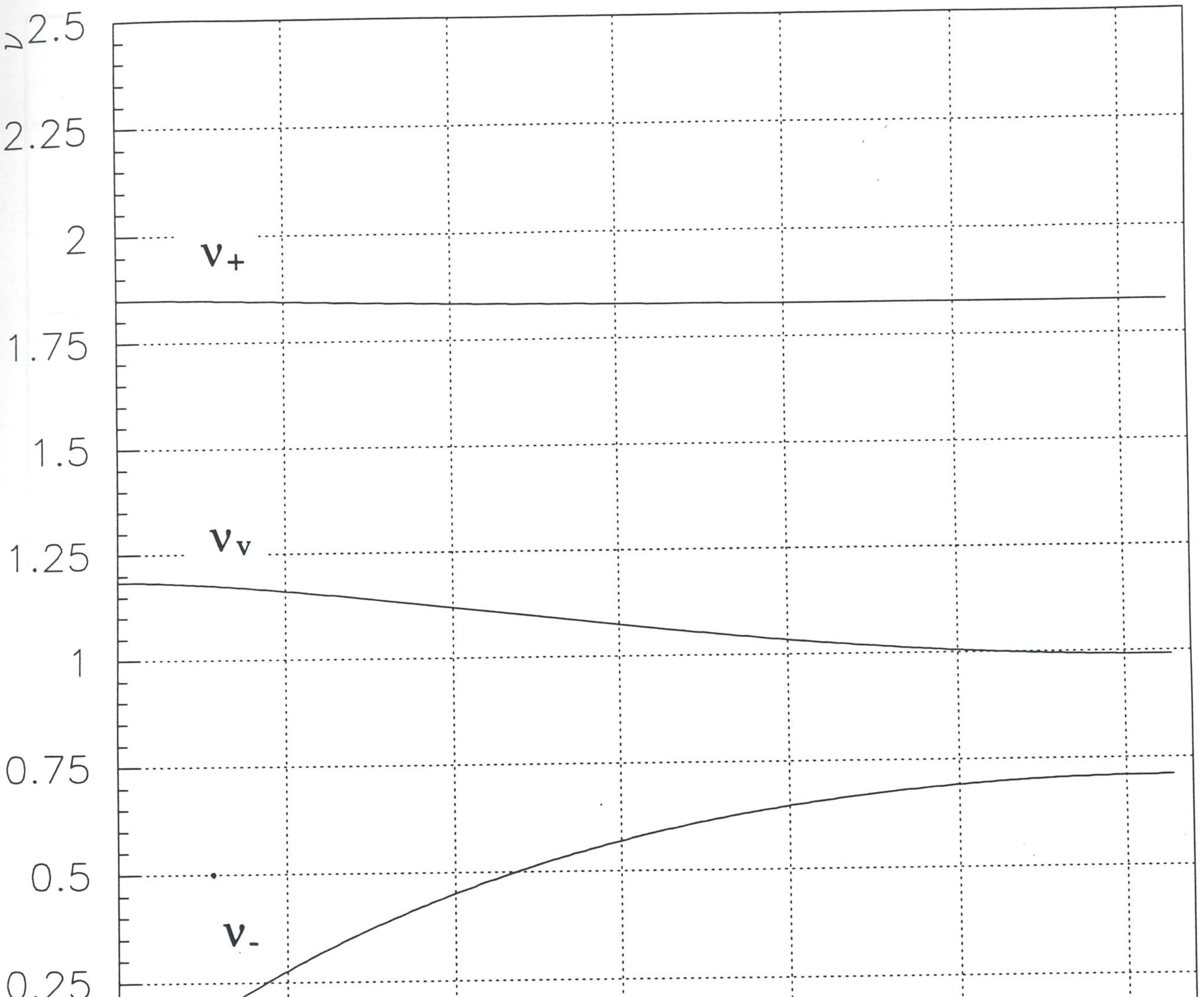

Fig. 1.2 - Coherent spectrum for a string configuration.

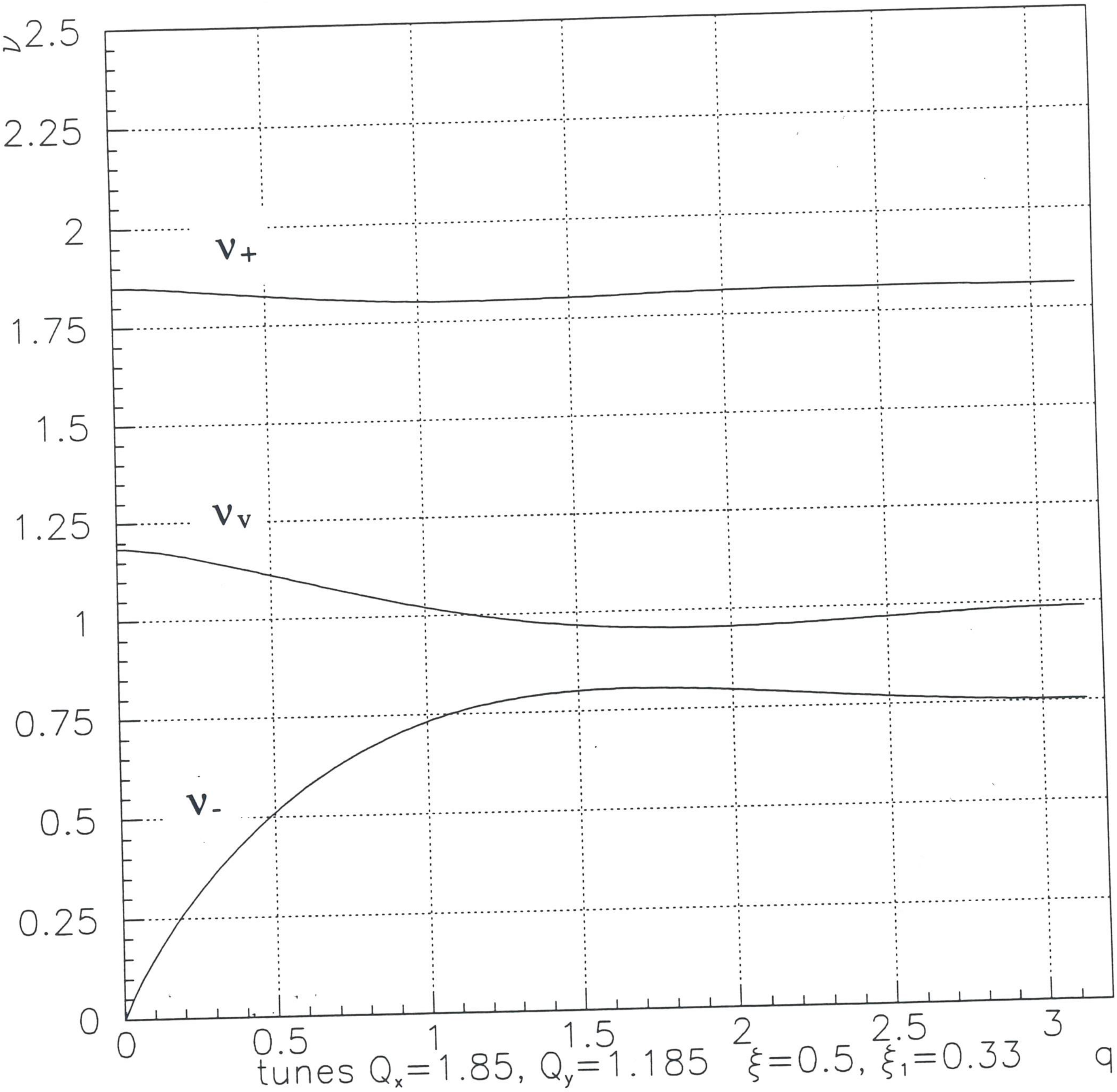

Fig. 1.3 - Coherent spectrum for a zig-zag configuration.

1.2.2 Fluctuations and Melting

The properties of the frequency spectrum can also be used to examine the influence of temperature on particle correlations and to find the corresponding break-up temperature for a given Crystalline structure.

Let us first take in to consideration the temperature dependence of long-range correlations in the longitudinal positions of the particle. For a given crystal temperature T, the amplitude of oscillations z_q of a longitudinal mode with wave number q is inversely proportional to its frequency $\omega(q) = \omega_0 \nu(q)$ and hence, from the equipartition theorem, it results:

$$z_q^2 = \frac{2T}{NM\omega^2(q)}$$

where ω_0 is the revolution frequency in the rest frame system, N is the number of particles and M is their mass.

This gives rise to the misalignment of the relative longitudinal positions of the particles arranged at a given distance j:

$$< \delta z_j^2 > \equiv \frac{1}{N}\sum_{n=1}^{N}\left(z_{n+j} - z_n\right)^2 = \frac{4T}{NM}\sum_{q}\frac{1-\cos(qj)}{\omega^2(q)}$$

In the long wave region, longitudinal waves have a universal sound-like dispersion:

$$\omega(q) = qu, \qquad u^2 = 2c^2\Lambda\frac{Z^2 r_p}{Ad}\left(1 - \frac{\gamma^2}{Q_x^2}\right)$$

with L a logarithmic factor defined as:

$$\Lambda = \max\left(\ln\frac{1}{q}, \ln\frac{D}{d}\right)$$

where D is the pipe aperture. When $j >>1$, the main contribution in the summation over the modes yield the region of wave number $q \cong i / j$, which gives an estimation of the misalignment:

$$< \delta z_j^2 > \cong d^2 \frac{j}{\Gamma \Lambda}$$

where $\Gamma = Z^2 e^2 / Td$ is the customary correlation parameter.

Finally, taking into account that the break-up of this long-range correlations occurs when the misalignment is of the same order of the particle-to-particle distance, the value of the correlation parameter $\Gamma_{//}(j)$ corresponding to the break-up results:

$$\Gamma^*_{//}(j) = \Gamma^* \frac{j}{\Lambda} \cong \frac{j}{\Lambda}$$

or, in terms of temperature:

$$T^*_{//}(j) \cong T^* \frac{\Lambda}{j}$$

where $T^* = T^*_{//}(1) \cong Z^2 e^2 / d$ is the melting temperature of a string.

The break-up of the long-range correlations at temperatures that are inversely proportional to the distance between the particles is a typical behavior caused by the sound-like dispersion of the longitudinal spectrum at long wavelengths.

The short-range part of the coherent spectrum may be rather complicated. Even simple configurations as the string and zig-zag have three branches in the spectrum, and the eigenfrequencies may differ by orders of magnitude. In such cases a Crystalline structure should be described not by a single melting temperature, but by a certain sequence of temperatures. A rather simple case of melting point hierarchy is represented by the vertical zig-zag case. If the zig-zag is not far away from its threshold, it is possible to demonstrate that the break-up of the transverse order occurs at a much lower temperature than for the corresponding longitudinal short-range order. As for the previous case, applying the equipartition theorem, it is possible to derive the break-up temperature for transverse correlations. Transverse correlations are destroyed when the amplitude of thermal oscillations are of the same order of magnitude as the transverse size of the zig-zag. This takes place when the correlation parameter $\Gamma_\perp^*$ is:

$$\Gamma_\perp^* = \frac{2.4}{\left(\dfrac{\xi}{\xi_1} - 1\right)^{3/2}}$$

If the correlation parameter for the zig-zag is lower than this value, its transverse order is destroyed; however, the longitudinal order disappears only at $\Gamma = \Gamma^* \cong 1$. Near the zig-zag threshold these two melting points may differ significantly.

1.2.3 Shear Forces and Breathing

The attainment of Crystalline states for a cooled beam in a storage ring can be prevented by the viscous heating due to the shear induced in the dipole fields. Shear will transfer some of the energy of coherent motion to the thermal energy and may prevent reaching the low temperatures required for formation of Crystalline states. The solution at the equilibrium for the third equation of motion (see *sec. 1.2*) imposes the condition of equal revolution frequency for all the particles of the crystal, which is the condition for a Crystalline Beam to survive in a general and realistic lattice. In fact, in the numerical simulations particles only underwent longitudinal and transverse oscillations with the ring lattice periodicity. While the mentioned solution is a direct consequence of smooth approximation (the equation of motion are time-independent), in the simulations the general time-dependent equations are used. Also in this case a stable and periodical solution can be found. This solution has a periodicity corresponding to the lattice cell of the magnetic structure. An example of such behaviour is shown in *Fig. 1.4*, where a crystallized shell is shown at different positions within a cell of the CRYSTAL

Storage Ring. The Crystalline Beam can travel along the storage ring if it has a proper value of the momentum gradient $\partial p_z / \partial x$. In fact, all the structures achieved in the simulations occurs to have this gradient as shown in *Fig. 1.5*. The same results were found also by *J. Wei and al.* [WEI2]; the authors explain the results as that the crystal "takes up the difference" between constant angular velocity and constant linear velocity by adjusting the spacing between particles, i.e. by converting potential energy into kinetic energy.

Only on average, the Coulomb repulsion of the space charge dominated beam is balanced by the external confining forces. An alternation of the focusing gradient and the bending field along the circumference imposes a variation of the beam sizes with the lattice periodicity. This correspond to a "breathing" of the beam and can be described by the following equation:

$$a''_{x,y} = \left(Q^2_{x,y} - g_{x,y}(\theta)\right)a_{x,y}.$$

Here, the influence of the orbit curvature variations is neglected for simplicity sake, supposing that $Q_x^2 >> \gamma^2$. The Coulomb forces are substituted by their average values, balancing the average external confining forces. This approximation is justified if the beam size variations $\Delta a_{x,y}$ are relatively small, i.e. $\Delta a_{x,y} / a_{x,y} << 1$.

The ordinary second-order linear differential equation with periodical coefficients has zero eigenfrequencies. Therefore it has a periodic basic solution, which describes the behavior of the beam size up to a constant factor, so that relative size variations can be evaluated. A comparison between these solutions and the PARMT simulations for a crystallized shell is shown in *Fig. 1.6*. The breathing is rather small because of the smoothness of the CRYSTAL Storage Ring: $\Delta a_x / a_x = 11\%, \Delta a_y / a_y = 9.5\%$.

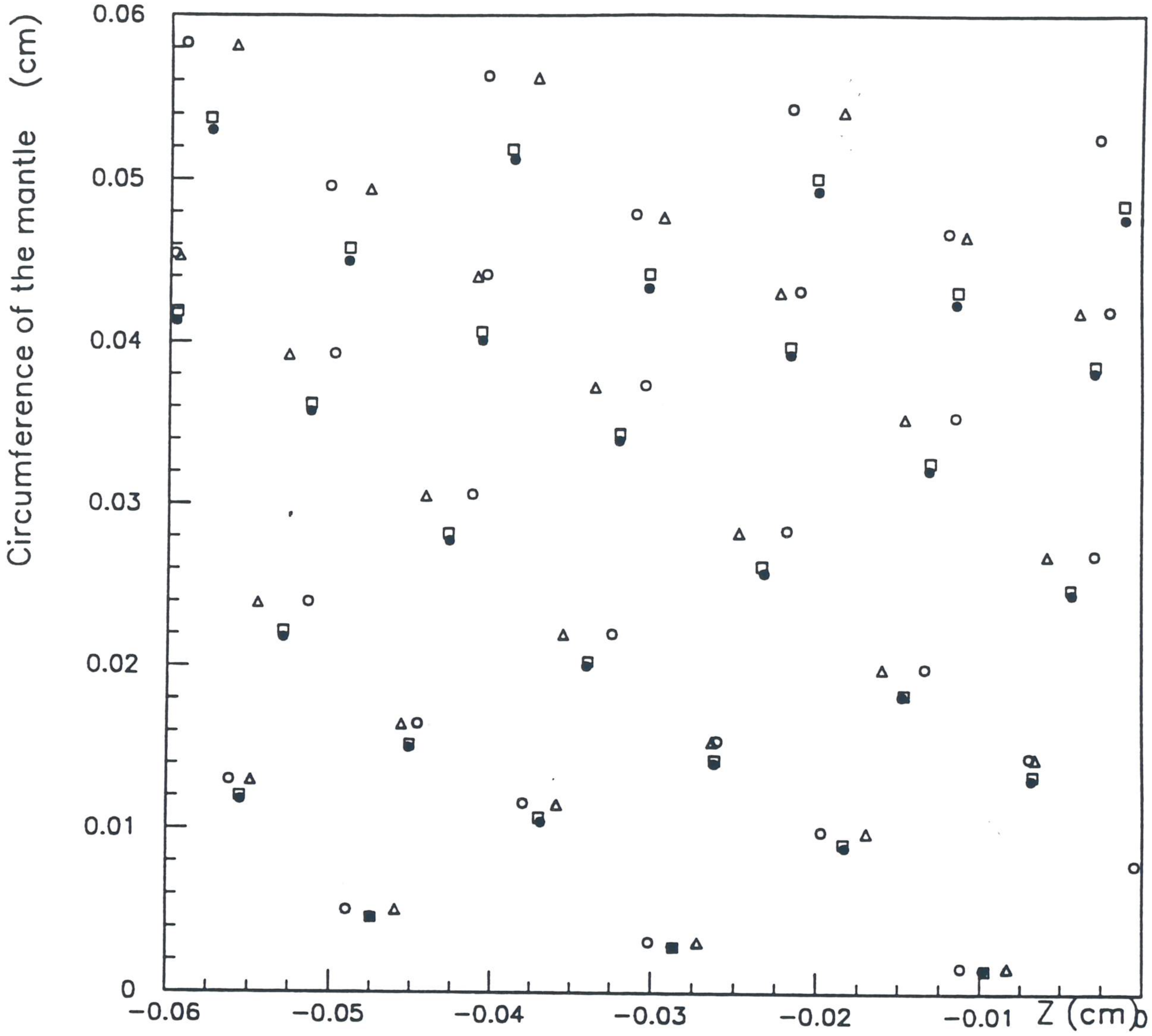

Fig. 1.4 - Shell configuration in a periodic cell of the CRYSTAL Storage Ring. Particles are projected onto the mantle at different positions in the cell: ● - middle of the drift space, Δ - entrance of the dipole, ○ - exit of the dipole, ☐ - middle of the next drift section.

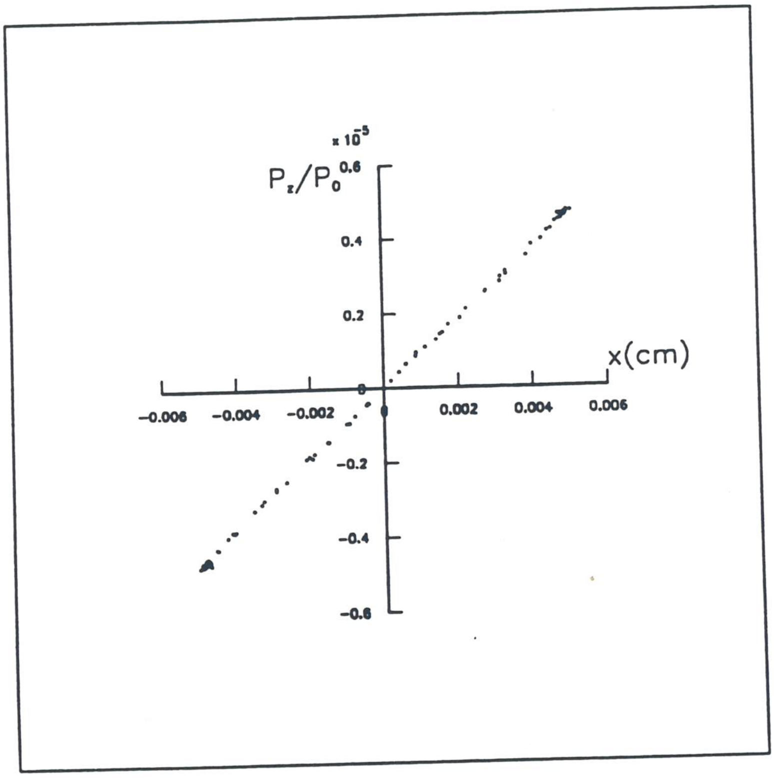

Fig. 1.5 - Longitudinal momenta p_z in the reference frame versus the horizontal coordinate of particles in a steady Crystalline state of a cooled beam. The momenta are given in units of the reference particle momentum p_0.

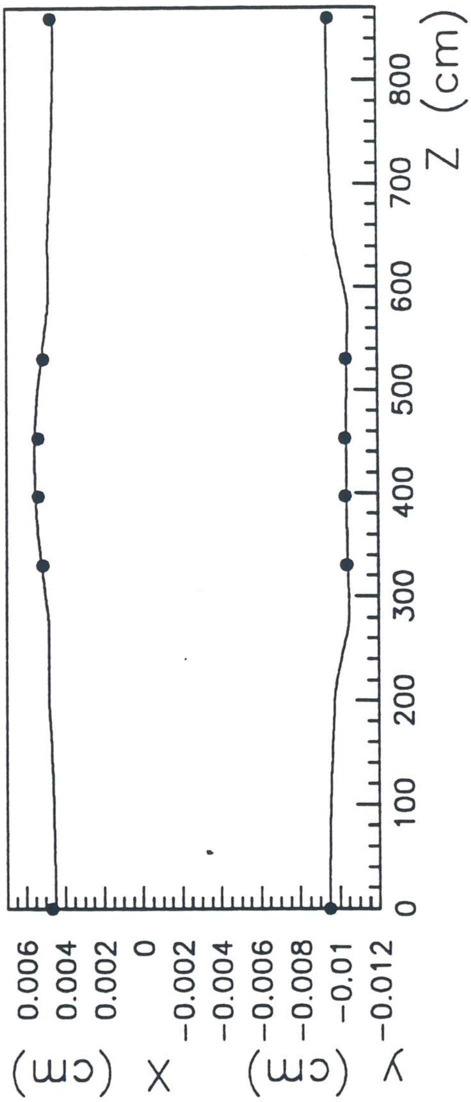

FIG. 1.6 - Breathing: comparison between the analytical solutions (solid curve) and the PARMT results (dots).

1.3 Envelope Instability of a Space Charge Dominated Beam

The transport of intense and cold ion beams through a storage ring has some common features with beams in heavy ion inertial fusion, for which several critical aspects have been revealed since the 1950s. Originally envelope equations are derived by Kapchinskij and Vladimirskij based on the Vlasov equation [KAP1]. Assuming *rms* envelope and *rms* emittance as defined by:

$$u_x(s) = \sqrt{<x^2>}$$

$$\varepsilon_x^2(s) = <x^2><x'^2> - <xx'>^2;$$

$$u_y(s) = \sqrt{<y^2>}$$

$$\varepsilon_y^2(s) = <y^2><y'^2> - <yy'>^2$$

envelope equations reads:

$$\frac{d^2u_x}{ds^2} + \left(k_x^2(s) - \frac{1}{\rho^2}\right)u_x - \frac{Z<xE_x>}{Mc^2\beta^2\gamma^3u_x} - \frac{\varepsilon_x^2(s)}{u_x^3} = 0$$

$$\frac{d^2u_y}{ds^2} + k_y^2(s)u_y - \frac{Z<yE_y>}{Mc^2\beta^2\gamma^3u_y} - \frac{\varepsilon_y^2(s)}{u_y^3} = 0$$

where k_x, k_y are the focusing functions and M is the ion mass.

These equations are self-consistent since the charge distribution is exactly of Kapchinskij-Vladimirskij type. Analytical and numerical studies are made by *I. Hofmann et. al.* [HOF1] demonstrating that the K-V distribution in a periodic focusing channel is subject to various instabilities. The main conclusion of the work of Hofmann and collaborators is that the phase advance of a single particle, σ_0, in the cell should not exceed 90^0 to avoid the second-order instability. Struckmeier and Reiser [STR2] studied the behavior of mismatched intense charged-particle beams in periodic transport channels and found two mismatched oscillations, one in which the amplitude of oscillations in the two transverse directions are "180^0 out of phase" and one in which they are "in phase". Still they confirm that $\sigma_0 < 90^0$ is the safe condition with respect to envelope perturbations for mismatched beams. For the instability of cold and space charge dominated ion beams in a storage ring, Hofmann and Struckmeier [HOF2] demonstrated the existence of such an effect by computer simulation.

Based on electron and laser cooling, longitudinal beam temperature in the *mK* range was achieved experimentally in a storage ring [HAN1], but transverse temperatures are still about several thousand Kelvin [HOC1]. Besides experimental efforts to develop fast transverse cooling techniques, an advance in understanding the transport of space charge dominated beams in a storage ring is needed. The envelope instability can be considered as an effect that prevents to achieve low transverse temperatures. In particular the insertion of additional elements cause the breaking of the lattice periodicity and as a consequence the beams result mismatched. Being the beams, in our case, always under frictional cooling forces, a quantitative knowledge of the instability growing rates is of particular interest.

To study the envelope instability, the beam transport has been simulated by using the PARMT code. Simulations are performed for the CSR storage ring but the results, depending only on the betatron phase advance and not by the lattice function in detail, are of general use and scalable to any storage ring. The magnetic structure of the ring consists of eight symmetric cells, with the parameters listed in *Table 1.4*. Two cells of the lattice are shown in *Fig. 1.7*.

The envelope instability is analyzed for different focusing conditions with and without periodicity perturbations. In this case the insertion of the electron cooler and of the sextupoles is considered as a periodicity perturbation. In order to study the instability a semi-Gaussian particle distribution is considered. For all simulations the beam consists of $10^8\,Be^+$ ions ($\beta=0.07$.) Initial emittances are chosen with a space charge phase advance of $\sigma=32^0$, which should cause envelope instability. To study only the envelope instability, separately excluding the contribution of the intrabeam scattering on the emittance growth, the simulations have been made with a self-consistent calculation of space charge forces by means of a Poisson solver.

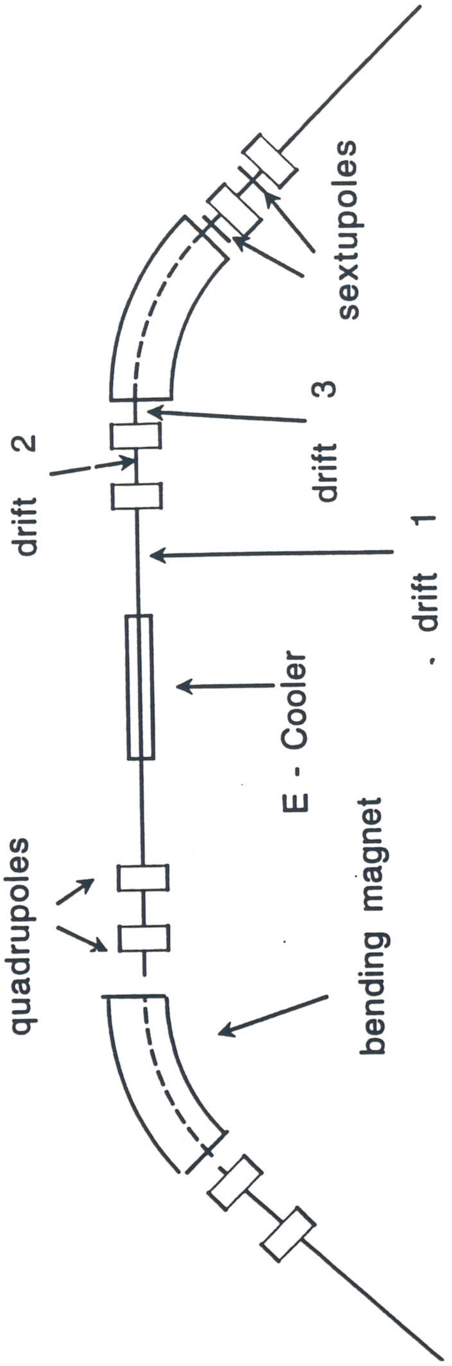

Fig. 1.7 - Two cell of the ring showing the location of the elements perturbing the periodicity.

Table1.4 - Parameters of the storage ring.

Element	Length (m)	
Drift 1	2.0	
Focusing quadrupole	0.25	
Drift 2	0.40	
Defocusing quadrupole	0.25	
Drift 3	0.40	
Sector Magnet	4.40	angle=π/4
Drift 3	0.40	
Defocusing quadrupole	0.25	
Drift 2	0.40	
Focusing quadrupole	0.25	
Drift 1	2.0	
Periodicity	8	

According to *Ref.* [HOF1], multipolarity of the unstable oscillations depends on the single particle phase advance per cell σ_0. Simulations were done for three different values of the phase advance σ_0 : (i) $\sigma_0 = 60^0$, (ii) $\sigma_0 = 90^0$, (iii) $\sigma_0 = 125^0$.

Fig. 1.8 shows the evolution of the beam for the three tunes mentioned above. It is confirmed that $\sigma_0 = 90^0$ is a safe condition for the envelope mode.

Similar simulations were repeated perturbing the ring periodicity by inserting the electron cooler and a pair of sextupoles. The space charge of cold electrons acts as a focusing lens, which in our case has a focal distance of about *60 m*. In simulations the cooler is modeled by a *1 m* long solenoid and a *1000 Gauss* magnetic field, together with a thin focusing lens. Two pair of sextupoles, *20 cm* long and with a gradient of $5\ Tm^{-2}$, were placed in two cells only, close to the quadrupoles (see *Fig. 1.7*).

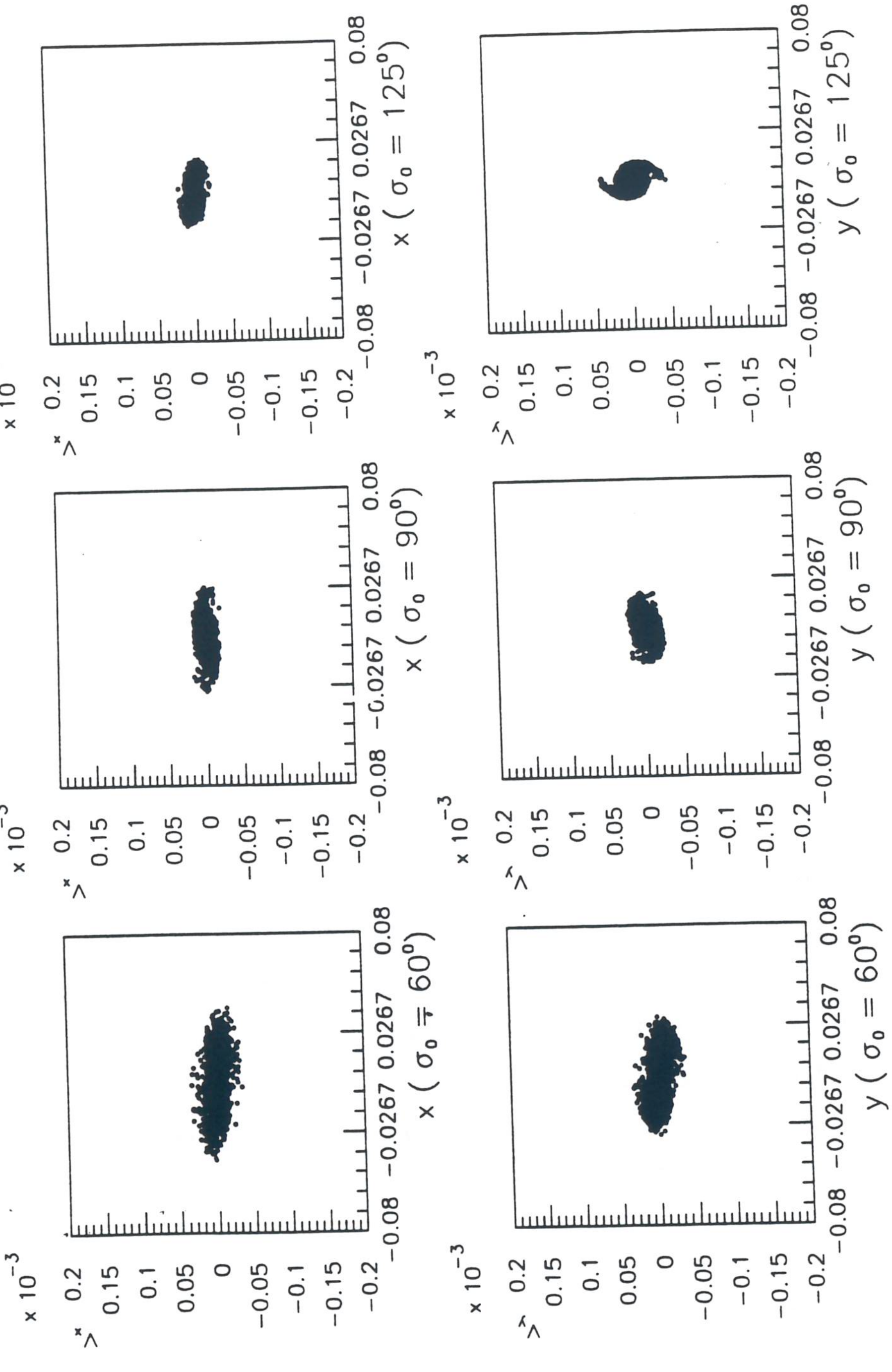

Fig. 1.8 - Semi-Gaussian beam distributions for different single particle phase advances σ_0, without periodicity perturbation.

As for the previous case, *Fig. 1.9* shows the evolution of the beam for the three mentioned tunes. The typical distortion connected to the envelope instability can be recognized by the two arms growing out of the initial distribution (case iii). Comparing *Fig. 1.8* and *Fig. 1.9* it appears that the distortion of the particle distribution is more important for the case of perturbated periodicity; but still $\sigma_0 = 90^0$ represents a safe condition for the envelope mode.

A quantitative estimation of the blow-up rate of the envelope instability is of great interest for general understanding. According to *Ref.* [HOF1], the onset condition of envelope instability depends on the single particle phase advance of a storage ring σ_0 and on the space charge dominated phase advance σ, which is reduced because of the cooling. To simulate the growth time of the envelope instability the beam is chosen with an initial emittance of $10^{-6}\pi$ *mrad* and is cooled down to a plasma parameter $\Gamma=1$. The cooling process is simulated by reducing the emittances of a fixed quantity, once every revolution. The blow up rate of the envelope instability is deduced from the required cooling forces to obtain the desired plasma parameter. The result of the simulations is shown in *Fig. 1.10*, for different σ_0. The drastic change of the curve behavior for $\sigma_0 > 90^0$ clearly indicates transverse heating from the envelope modes, as expected. For a phase advance $\sigma_0 < 90^0$ the beam can be cooled down to $\Gamma= 1$ with a e-folding cooling time of *5.8 ms*. This cooling time represent a lower limit, in fact longer cooling times were not explored because they require very long computation time. In addition, the use of longer cooling time can also produce not correct results because of numerical errors, which affect calculations involving small numbers. For $\sigma_0 > 90^0$ the envelope instability produces a three order of magnitude faster blow up rate, which gives an e-folding cooling time in the μs range. The simulations show that the heating due to the envelope instability is even stronger than the heating coming from intrabeam scattering.

Compared with the transverse cooling time of the best experimental results, the blow up time of the envelope instability is very short in the present storage ring and the

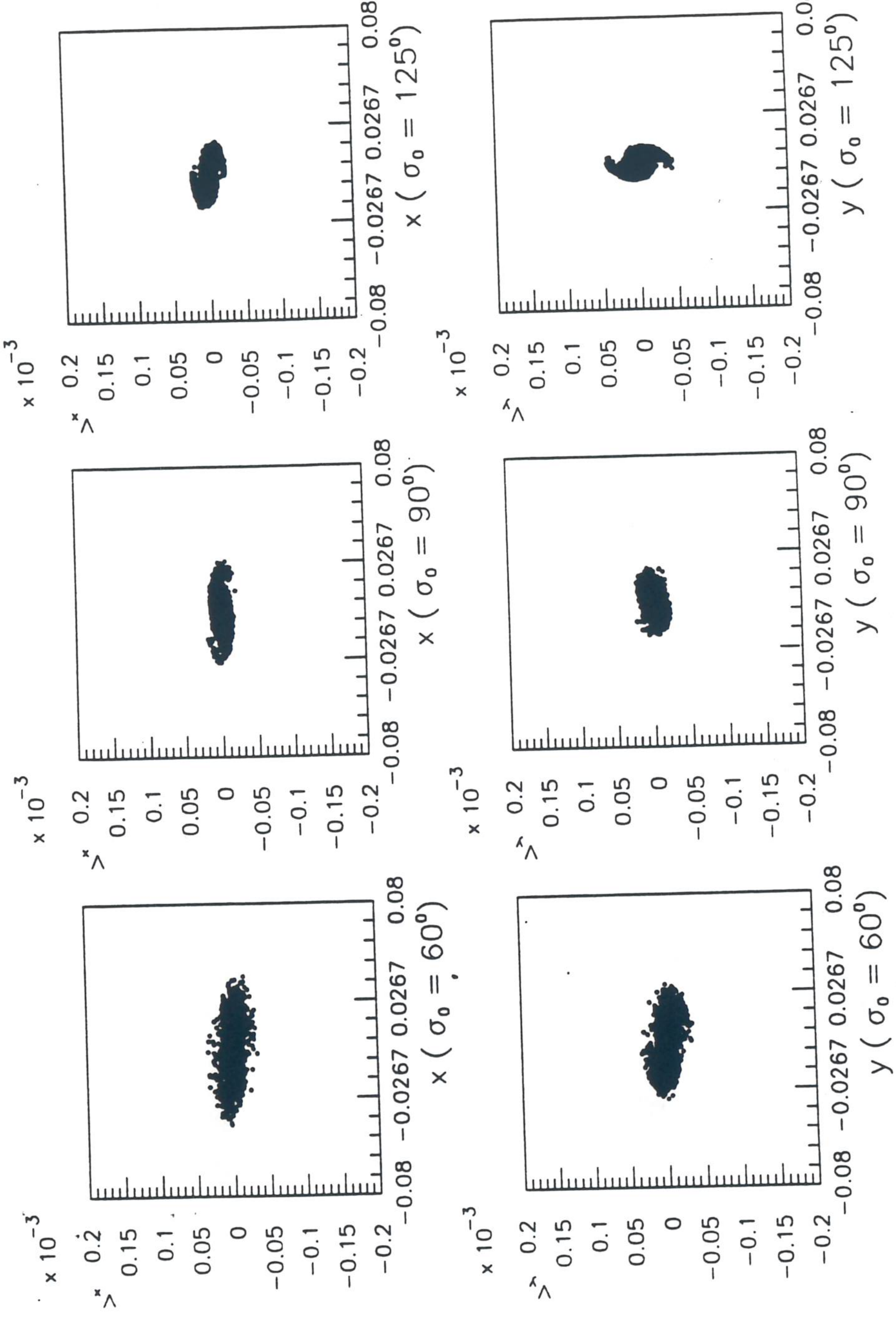

Fig. 1.9 - Semi-Gaussian beam distributions for different single particle phase advances σ_0, with periodicity perturbation.

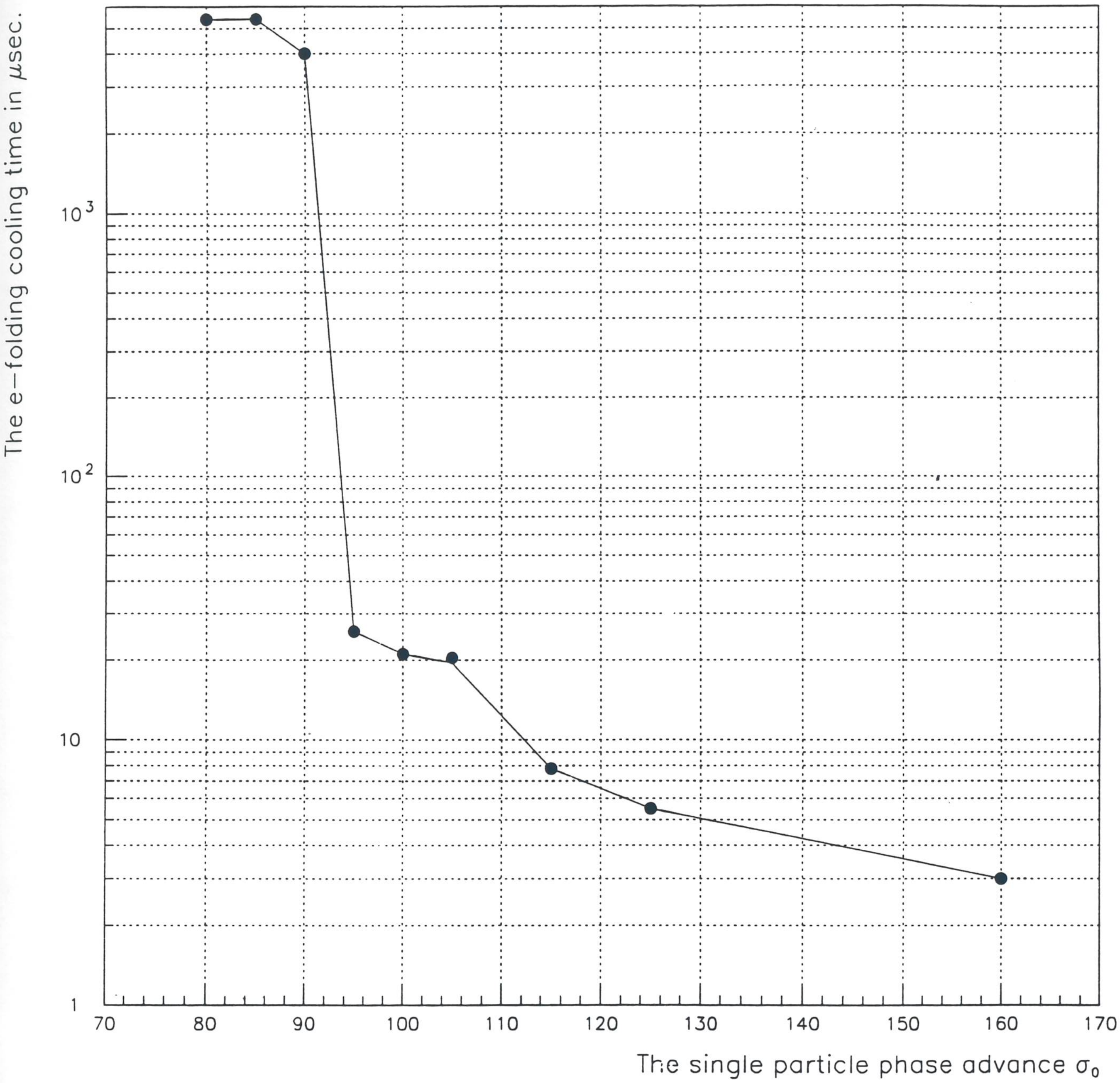

Fig. 1.10 - The e-folding cooling time required to compensate the blow up rate of the envelope instability, in order to obtain a beam with plasma parameter $\Gamma=1$, in function of the single particle phase advance σ_0.

transverse beam temperature can hardly be decreased below a certain value. Therefore, the simulation results suggest that a storage ring aimed at crystallizing ion beams has to fulfill the condition $\sigma_0 < 90^0$.

References

[BIR1] G. Birkl, S. Kassner and H. Walther; Nature 357 (1992) 310.

[BIS1] G. Bisoffi et al.; The Crystal Storage Ring Project at Legnaro; Presented at the European Particle Accelerator Conference EPAC 94, London June 27-July 1, 1994.

[BOI1] G. Boicount and J. Merson, Los Alamos National Laboratory, Report LA-UR-90-127, January 1990.

[BUR1] A.V. Burov; Steady States and Eigenmodes of a Crystal Beam in a Storage Ring; Submitted to Part. Acc.

[DEM1] E.N. Dementiev, N.S. Dikansky, A.S. Medvedko, V.V. Parkhomchuk and D.V. Pestrikov; Sov. Phys. Tech. Phys. 25 (1980) 1001.

[HAE1] T. Haensch and H. Schawlow, Opt. Com. 13 (1975) 68.

[HAN1] J.S. Hangst et al.; Phys. Rev. Lett. 67 (1991) 1238.

[HAS1] R.W. Hasse and J.P. Schiffer; Ann. of Phys. 203 (1990) 419.

[HAS2] R.W. Hasse; Phys. Rev. Lett. 67 (1991) 600.

[HOC1] B. Hochadel et al.; Proceedings of the Workshop on Beam Cooling and Related Topics, Montreux, 4-8 October 1993, CERN 94-03, 198.

[HOF1] I. Hofmann, L.J. Laslett, L. Smith and I. Haber; Particle Acc. 13 (1983) 145.

[HOF2] I. Hofmann and J. Struckmeier; Proc. of the Workshop on Crystalline Ion Beams, Wertheim, Germany, October 1988, Report GSI 89-10 (1989), 140.

[KAP1] I.M. Kapchinskij and V.V. Vladimirskij; Proceedings of International Conference on High Energy Accelerators, CERN, Geneva (1959), 27.

[LI1] X.P. Li, A.M. Sessler and J. Wei; Crystalline Beam in a Storage Ring: How Long Can It Last?; Presented at the European Particle Accelerator Conference EPAC 94, London June 27-July 1, 1994.

[RAH1] A. Rahman and J.P. Schiffer; Phys. Rev. Lett. 57 (1986) 1133.

[RUG1] A.G. Ruggiero; Demonstration of No Feasibility of a Crystalline Beam in a Betatron Magnet; BNL-49529, September 1993.

[SCH1] J.P. Schiffer and P. Kienle, Zeitschr. f. Phys. A321.

[STE1] M. Steck et al.; Suppression of Intrabeam Scattering in Cooled Heavy Ion Beams; to be published.

[STR1] J. Struckmeier and I Hoffman, GSI-ESR-87-03, Darmstadt 1987.

[STR2] J. Struckmeier and M. Reiser; Part. Acc. 14 (1983) 227.

[TEC1] L. Tecchio et al. (CSR Collaboration); CRYSTAL: A Storage Ring for Crystalline Beams; LNL-INFN (REP) 80/94.

[WAK1] I. Waki, S. Kassner, G. Birkl and H. Walther; Phys. Rev. Lett. 68 (1992) 2007.

[WEI1] J. Wei, X.P. Li and A.M. Sessler; Crystalline Beam Ground State; BNL-52381, June 1993.

[WEI2] J. Wei, Xiao-Ping Li and A. Sessler; Phys. Rev. Lett. 73 (1994) 3089.

2
The Storage Ring

2.1 Lattice and General Layout

The overall size of the storage ring was determined by some general considerations such as the largest specific kinetic energy of the ions which have to be stored, the matching with the heavy ion injector and, most important, the requirements for Crystalline Beams. The maximum specific energy has been fixed at *50 MeV/u* for *Gold* ions *(51+)*, corresponding to a magnetic rigidity of *3.8 Tm*. The storage ring has a total length of *70 m*. The maximum magnetic rigidity was chosen in connection with the use of the storage ring for other purposes, namely nuclear, atomic and molecular physics. The value of *3.8 Tm* places the CSR Storage Ring in a complementary position with respect to the similar existing facilities.

The shape and symmetry of the ring was determined by a compromise between an ideal machine for crystallization purposes, where the beam is preserved from external perturbations, and the need for several straight sections where to accomodate injection, extraction, acceleration, cooling and diagnostic devices.

It has been proven [BJO1] that minimization of the intrabeam scattering blow up is related to minimization of the first derivatives of the horizontal and vertical β–functions and of the dispersion function (η') along the machine. The simulations performed with the computer code MAD [GRO1] show that high periodicity of the lattice and short drift sections are preferable. As a matter of fact, the electron cooler device needs a rather long drift space and this determines the length of all drift sections.

In addition, the demand for a single particle phase advance $\sigma_0 < 90^0$, in order to avoid envelope instability (see *sect. 1.3*), imposes already a minimum periodicity to the ring;

the eightfold symmetry is the minimum geometry satisfying this requirement.

Furthermore, the need for many straight sections, combined with the high periodicity required to obtain Crystalline Beams and to avoid crossing systematic betatron resonances, also imposes such a geometry (see *Fig. 2.1*). For the given periodicity of the lattice, betatron tunes stay enough far away from the following low-order systematic resonances:

$$\begin{array}{rl} Q_x = i, & Q_y = j \\ 2Q_x = k, & 2Q_y = l \\ Q_x + Q_y = m, & Q_x - Q_y = n \end{array}$$

with *i, j, k, l, m* and *n* integers.

Several sets of values can satisfy these requirements and one can change between different working points and use the most suitable for the actual experiment. Although the storage ring can be used for different applications, here only the working point directly connected to the formation of Crystalline Beam structures will be discussed.

The magnetic lattice consists of eight *45°* bending magnets, *32* quadrupoles (and *32* sextupoles). The dipoles are sector magnets with zero entrance and exit angles; their length along the reference orbit is *2 m*. Only one type of quadrupole is used; their length is *0.25 m* and are assembled in four families for the normal operation mode. To operate the machine for Crystalline Beams only two families of quadrupoles are required. The bending magnets have a vertical aperture of *80 mm*, corresponding to a vertical acceptance of *50 π mm mrad*; while the quadrupoles have a bore radius of *65 mm*. Two families of sextupoles have been considered to correct horizontal and vertical chromaticities. The sextupoles have the same bore radius as the quadrupoles and their length is *0.20 m*.

The drift space between the quadrupole-sextupole and quadrupoles is *0.1 m* and *0.4 m*, respectively; while the length of the straight sections is *3.4 m*. These latter will house the injection and extraction system, cooling devices, RF cavity, diagnostic devices and correcting magnets.

The transition energy $\gamma_{tr} = 1.76$ is a large value which always keeps the machine operating well below it.

A summary of the lattice and cell parameters is given in *Tables 2.1.1* and *2.2*.

The lattice parameters are determined by computer simulation using the codes MAD [GRO1] and TRACE-2D [CRA1].

Table 2.1 - Lattice Parameters of the CRYSTAL Storage Ring.

Description	Crystalline Mode
Ring Length [m]	68.8
Lattice Periodicity	8
Magnetic Rigidity [Tm]	3.8
Bending Radius [m]	2.55
Phase Advance per Period:	
Horizontal	83^0
Vertical	53^0
Transition γ	1.76
Betatron Tunes:	
Q_x	1.85
Q_y	1.185
Natural Chromaticity:	
ξ_x	-0.72
ξ_y	0.21
β_x, max [m]	6.74
β_y, max [m]	10.4
Dispersion max [m]	3.6
Momentum Compaction	0.32

The positioning of the magnets requires special care. The following alignment *rms* errors are considered to be within the present state of the art: *0.1 mm* for both dipole and quadrupole lateral displacement and *0.2 mrad* for axial rotation. In addition, an integrated dipole field error of the order of 10^{-4} *rms* is required. This cause an uncorrected orbit distorsion with an expected value smaller than *0.8 mm.*

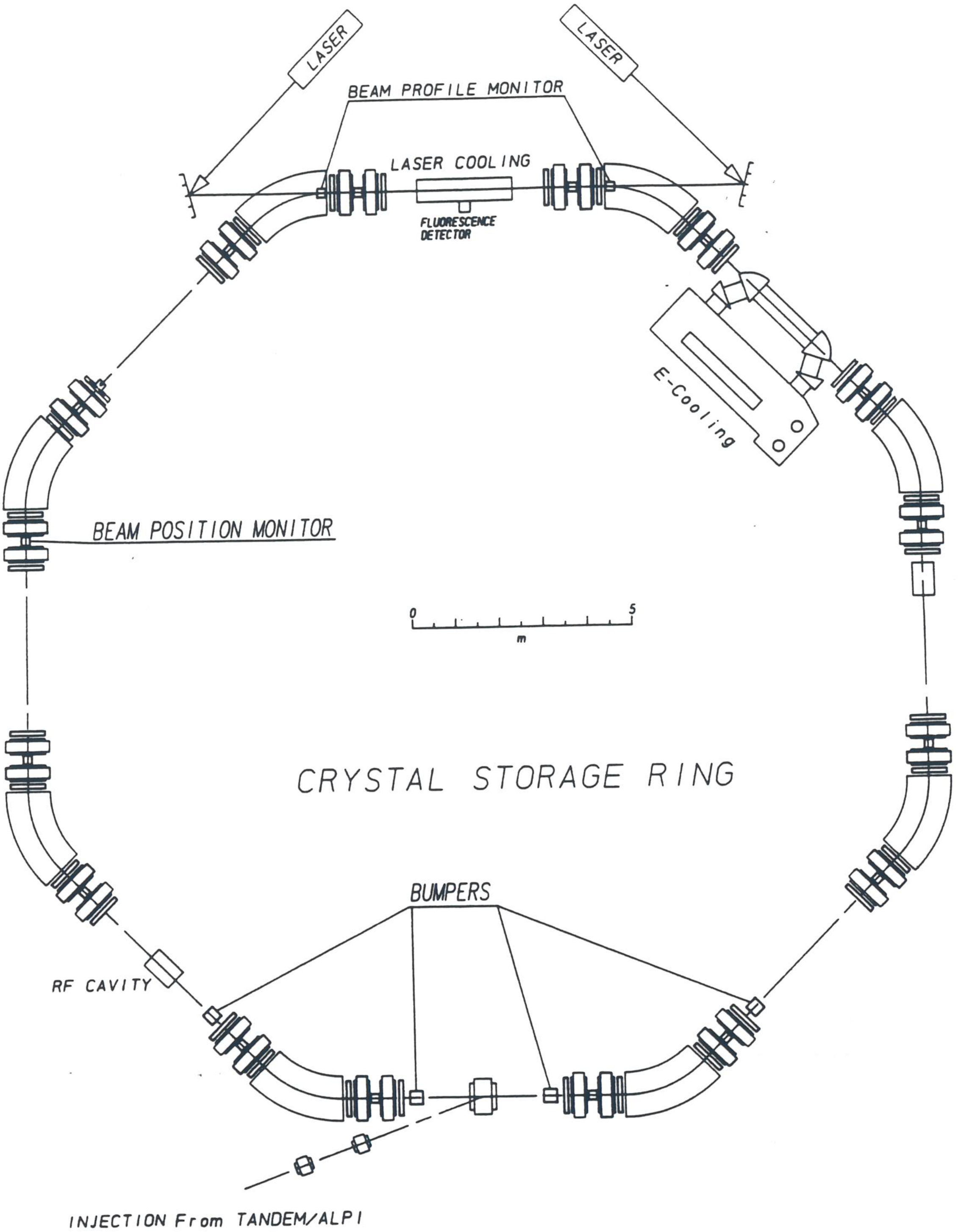

Fig. 2.1 - Layout of the CRYSTAL Storage Ring.

To keep the acceptance of the ring maximum, the closed orbit distorsion has to be minimized. The compensation can be done by properly located correcting dipoles. In addition to the correcting dipoles, extra horizontal compensation must be obtained from backleg windings on the bending magnets.

Table 2.2 - Cell Parameters of the CRYSTAL Storage Ring.

Description	Crystalline Mode
PERIOD Length [m]	8.6
Dipoles:	
Dipole Length [m]	2.0
Bending Angle	45^0
Bending Radius [m]	2.55
Vertical Gap [cm]	8
Drifts:	
Drift Length [m]	3.4
Quadrupoles:	
QF Length [m]	0.25
Strength [m^{-2}]	0.4
Gradient [T/m]	0.48
QD Length [m]	0.25
Strength [m^{-2}]	-0.6
Gradient [T/m]	-0.72
Bore Radius [cm]	6.5
Sextupoles:	
SF Length [m]	0.20
Strength [m^{-3}]	4.51
Gradient [T/m^2]	5.41
SD Length [m]	0.20
Strength [m^{-3}]	-3.97
Gradient [T/m^2]	-4.76
Bore Radius [cm]	6.5

2.1.1 The Working Point for Crystalline Beams

The accumulation of an ordered structure is the result of an equilibrium between the interparticle Coulomb force and the external focusing system. The effect of different lattices on the intrabeam scattering (IBS) rate of a previously cooled ion beam was investigated with the computer code INTRABS [CON1]. In comparison, the features of the beam itself (type of ion, its charge state, velocity, initial values of ε_x ε_y and $\Delta p/p$ - typical of an already cooled beam) were left unchanged, and only the lattice was varied.

Since, by definition, at equilibrium the compression of the six-dimensional phase space provided by the cooler and averaged on one turn cancels the phase space growth due to intrabeam scattering, it results that a lower IBS growth rate (expressed in our case as the increase rate of the transverse emittance and the longitudinal momentum width) poses less stringent requirements on the cooling system performance and is therefore favourable.

The working point for Crystalline Beams is characterized by smooth β-functions in order to decrease intrabeam scattering as much as possible. Furthermore, crystallization requires low phase advance per super period [HOF1] and hence low tunes.

When the beam crystallizes the tune shrinks towards zero (not necessarily for a string configuration) due to very strong space charge defocusing. It is favourable to be below the strong integer resonances $Q_x = Q_y = 2$ since these resonances are difficult to go through.

The working point for Crystalline Beams is determined optimizing the storage ring from the point of view of intrabeam scattering, as discussed above.

The lattice functions $\beta_x(s)$, $\beta_y(s)$ and $D_x(s)$ for such a configuration are plotted in *Fig. 2.2*, while the stability diagram is shown in *Fig. 2.3*. The tune for the Crystalline working point is $Q_x = 1.85$, $Q_y = 1.185$. There are several resonances in the vicinity of this working point. However, almost all drawn systematic resonances are driven by skew fields (n_y is odd) and thus less dangerous.

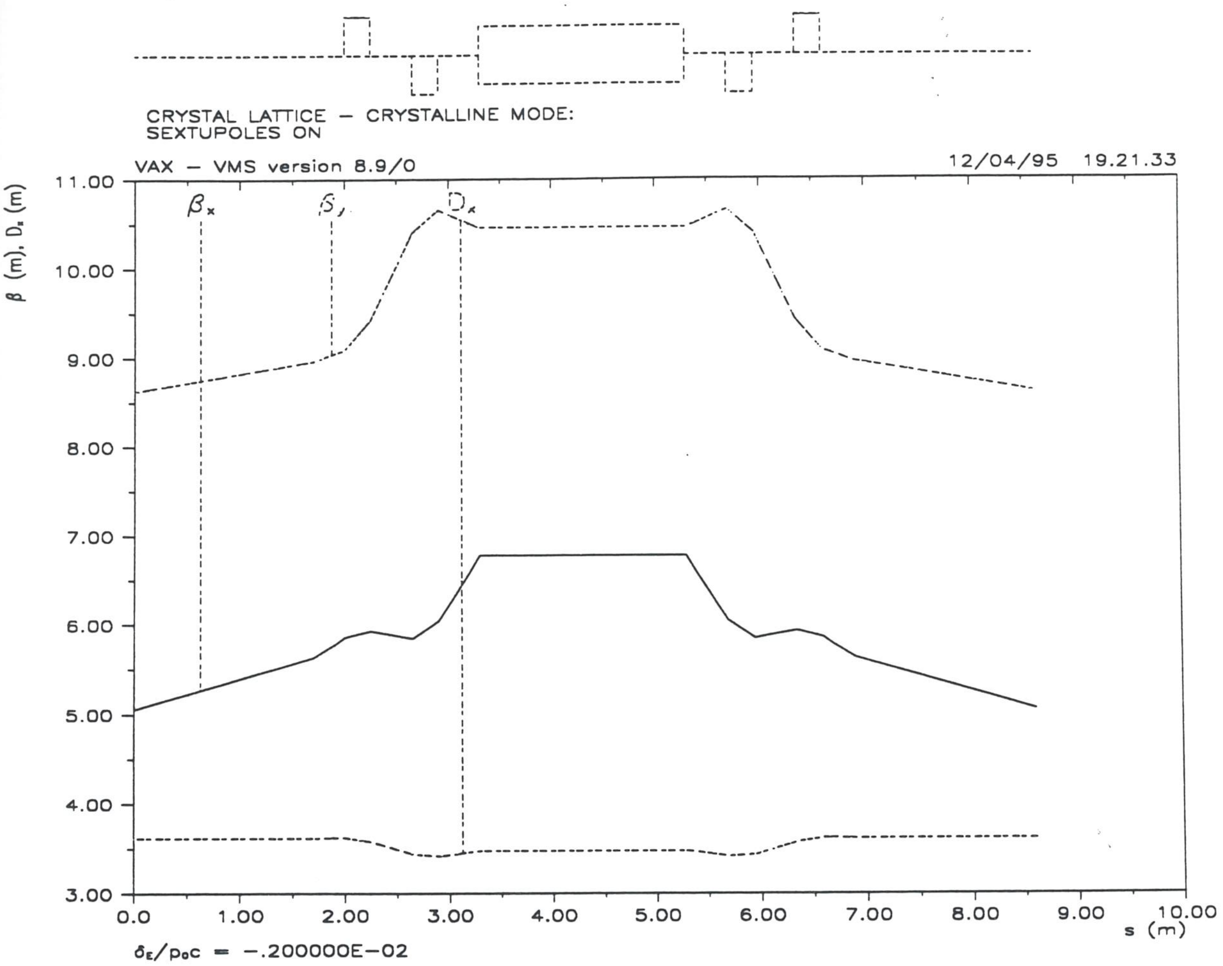

Fig. 2.2 - The lattice functions for the Crystalline mode.

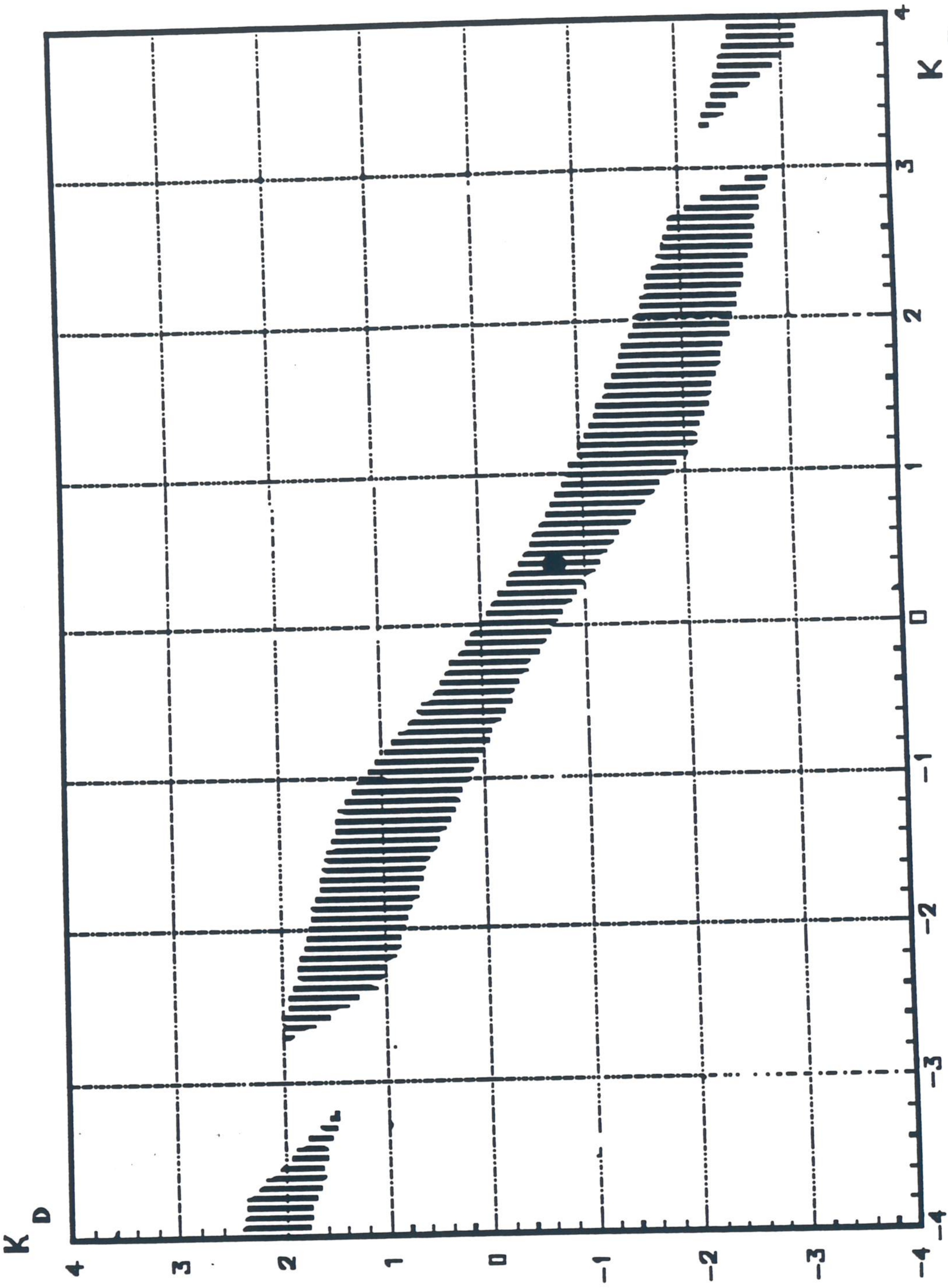

Fig. 2.3 - Stability diagram for two quadrupole families; K_D and K_F are the quadrupole strengths in m^{-2}.

Numerical values of the lattice functions and the quadrupole and sextupoles strengths are given in *Tables 2.1* and *2.2*.

2.1.2 Fringe Fields, Misalignments and Field Errors

The design of a realistic storage ring demands an accurate investigation about the effects produced by fringe fields, misalignments and field errors in bending magnets and quadrupoles, that act as perturbations on the beam. These perturbations lead to a distortion of the closed orbit and can excite resonances, which should be crossed by the beam under the cooling process.

The formation of Crystalline structures in ion beams under perturbed conditions have been studied by using the computer code PARMT. In the simulations a real cooling factor (at least for the string case) has been used and any kind of misalignments, field errors, fringe fields and periodicity perturbation have been taken into account.

For simulations a $^9Be^+$ beam ($\beta = 0.07$) and initial emittance of $1\ \pi\ mm\ mrad$ was considered. Similar results are obtained by using different kind of ions. The cooling effect was taken into account by reducing the beam divergences by a given factor after each revolution. A reduction factor of *1.003*, corresponding to an effective cooling time of *1 ms*, is used for simple Crystalline structures (string and zig-zag). Since the computation time increases quadratically with the number of ions, simulations of *3D* structures will demand huge computing time and are here not considered. The results are obtained aften 10^4 revolutions.

Fringe Fields

The code takes into account fringe fields of both quadrupoles and dipoles.

The field gradient $g(s)$ on the axis of a quadrupole field is calculated with the following ansatz:

$$g(s) = g_0 sin^2\left(\frac{1}{2}\pi s / L_R\right); 0 \le s \le L_R$$

where L_R is the length of the fringe fields. The magnetic field can be written as a power series containing only derivatives of the function $g(s)$ as coefficients [STE1]. The calculation of the particle transformations through the fringe fields is carried out by numerical integration of a system of differential equations. In the simulations L_R =5 *cm* has been used, which is realistic representation of well-designed quadrupoles.

The fringe field of dipoles is calculated more simply through a thin matrix formalism that takes into account the edge effects in bending magnets through the fringe field term ψ:

$$\psi = K_1\left(\frac{g_a}{\rho_0}\right)\left(\frac{1+\sin^2\alpha}{\cos\alpha}\right)\left[1 - K_1 K_2\left(\frac{g_a}{\rho_0}\right)\tan\alpha\right]$$

where α is the angle of rotation of pole face, g_a is the gap of magnet, ρ_0 the bending radius of central trajectory, K_1 and K_2 as usual are *0.35* and *4.0* respectively.

The fringe fields in the quadrupoles produce a small orbit displacement while the fringe fields in the dipoles contribute very slightly.

Misalignment

In general, misalignment effects can be taken into account by applying an angular deflection on the beam particles, that is a change in particle divergence. The particle divergence changes, due to any type of shifts and angular rotations of the optical elements, can be estimated separately and then added. So in calculations, after each bending magnet and each quadrupole, changes of particle divergence have been introduced randomly in both horizontal and vertical planes along the ring circumference. We took values of 0.1*mm* as maximum shifts and 0.2 *mrad.* as maximum rotations These kinds of misalignments produce two different maximum divergence changes for the two families of quadrupoles used in CSR. In fact a maximum divergence change of 0.045 *mrad* in both transverse planes has been evaluated for the focusing quadrupoles and 0.073 *mrad* for the defocusing one. The maximum divergence changes added after the bending magnet due to misalignments have been evaluated as 0.08 *mrad* in the horizontal plane and as 0.25 *mrad* in vertical plane. The divergence values are chosen randomly between the given maximum values and then added along the storage ring.

The misalignments produce a closed orbit distortion that does not prevent the formation of Crystalline Beams, as will be shown in the following

To determine the influence on the closed orbit distorsion due to quadrupole and dipole misalignments, their contributions have been separately studied. Misalignments on the dipoles are more effective than those on quadrupoles; the maximum allowable tolerances for the formation of Crystalline Beams have been found to be of *2 mm* shifts and *4 mrad* rotations for quadrupoles and of *1.5 mm* shifts and *2.5 mrad* rotations for dipoles.

Field Errors

The effects of field errors on the Crystalline Beams have also been included in the PARMT code. In all the quadrupoles and dipoles the field errors have been taken into account by adding a relative error to the values of both quadrupole strengths and curvature radii. In the simulations a set of field errors, corresponding to the *0.01 %* of the designed values, are chosen randomly. The resulting closed orbit distorsion is negligible in comparison with the distorsions induced by misalignments. By increasing the relative field errors up to *0.2 %* on both dipole and quadrupole elements Crystalline Beams are still obtained, but with increase of the closed orbit distorsion.

Periodicity Perturbations

To have the possibility to correct the chromaticity a series of sextupoles might be placed along the ring. Furthermore, the e-cooler solenoid is inserted in one drift section. These elements break the symmetry in the ring and can then be considered as periodicity perturbations. The sextupoles should therefore be placed symmetrically along the ring, it is then only the solenoid, used for the electron cooling, that breaks the symmetry. The sextupoles and the solenoid have to be taken into account in the simulations because they can become a source of heating for beam particles. The simulation results have shown that Crystalline Beams are still obtained but with an unlike closed orbit distortion and this is mainly due to the sextupoles effect. The solenoid insertion produces almost no effect.

In summary, all computer simulations have shown that in a realistic lattice, which includes fringe fields, misalignments, field errors and periodicity perturbations, Crystalline structures are still obtained. As comparison, *Fig. 2.4* and *Fig. 2.5* show Crystalline Beams (string and zig-zag) for an ideal and a realistic lattice respectively. For the realistic lattice the following tolerances are assumed: misalignments *0.1 mm* shifts and *0.2 mrad* rotations, field errors *0.01 %*. Periodicity perturbations and fringe fields are also included.

2.2 The Injection and Extraction Systems

Heavy ions will be injected into the CRYSTAL Storage Ring using the existing facilities at LNL: the XTU Tandem with the ALPI superconducting post-accelerator. The most efficient way of injecting into a storage ring is the pulsed mode, where the XTU Tandem-ALPI provides short beam pulses of heavy ions with peak current, giving good quality beams with small transverse emittance and momentum spread. With this scheme, it is possible to obtain beams with a wide range of

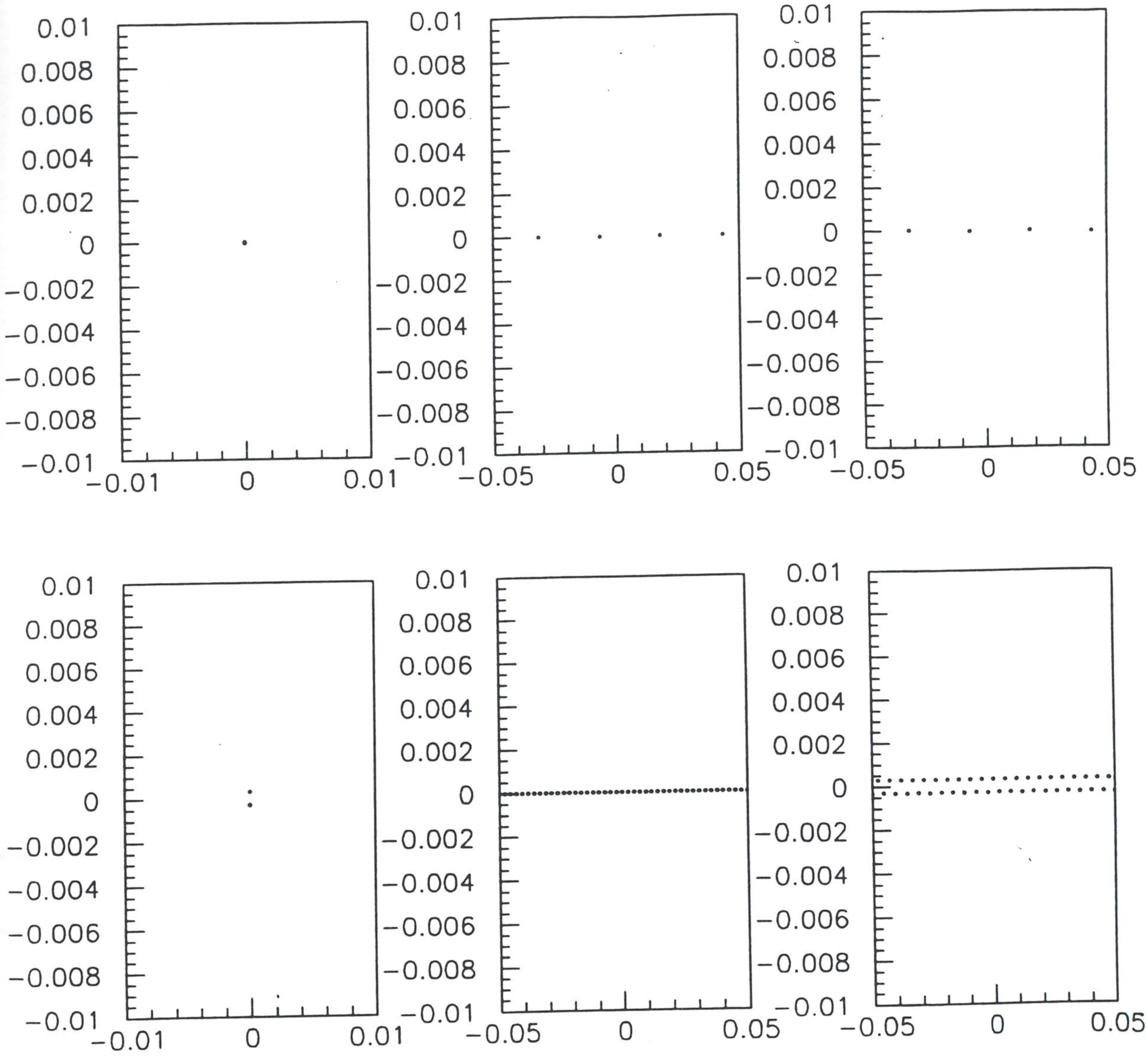

Fig. 2.4 - Crystalline structures of ${}^9Be^+$ ions ($\beta=0.07$) in an ideal lattice: string and zig-zag configurations.

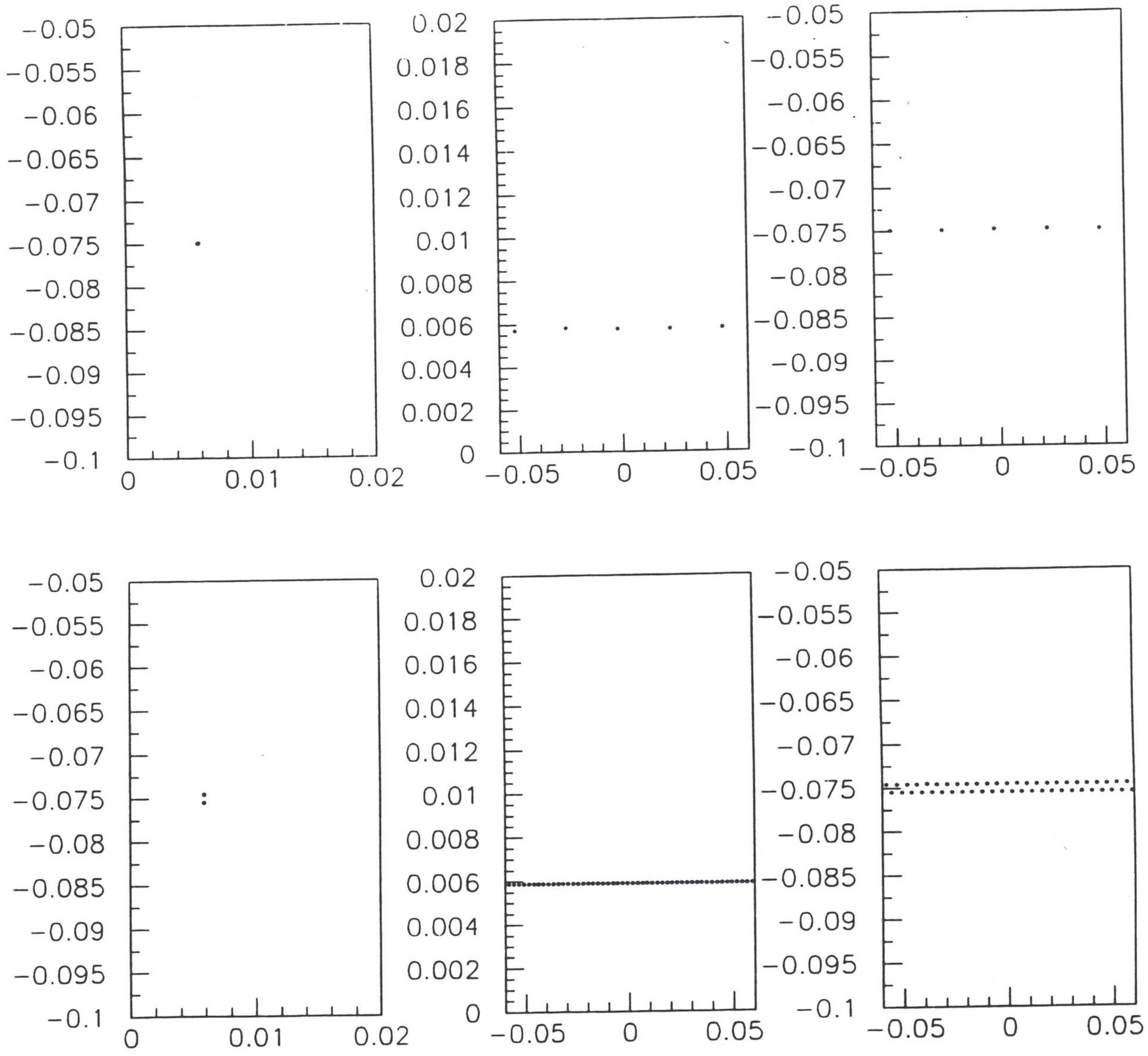

Fig. 2.5 - Crystalline structures of ${}^9Be^+$ ions ($\beta=0.07$) in a realistic lattice: string and zig-zag configurations. The following tolerances are assumed: misalignments *0.1 mm* shifts and *0.2 mrad* rotations, field errors *0.01 %*. Periodicity perturbations and fringe fields are also included.

mass numbers and sufficiently large charge states produced by stripping targets at proper location [TEC1].

If required, it will also be possible to inject into the CSR directly from the Tandem, bypassing ALPI.

The ions useful for laser cooling are $^{7}Li^{+}$, $^{9}Be^{+}$ and $^{24}Mg^{+}$, for which the Tandem has a very poor production efficiency. To produce such kind of ions, an indipendent low energy source, followed by a small electrostatic accelerator, can easily be installed closed to the injection, in the CSR area.

The most suitable source is a CHORDIS type and is chosen to provide a low emittance beam ($< 1\pi$ *mm mrad*) and small initial energy spread ($< 10^{-4}$), with typical current intensity of a few tens of *mA*. The beam is accelerated electrostatically by a precision high voltage accelerator. The accelerator can operate at energies from *50* to *400 KeV*. The ions are mass separated in a *45* degree analyzing magnet and then pass through the injection beam line.

An estimation of the injection parameters for different ion species are summarized in *Tab. 2.3*.

Beam injection of heavy ions take place in one of the straight sections as shown in *Fig. 2.1*.

Table 2.3 - Parameters from Injection.

Ion Species	Li	Be	Mg	S	I	Au
Q	1	1	1	16	40	51
A	7	9	24	32	127	197
$\beta=v/c$	0.0117	0.0091	0.0034	0.185	0.11	0.099
Bρ [Tm]	0.25	0.25	0.25	1.17	1.135	1.196
Kin. Energy [MeV/u]	0.4	0.35	0.13	16.4	6.11	4.59
Number of Bunches	1	1	1	6	9	11
N_{inj} 10^7/bunch	200	200	200	2.1	0.5	0.375

For the demonstration of Crystalline Beams, the CHORDIS source can produce so intense beams of $^{7}Li^{+}$, $^{9}Be^{+}$ and $^{24}Mg^{+}$ that a single turn injection will be probably sufficient for the required intensities. The intensities of ion beams attainable out of a Tandem-ALPI complex might be not sufficient and it is necessary to adopt a multiturn injection scheme.

The same system deflecting the beam in at the injection, can also deflect the beam out at the moment of extraction.

2.2.1 The Multiturn Injection

The injection scheme here proposed for CSR operating in the Crystalline mode is the multiturn injection (MTI), like that already successfully experienced at Heidelberg (TSR) [BIS1, WAT1].

The beam has to be delivered by the injection line to the ring and receives a final kick by an electrostatic inflector which makes the injected beam trajectory parallel to that of the stored beam. The electrostatic characteristics of the inflector are not critical: the required electric field can be derived by the formula

$$E = \Theta \, Q \, (B\rho)^2 / l \, m$$

(Θ being the inflection angle, l the inflector length, Q/m the charge over mass ratio of the ion and $B\rho$ its magnetic rigidity). So as to require not too high electric fields from the parallel plate capacitor, θ_{in} had to be made small enough $(2 \div 3\,°)$ by means of proper dipoles upstreams; $(B\rho)_{max} = 1.5\ Tm$, $l=0.6\ m$ and the charge-over-mass ratio available from the linac imply a required E_{max} not higher than $6\ MV/m$, which is not critical over a $20 \div 30\ mm$ gap; the inner electrode has just to be thin enough to cut a mostly negligible part of the already stored beam during the injection procedure.

So as to fill the part of the machine acceptance which is devoted to the MTI cycle (A_{MTI}) efficiently, at the beginning of the process the closed orbit *(c.o.)* has to be distorted in order to coincide with the trajectory of the incoming beam, where the electrostatic septum is located. This is accomplished by proper dipoles *(bumpers)* of $0.4\ m$ length, symmetric with respect to the injection point; their role is to produce a kick of the closed orbit at a phase advance exactly equal to $\Delta\mu = -\pi/2$ before the inflector, and to compensate for it at $\Delta\mu=\pi/2$ downstreams. In such a way the closed orbit results unaltered in the rest of the ring. After the closed orbit distorsion has been performed, the field of the bumpers has to be reduced to zero in a time corresponding to about *60* beam revolutions in the ring (about 60 -$100\ \mu s$): A_{MTI} is thus filled very efficiently.

The CSR will have at least two operation modes, as pointed out previously, to both of which the injection scheme has to be applicable. The condition $\Delta\mu = \pm\pi/2$ for the position of the bumpers having to be valid in both cases, four bumper magnets are necessary in the ring. This configuration will allow to control the bump height and to correct the closed orbit distorsion by acting separately on two different families of bumpers (K_1 and K_2). Then the injection system will occupy three drift sections of the ring. The injection point is placed in the middle of a drift section where the dispersion function is maximum. The sextupoles housed in this section are cumbersome and impose a constraint on the position of the two bumpers of the first family allocated in the same drift section. Taking the injection point as the origin of the phase advance reference frame around the ring, the position of the K_2 bumpers has been fixed to $\Delta s_2 = \pm\ 1.4\ m$. This bumper family practically aims at correcting the closed orbit bump without affecting the central orbit elsewhere. The K_1 bumper family controls the real bump height at injection (fixed at $\Delta x = 5.2\ cm$) and has to be placed in the neighboring drift sections where points with β_x-function values as high as possible must be selected. However, the sextupoles still restrict the possible bumper positions to $\Delta l = \pm 1.4\ m$ from each drift section center. Therefore, with reference to the injection point, the position of the K_1 bumpers can be selected within the range $\Delta s_1 = \pm\ (7.2$ - $10.2)\ m$, as shown in *Fig. 2.6a*. This accomodation is represented by a circular diagram (the deflection kick of the bumpers upstream the two families are in opposite directions), as shown in *Fig. 2.6b*. For these values it is possible to obtain the required bump height minimizing the maximum deflection kick and, correspondingly, the maximum value of the magnetic

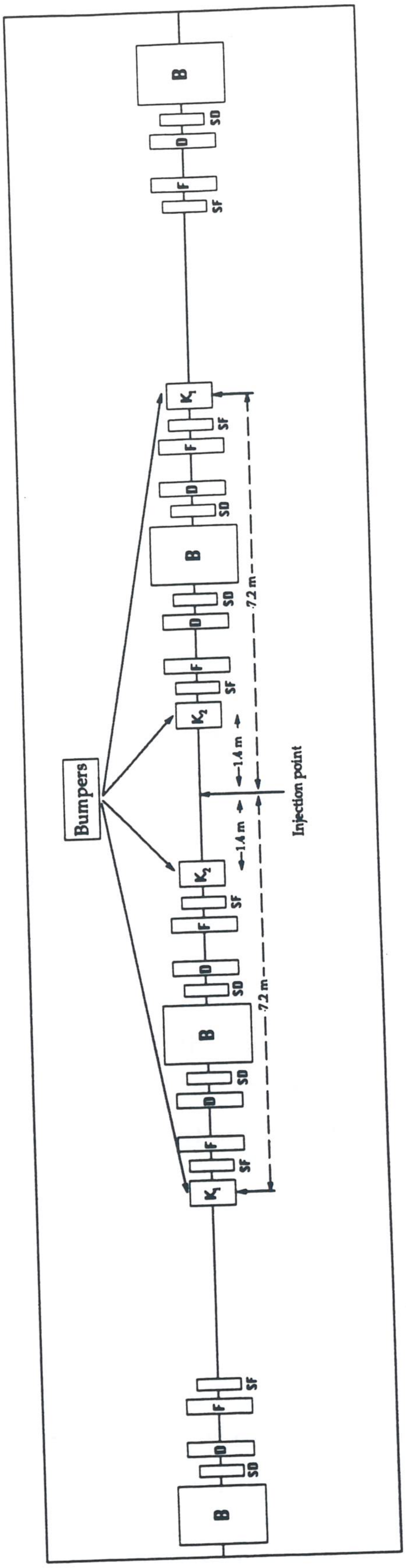

Fig. 2.6a - The injection system of CSR.

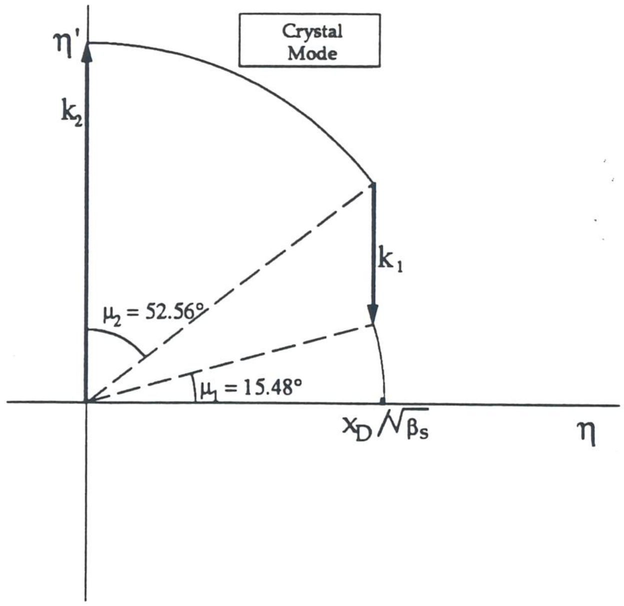

Parameter	Crystalline Mode
$\Delta\mu_1$	15.48^0
$\Delta\mu_2$	52.56^0
k_1	- 0.0109
k_2	0.0280
δ_1	$- 0.267^0$
δ_2	0.687^0
B_1	- 0.0175 T
B_2	0.0450 T

Fig. 2.6b - Circular diagram for the bumpers and their operation parameteres.

field required in the bumpers. In such a conditions the maximum deflection kick comes out to be $\delta_{max} = 0.88^0$. Assuming $(B\rho)_{max} = 1.5\ Tm$ at the injection, the maximum magnetic field in the bumpers will be $B_{max} = 0.0577\ Tesla$. Furthermore, with the same bump height at the injection point the maximum distance of the closed orbit with respect to the central one, is minimized. Results are shown in *Fig. 2.7*, where the displacement of the closed orbit around the ring is displayed for this bumpers accomodation.

In order to best exploit the horizontal acceptance, the required closed orbit deviation (at its maximum extension, i.e. at the inflector) is $x_D = 0.052\ m$.

As one MTI process is completed, the position of the closed orbit is still displaced outwards by $D(s)\delta_{inj}$ with respect to the geometric center of the vacuum chamber ($D(s)$ being the dispersion function along the ring and δ_{inj} the momentum displacement of the injection orbit).

The intensity multiplication factor achievable with the multiturn injection scheme is:

$$m = x_D^2/(D_T \varepsilon_0 \beta_{max})$$

where D_T is the dilution factor of the transverse phase space (taken equal to 2) and $\varepsilon_0 = 1\ \pi\ mm\ mrad$ is the emittance of the injected beam.

It can be easily shown that, if the whole acceptance is devoted to the MTI process, the result would be $m = 60$ that is big enough to obtain the desired intensities.

A more efficient injection scheme is represented by the combination of multiturn injection and radiofrequency stacking (RFS). The latter implies the use of a radiofrequency cavity with the direct consequence of increasing the ring impedance drastically. This fact can induce coherent instability in a coasting beam and prevent the formation of Crystalline Beams. For this reason, operations with coasting beams might exclude the insertion of an *RF* cavity in the ring. Whenever the storage ring will operate with bunched beams or in a different mode than the Crystalline one, the presence of the RF cavity will not

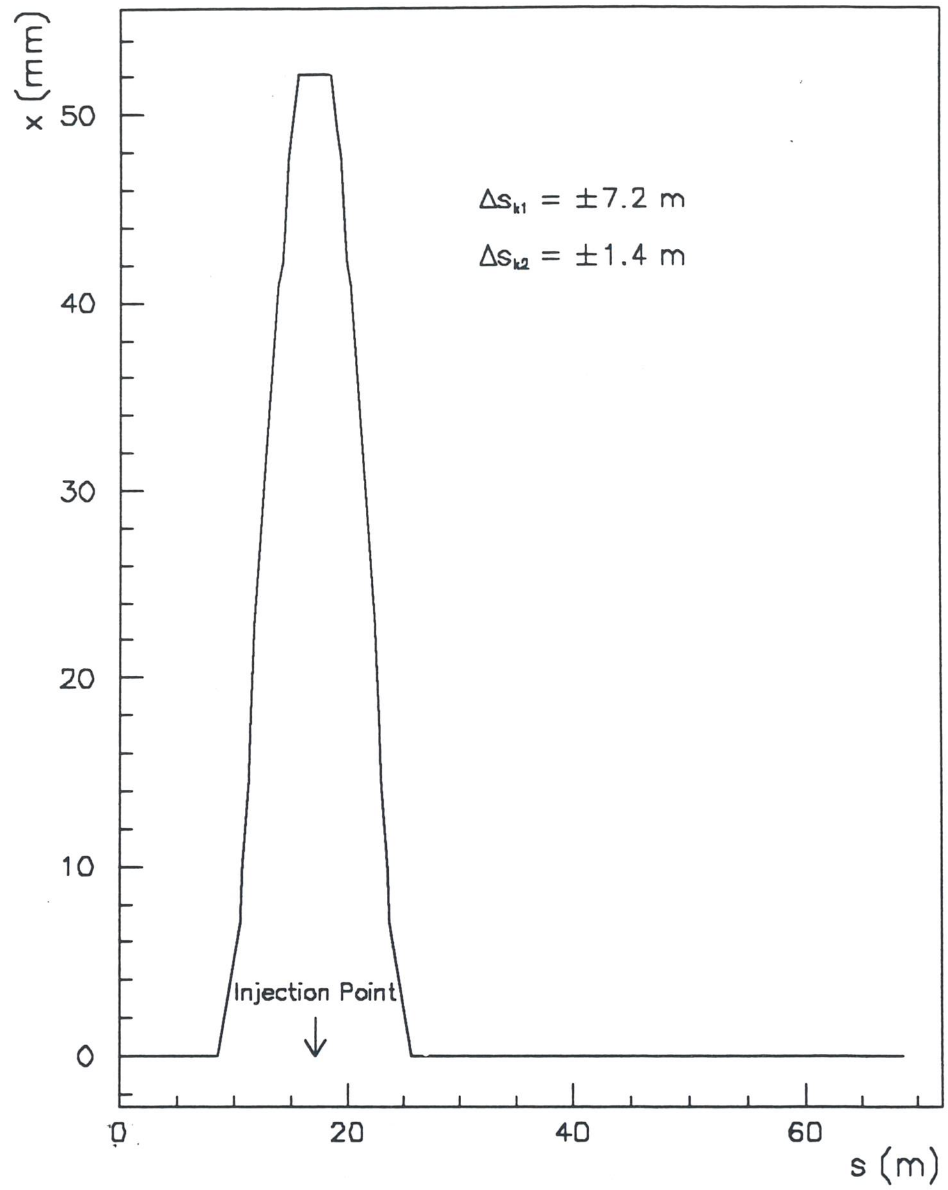

Fig. 2.7 - Displacement of the closed orbit at the injection.

rise any influence on the beam for what concerns the coherent instability connected to the impedance.

In this case, the combination of the multiturn injection and the radiofrequency stacking could be foreseen giving an intensity multiplication factor of about *150*.

The resonator which is periodically performing the momentum displacement of the multiturn-injected particles can be a traditional ferrite loaded single-gap cavity. Its working frequency has to be ranging between about *2* and *5 MHz* and a current change in the magnetization windings has to provide a fast frequency change of some percent. A maximum gap voltage of *1 kV* will be sufficient. The stacking cavity performs an adiabatic beam capture, a deceleration and a debunching when the top of the stack is reached.

2.3 The Magnet System

The Storage Ring lattice consists of *8* periods with *16* horizontally focusing quadrupoles (*QF*) and *16* horizontally defocusing quadrupoles (*QD*) and *8* bending dipoles. In addition, *32* sextupoles are also inserted to correct the chromaticity.

Initial designs for the quadrupoles and the dipoles are presented in the following sections. They should not be considered as final designs but they may be used for initial layouts and sizing.

2.3.1 Dipole Design

The main parameters are listed in *Table 2.4* and the typical layout is shown in *Fig. 2.8*.

They are *C*-type to get a vacuum chamber with offtakes for pumps in addition to the extentions for the alignement.
Given the nominal field of *1.5 T* and a gap height of *80 mm*, special attention will be paid to the dimensioning of the magnet circuit in order to avoid iron saturation that could cause field distortion. The iron has to be characterized by good

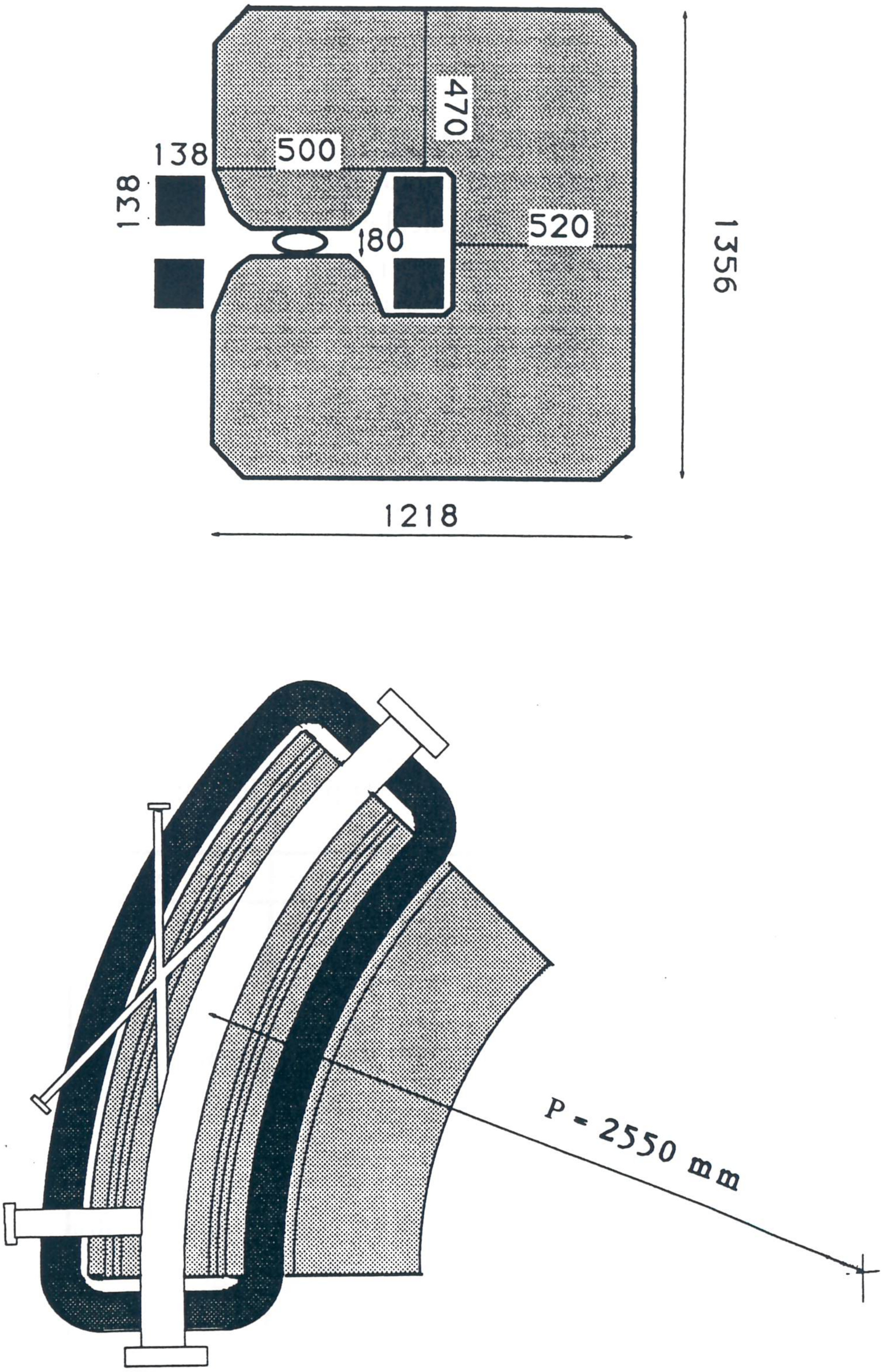

Fig. 2.8 - A sketch of the dipole magnets.

saturation properties. It has been necessary to increase the pole width to obtain a good uniformity ($\Delta B/B_0 < 10^{-4}$) at different field values ($B_{min}= 0.1$ T, $B_{max}= 1.5$ T) in the vacuum pipe region.

The coils will be made up with *10.5 x 10.5 mm²* water cooled hollow conductors (central cooling hole *7 mm* diameter). Every coil is arranged in six pancakes, with *24 turns* and four layers each. All pancakes are electrically in series and the cooling circuits are parallel-connected; the selected maximum current density is *4.86 A/mm²*. The total dissipated power in the dipole system is *410.4 kW.*

The dipoles have been designed for DC operation mode.. They must be modified by using laminated core (lamination thickness: *0.35 mm*) to minimize iron current losses if an AC operation mode is required. It could be necessary to reduce the pole width, reducing the homogeneous field area width in order to minimize the total stored energy and therefore the peak power.

Table 2.4 - Basic Dipole Parameters.

Parameter	Symbol	Unit	Values
Type			Curved C
Number of Magnets			8
Max. nominal Field	B_{max}	T	1.5
Bending Angle	θ	Degrees	45
Bending Radius	ρ	m	2.55
Geometrical Length	L_{dip}	m	2.0
Gap Height	g	mm	80
Current	I	A	340
Voltage	V	V	151
Power	P	kW	51.3
Total Weight		ton	21

2.3.2 Quadrupole Design

Quadrupoles in the Storage Ring have a length of *0.25 m* and a maximum design gradient of *12.3 T/m*, consistent with the magnetic rigidity. The fully symmetric quadrupole cross-section is shown in *Fig. 2.9*, while *Table 2.5* lists the fundamental parameters.

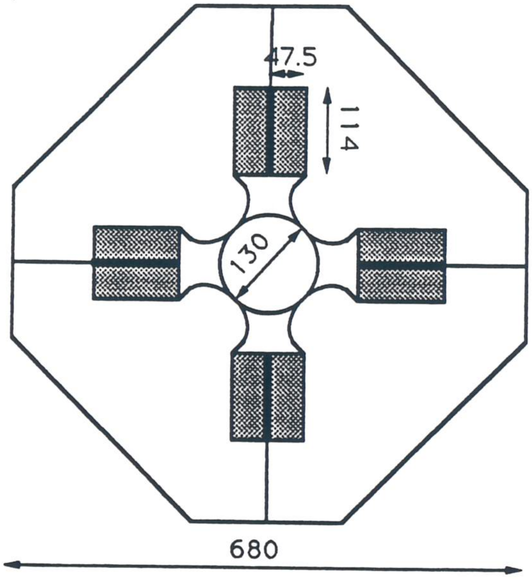

Fig. 2.9 - A sketch of the quadrupole magnets.

The maximum field gradient of *12.3 T/m* gives a maximum pole tip field of *0.8 T*. It is necessary to avoid iron saturation by shaping properly the return joke because of the high field. The quadrupoles , being four-fold symmetric, are cut in four identical pieces.

The coils will be made up with *9.5 x 9.5 mm²* water cooled hollow conductors (central cooling hole *4.5 mm* diameter). Every coil is arranged in *60* turns and twelve layers. All the coils are electrically in series and the cooling circuits are parallel-connected; the selected maximum current density is *4.72* A/mm^2.

The total dissipated power in the quadrupole system is *270 kW*.

Table 2.5 - Basic Quadrupole Parameters.

Parameter	Symbol	Unit	Values
Number of Magnets			32
Max. Field Gradient	G_{max}	T/m	12.3
Max Pole Tip Field	G_p	T	0.8
Geometrical Length	L_{quad}	mm	250
Aperture Diameter	g	mm	130
Number of Turns/pole	Np		60
Current	I	A	350
Voltage	V	V	24
Power	P	kW	8.4
Total Weight		kg	750

The quadrupoles have been designed for DC operation mode. They must be modified by using laminated core (lamination thickness: *0.35 mm*) to minimize iron current losses and slightly changing the yoke shape to minimize the total stored energy if an AC operation mode is required.

2.3.3 Power Supplies

The proposed solution has to provide two power supply busses, for each one of the QF and QD quadrupoles (two families). The quadrupoles of each family are powered in series. All dipoles are powered independently.

The DC power supplies are conventional and their main parameters are listed in *Table 2.6*; a digital programmed mode of operation is necessary for a possible slowly pulsed operation mode, in this case suitable power supplies must be provided.

Table 2.6 - Total Power Supplies Requirements

Parameters	Unit	Values
N. of Dipole Power Supplies		8
Total Output Power	kW	411
Total Input Power	kVA	514
N. of Quads Power Supplies		2
Total Output Power	kW	270
Total Input Power	kVA	338

In order to mantain a stable machine operation, mainly at the Crystalline mode, the ripple of the power supplies has to be better than 10^{-5}.

2.4 The Cooling System

Very efficient phase-space cooling is required to attain crystalline ion beam i.e. beams with very small temperature (in the rest frame system), compared with the average Coulomb interaction energy. Two techniques of cooling are applied to the CRYSTAL Storage Ring: electron cooling and laser cooling (see *Fig. 2.1*).

Electron and/or laser cooling are needed to attain Crystalline Beams since their features complement each other.

Electron cooling provides a phase-space contraction for an ion beam, through the overlapping of an ultracold electron beam, continuously renewed. Coulombian scattering forces between ions and electrons equalize the temperatures of the beams and allow to attain a relatively low momentum spread $\Delta p_p/p = 10^{-5} \div 10^{-6}$. Notice that assuming an electron beam longitudinal temperature of $e^2 n_e^{1/3}$, the ion plasma parameter after cooling will be $\Gamma_i = Q^2 (n_i/n_e)^{1/3}$. If the electron and ion densities are of the same order of magnitude, then the critical value for Crystalline Beams of $\Gamma_i = 170$ is reached when $Q^2 > 13$.

Laser cooling acts by virtue of momentum exchange between an ion beam and laser light, whose frequency is chosen in correspondence with values of the electric dipole for the stored ions. Photon excitation and subsequent re-emission causes, in principle, longitudinal momentum $\Delta p_p/p$ even three orders of magnitudine lower than in the electron cooling case. This latter method has a working regime that recommends a precooled ion beam; the former can therefore be considered as complementary to the laser cooling. Furthermore, in the present storage rings, laser cooling acts only along the longitudinal axis, so that transverse cooling is bound up to electron cooling efficiency. To increase the cooling efficiency in the transverse planes a new method for transverse laser cooling has been developed. In addition, laser cooling of bunched beams is a new and very promising technique for longitudinal phase space compression. With this method also the indirect cooling of transverse dimensions can be effectively increased. It is also clear that the laser cooling makes a decisive selection on the kind of ion to be employed. For these ion beams, electron cooling reduces emittance and momentum spread without decreasing the ion current, allowing the application of laser cooling on a dense ion beam with still enhanced efficiency.

2.4.1 Electron Cooling

The electron cooling is a well known and tested technique for cooling ions in storage rings [POT1]. The efficiency of the method is strictly related to the electron beam parameters. A typical electron cooling device suitable for CSR is presented in the following section; the design parameters are reported in *Table 2.7.*

In general, a cooling device may be divided in three sections:

1) electron gun, where the electrons are produced and accelerated;

2) drift section, where the electron beam are merged with the ion beams at the same relative velocity, after being bent by a toroid;

3) collector; which has to recover the electrons without disturbing the electron and ion optics

Table 2.7- Electron Cooler Design Parameters.

Parameters	Symbol	Value
Electron Energy Range [keV]	E_e	1-20
Electron Current [A]	I_e	0.1 -1
Cathode diameter [mm]	ϕ_c	40
Gun Perveance [μP]	P_g	2
Transverse Electron Temperature [eV]	T_e	0.1
Length of Cooling Section [m]	l	1
Magnetic Field [T]	B_0	0.2
Collector Perveance [μP]	P_C	5
Relative Current Loss	I_{loss}/I	$<10^{-5}$
Dissipated Collector Power [W]	W_C	100
Average Vacuum Pressure [Torr]	P_{gas}	10^{-10}

The Electron Gun

Electrons are emitted by resistively heating a flat disk thermionic cathode. The cathode is surrounded by a Pierce electrode [PIE1] and followed by *7* ring shaped electrodes. The immersed-flow configuration (magnetized electron) compensates the space-charge blow-up and transverse energy heating due to optic errors. The gun has a perveance of $2.3\ \mu P$. The extraction by Pierce optics compensates at the first stage the space-charge effect, the first electrode provides a fixed current extraction. The second electrode supplies an electric field which compensates the defocusing effects of the anode hole. After the extraction, the electrons may experience the acceleration fields of the following electrodes in the Pierce optics, adiabatic acceleration [ALE1]] or resonant acceleration [KUD1].

The different accelerating methods improve the parameters related to the beam temperature, therefore they influence the cooling time of the ion beams. A simulation of the accelerating structure done by the code Slacgun [HER1] is represented in *Fig. 2.10*. The results give information on trajectories and heating of the beam due to optics errors. It results that the optic disturbances, already for low magnetic field (few hundred Gauss), are lower than the thermal transverse temperature (*0.1 eV*).

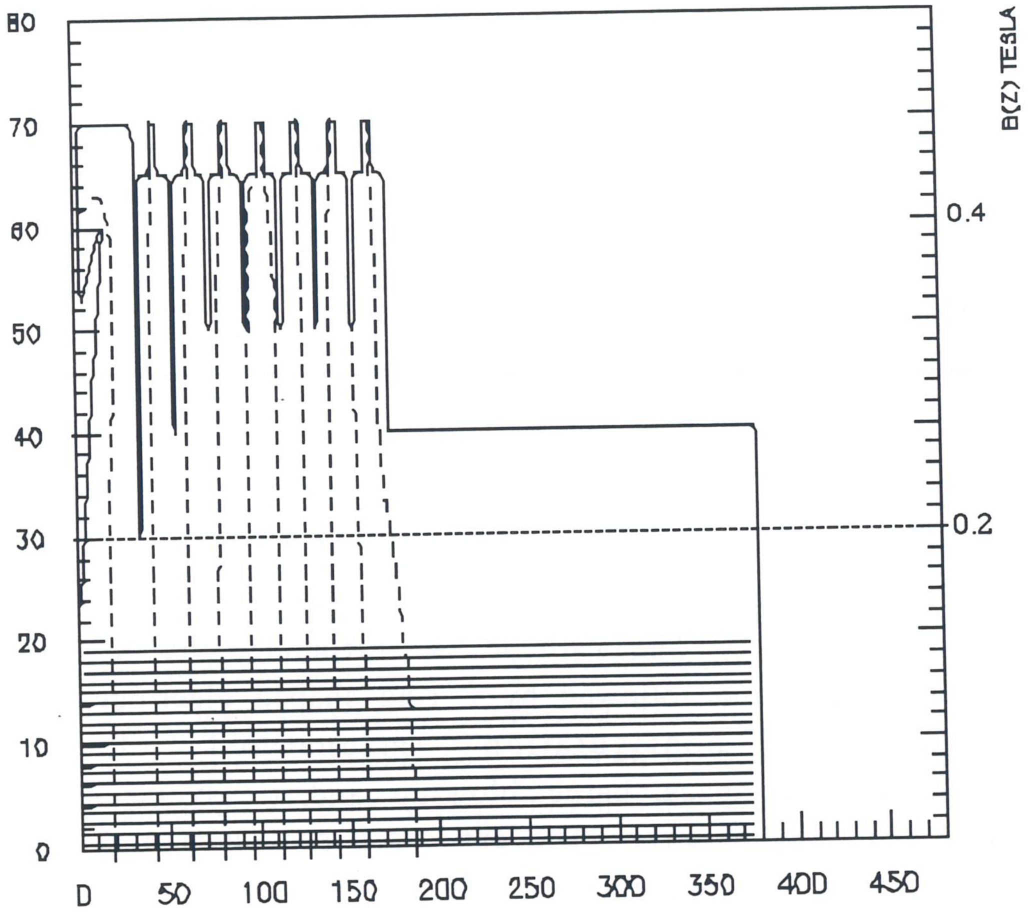

Fig. 2.10 - Trajectory simulated by Slacgun (E_e = 10 keV, B_0=2 kG).

The Drift Section

After extraction and acceleration, the electron beam experiences the bending magnetic field provided by toroids and dipoles. At the junction between solenoid and toroid the magnetic field is reduced and needs correction in order to avoid transverse heating in the boundary of the beam. Then the electrons are merged with the ion beam, which has a lower initial diameter. The alignment between the beams needs big care. The cooling time for different kind of ions is calculated by the formula [DIK1]:

$$\tau = \frac{A\ e\ \beta_0^4\ \gamma_0^5}{Z^2\ 4\pi r_e r_p\ \eta\ J_e\ L_C}\ \theta^3,$$

Where r_e and r_p are the electron's and proton's classic radius, Z the charge state, A the mass number of the particle being cooled, η the ratio of the electron beam length to the ring circumference, $L_C=15$ the Coulomb logarithm, β and γ the relativistic factors for the beams, J_e the electron beam density. The divergence θ, is due to the contribution of longitudinal and transverse ion and electron temperature:

$$\theta^2=\theta_i^2+\theta_e^2$$

The total divergence for CSR results less than *1 mrad*. *Table 2.8* shows the calculated cooling time for different ions at the injection energies.

In the low temperature range ($T_i < T_e$), the contribution to the cooling time is mostly due to the electron temperature. By adiabatic acceleration [ALE1] it is possible to reduce the longitudinal temperature and suppress the transverse-longitudinal relaxation by a strong magnetic field. The adiabatic expansion provides a reduction of the transverse beam temperature of the electron beam [DAN1]. Both methods contribute to enhance the cooler performance.

The cooling section affects the ion beam optics. The solenoidal confining magnetic field induces a rotation of the beam around its axis. This effect provides a coupling between the two transverse planes; this results in a lowering of the betatron oscillation limit. The toroids give a component of magnetic field perpendicular to the ion beam, requiring correction dipoles to compensate for the deflection.

Furthermore, the electron beam acts on the ion beam like an electrostatic lens. For a constant perveance gun the tune is independent from the electron energy.

Table 2.8 - Cooling Time for Different Ions.

	Li	Be	Mg	I	Au
Z	1	1	1	40	51
A	7	9	24	127	297
β	0.07	0.07	0.07	0.11	0.1
γ	1.0025	1.0025	1.0025	1.006	1.005
Energy [kev]	1.28	1.28	1.28	3.1	2.6
τ [ms]	29	42	112	2	1.2

The Collector

After the interaction the electrons pass through the toroid, and are decelerated and captured by the collector. The collector potential is close to the cathode one. The electrons are decelerated in order to dissipate lower power and to prevent secondary electron emission. But the lower the collector potential the higher the probability to have reflection of primary or secondary electrons. Primary and secondary electrons, accelerated backwards, excite the transverse energy of the beam in their travel forwards and backwards in the cooling section.

The parameters required for the collector are: perveance of $5\ \mu P$, current loss lower than 10^{-5} and dissipated power $100\ W$. These features are accomplished by applying a magnetic mirror spreading the electron beam on the collector surface and reflecting the electrons which may travel in the opposite direction [SHA1].

Hollow Cathode Electron Cooling Device

The hollow cathode electron cooler [SHA2] is an electron cooling device without bending magnets (toroids). The electron beam is generated by a ring shaped cathode immersed in the opposite magnetic fields of two solenoids (cusp configuration). In such a way the cathode ring lies in the magnetic field plane of symmetry. A cylindrical electron beam with a small bore in the center is generated and accelerated with the same technique used in a standard device. After travelling through the cooling region the electron beam is decelerated and recovered in a collector. The collector has a central hole on the bottom to allow the ion beam to circulate in the storage ring.

The hollow cathode device presents a few practical advantages. Compared with a conventional device, the physical space occupied by this device is reduced and a cooling region of double length can be housed in the same straight section. The high voltage potential can be directly applied to the cooling section (not strictly required), simplifying the high voltage power supply and control systems. At the ends of the cooling section the ion beam is not deflected by the transverse magnetic field (no toroids) and correcting dipoles are not required. Finally, adopting the hollow cathode configuration the cost of the cooler could be considerably reduced.

Actually, a full-scale prototype is under study and only experimental results will give clear indications about the possibility of using a hollow cathode electron cooler in a storage ring. A schematic drawing of the device is presented in *Fig. 2.11*. Such a prototype was designed to fulfill the CSR requirements and the corresponding parameters are presented in *Table 2.9*.

The test was developed in two steps: the first dedicated to the analysis of the beam characteristics, the second to have better insight into current and energy distributions.

A troublesome feature of the system is the presence of a region, near the axis, where electrons experience violation of the adiabaticity condition. Nevertheless a reduction of the disturbed region (< *3 mm* diameter) was found out by applying a negative potential to a special tube shaped electrode (gun-reflector) [SHA2]. A gun perveance of $20\ \mu P$ has been measured.

After the interaction section the beam is cleared out from the axis by the magnetic field of the solenoid end and captured by a hollow collector. A special tube shaped electrode (collector reflector) provides to suppress the current loss through the hole and reflected back to the interaction region. The experimental results give a relative current loss $< 10^{-4}$ for a $30\ \mu P$ collector perveance.

Table 2.9 - Design Parameters of the Prototype.

Electron Energy range [keV]	1 - 20
Magnetic Field range [kG]	0.2 - 2
Beam Current range [A]	0 - 2
Beam Diameter [mm]	30
Relative Current Loss	$<10^{-5}$
Collector Voltage range [V]	300-900 V
Vacuum [Torr]	$<10^{-10}$

The design parameters reported in *Table 2.9* have been achieved. A vacuum pressure lower than 10^{-9} Torr has been obtained during the operations. A better vacuum can be easily obtained by improving the pumping speed.

In order to measure current and energy distributions a longitudinal energy analyzer [ALE2] replaced the collector. Steering coils are mounted in the drift section in order to move the beam across the analyzer surface. The measured beam characteristics outside the disturbance region are in agreement with the theoretical predictions [MYA1] and comparable with the experimental results for conventional coolers.

The energy distribution measurement are done by the retarding potential method [KUD2]. This measurement provides information on the energy displacement of the average value of the distribution $\Delta W_{\parallel}$ from the reference potential W_0 (cathode potential) and the width of the distribution $\delta W_{\parallel}$. These parameters give also information on longitudinal and transverse temperatures of the beam.

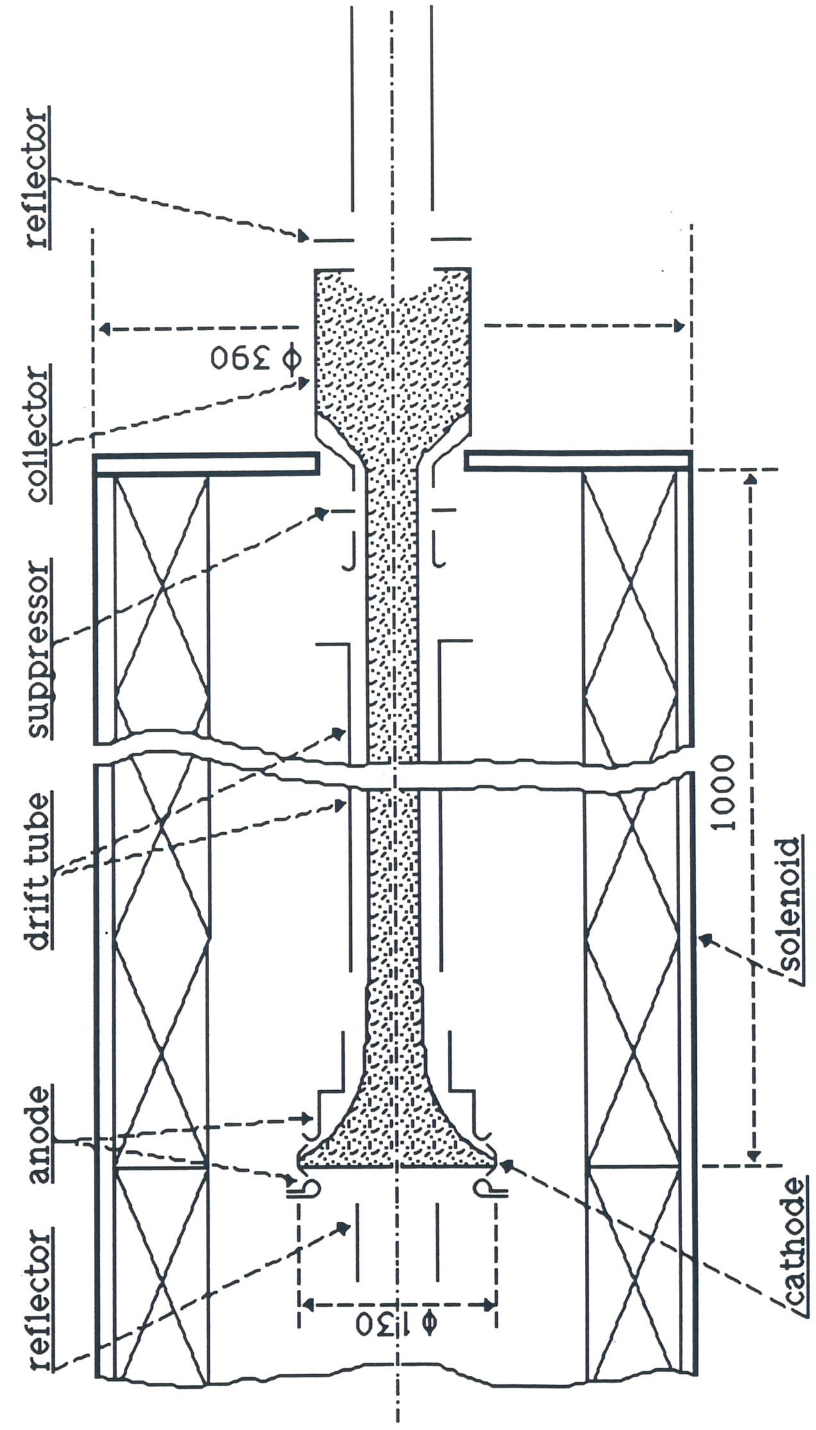

Fig. 2.11 - A sketch of the hollow cathode device.

$\Delta W_{//}$ is affected by parasitic contribution and coherent contribution [LAP1]. The coherent contribution is kept up by scanning the electron beam and recording $\Delta W(r)$. The variation of $\Delta W_{//}$ along the radial coordinate gives the transverse coherent energy of the beam; the parasitic effects show instead background contributions.

The displacement of the average of the energy distribution $\Delta W_{\parallel}$ is drawn in *Fig. 2.12*. In the region outside of the disturbed trajectories, the electrons has a transverse temperature lower than *0.2 eV*.

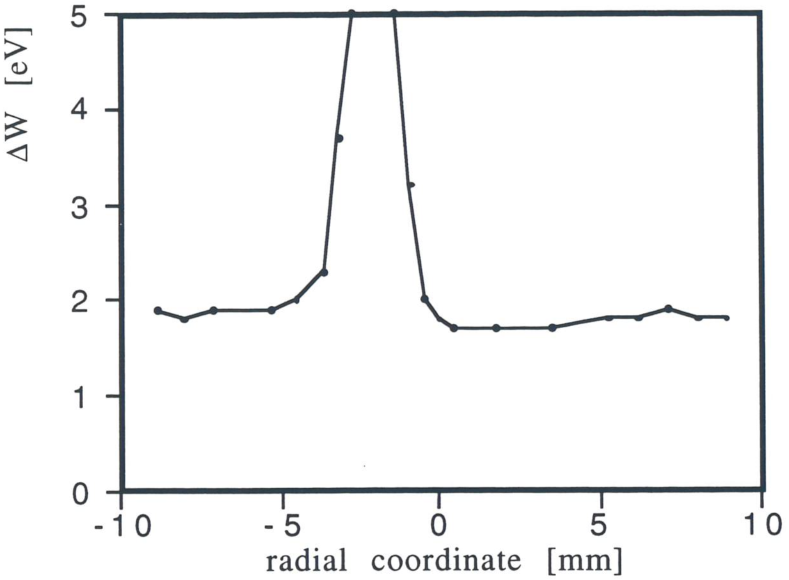

Fig. 2.12 - Displacement of the average of the energy distribution curve along the radial position.

The longitudinal energy is diplayed in *Fig. 2.13*, as a function of the beam current, for an electron beam energy of *20 keV*.

The physical dimension of the disturbance region depends on the fact that the magnetic field symmetry plane is placed outside the cathode at a certain distance from the emitter edge, so that a paraxial region is free from electrons. A more accurate geometric positioning of the solenoids will allow to reduce the size of the disturbance region considerably [SHA3]. Furthemore, the gun perveance is quite big and this can induce a heating of the beam, which is the main responsible for the relatively high temperatures measured on the prototype.

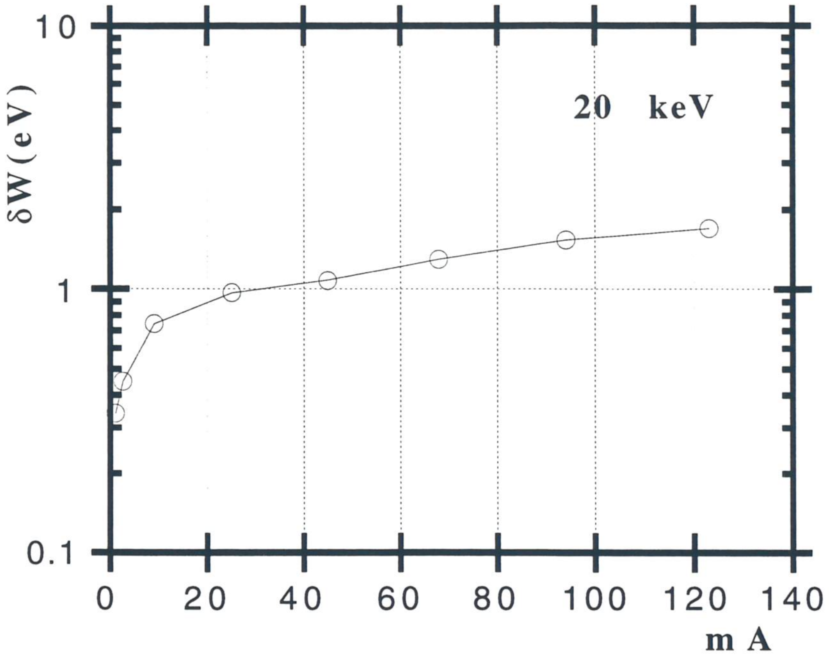

Fig. 2.13 - Longitudinal energy in function of the beam current, for electron energy of 20 keV.

2.4.2 Laser Cooling

Standard laser cooling of ion beams is a very powerful method to reach very low longitudinal temperatures [HAN1]. Its basic principles and techniques are well known. It is the result of velocity-selective transfer of photon momentum from a laser beam to a moving ion. The laser cooling technique is effective if the selected ion has a strong dipole transition from a stable or metastable state to an excited one. Obviously the required wavelength should be accessible to the laser technique. The ion species used in storage rings so far are: $^{7}Li^{+}$, $^{9}Be^{+}$ and $^{24}Mg^{+}$.

One possible technique for longitudinal laser cooling consists in superimposing two counterpropagating laser beams on the ion beam in one of the straight sections of the ring. The frequencies of the two lasers are set, after the different Doppler shifts have been taken into account, to the opposite sides of the Doppler linewidth of the ion. The two laser frequencies are then swept across the Doppler width. In this way the velocity distribution of the ions is compressed to the centre of the Doppler line. The suitable set-up concerning the longitudinal laser cooling for CSR (see *Fig. 2.14*) was extensively discussed in *Ref.* [TEC1]. In the following, more attention is dedicated to a new proposal for transverse laser cooling.

Transverse Cooling.

In order to overcome the problem of the short interaction time between ions and light when the beams are mutually orthogonal, a scheme is proposed where almost all the ions stay on resonance with the laser during the full time they cross the laser beam, i.e. they are on resonance regardless their velocities. This can be achieved considering a suitable broad-band laser whose spectrum is so large as to cover about one half of the Doppler profile of the ions. In this way no laser tuning is needed and the ions experience the radiation pressure each time they cross the laser beam, independently of the perturbations they have undergone in the storage ring. A second important point is that the optical pumping problems due to the ground state level structure are avoided when using a broad-band laser.

Let us assume that the cooling laser is directed along the transverse x-direction; all ions whose velocity component v_x is negative are on resonance with the red detuned laser and, therefore, are under cooling. If the laser beam is reflected backward through a mirror, then also the ions with positive velocity component will be on resonance. The same argument holds true for cooling of the other transverse degree of freedom provided that another laser beam is used.

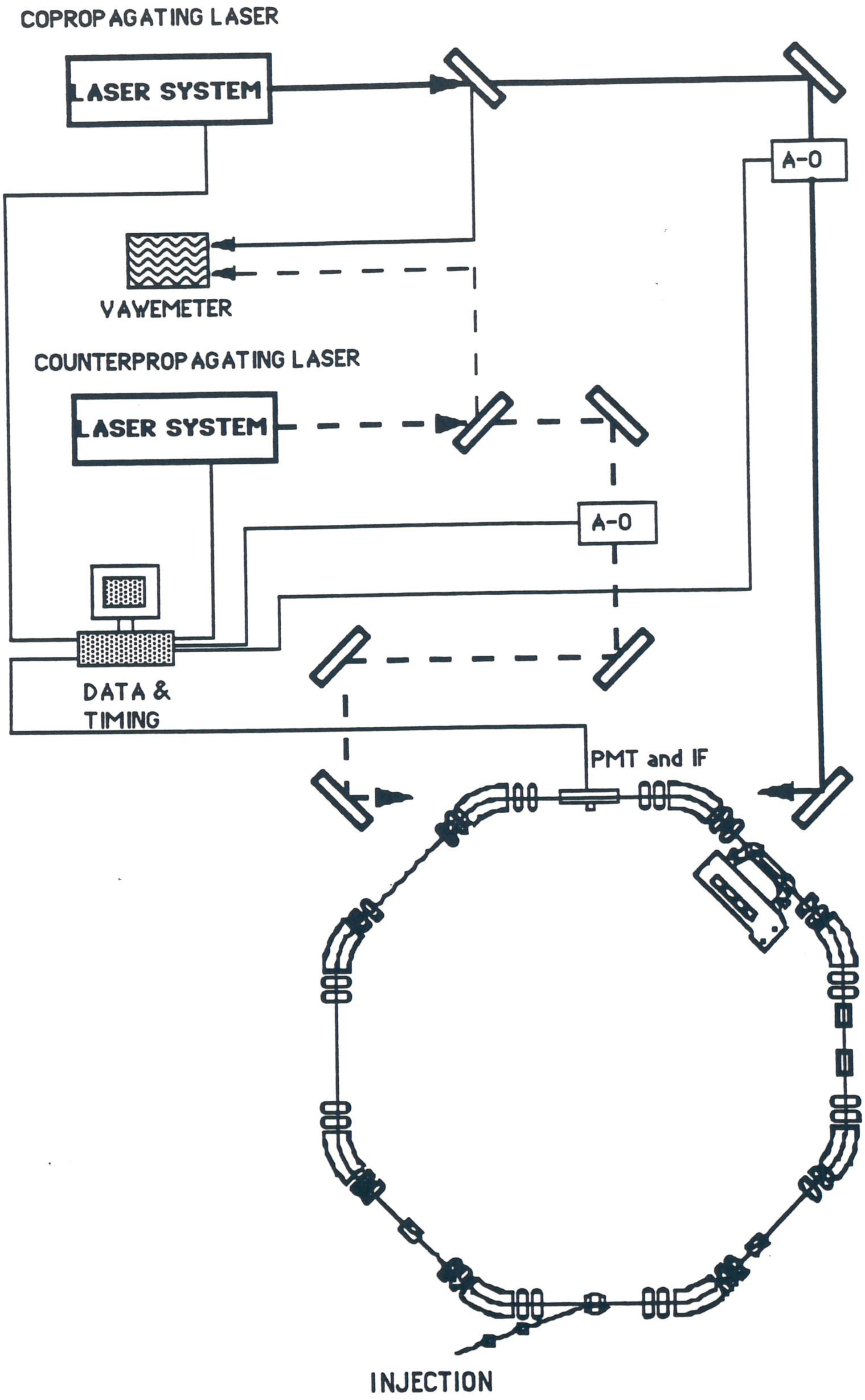

Fig. 2.14 - Proposed Set-up for the Longitudinal Laser Cooling.

As the interaction time is very short (i.e. of the order of few tens of *ns*) ions undergo a pulsed excitation which imposes the calculation of the probability p of excitation to the upper level at each turn of the ion about the storage ring. In first approximation, p is a function of the interaction time $t_{int}=L/v_L$ (where L is the length of the ion beam-laser overlapping region and v_L the ion longitudinal velocity) and of the Rabi frequency Ω_R:

$$p = \sin^2\left(\frac{\Omega_R t_{int}}{2}\right) \qquad (1)$$

By introducing the excited level lifetime τ and the saturation parameter $S=I/I_S$, where I is the laser intensity and $I_S = \pi hc/\lambda^3\tau$ is the saturation intensity (λ being the laser wavelength, c the speed of light and h the Planck constant), the Rabi frequency becomes

$$\Omega_R = \frac{1}{\tau}\sqrt{\frac{S}{2}} \qquad (2)$$

Let v_P denote the initial transverse velocity of ions. With the above assumptions the number of turns which are necessary to set an ion with zero transverse velocity is given by the number of photons the ions has to absorb divided by the number of photons absorbed at each crossing with the laser beam. This holds:

$$n = \frac{M v_P \lambda}{h p} \qquad (3)$$

where M is the ion mass. The cooling time T_{cool} is n times the revolution period, $T = L_S/v_L$ (L_S being the ring length). T_{cool} depends essentially on two correlated parameters, the interaction time t_{int} and the saturation parameter S. Then T_{cool} holds:

$$T_{cool} = \frac{v_P}{v_L}\,\frac{ML_S\lambda}{h}\left\{\frac{1}{\sin\sqrt{\dfrac{LW_0\lambda^3}{8\pi qDhc\tau v_L^2}}}\right\}^2 \qquad (4)$$

where D is the transverse size of the overlapping region, W_0 the laser power and q the number of longitudinal modes of the laser.

In order to demonstrate the feasibility of the proposed method we discuss the cases of $^7Li^+$ and $^{24}Mg^+$ ions confined in the ASTRID Storage Ring at Aarhus [NIE1], the main parameters of which are reported in *Table 2.10*. The chosen values of β will be obtainable also at CSR. In *Table 2.10* the cooling times for given values of W_0 are given, assuming $L=5\ cm$ and $D=1\ mm$. Laser powers are *1.5 W* at *548 nm* for cooling of $^7Li^+$ and *100 mW* at *280 nm* for $^{24}Mg^+$. The first one is obtainable from commercially available dye-lasers. A comment is necessary about the UV laser. A power of about *100 mW* at *280 nm* in continuous operation has already been obtained by frequency doubling a dye-laser in an external cavity [NIE2]. No reference instead exists in literature about the possibility of doubling a multi-mode laser as the one we suggest to use. A careful theoretical and experimental investigation is therefore requested about this point.

The proposed technique can be considered as complementary to indirect cooling (see section on TSR progress), to be used both together with indirect cooling itself for high density beams and alone for low density beams. Concerning the first case, the technique can be employed to complete the cooling process once indirect cooling has brought the ion beam to low temperatures where intrabeam scattering is more effective. On the other hand, the high densities necessary for indirect cooling process are no more requested for this direct cooling. The diffusion process due to intrabeam scattering, which is the main source of heating for high density beams, can be overcome by the use of very low density beams. Working with a number of particles of the order of 10^5 - 10^6 the heating rate due to intrabeam scattering is negligible and the main sources of heating are the collisions with the residual gas and the statistical nature of the spontaneous force. From *Table 2.10* it emerges that the technique allows to subtract from the system about *200 K* in one second: this value is sensitively larger than the expected heating rates due to the two processes mentioned above.

Table 2.10 - Main Parameters for Transverse Ion Cooling.

Parameter	$^7Li^+$	$^{24}Mg^+$
lower state	$2s\ ^3S_1$ (F=5/2)	$3s\ ^2S_{1/2}$
upper state	$2p\ ^3P_2$ (F=7/2)	$3p\ ^2P_{1/2}$
lifetime of lower state (s)	50	stable
lifetime of upper state τ (ns)	43	3.5
transition wavelength λ (nm)	548	280
natural linewidth $\Delta\nu_H$ (MHz)	3.7	45
total laser linewidth $\Delta\nu_L$ (GHz)	1.9	2.1
laser cavity length L_c (m)	6.8**	3.3
number of longitudinal modes q	270**	47
laser intensity per mode* I (mW/cm^2)	11.1	4.2
total laser power W_0 (W)	1.5	0.1
saturation intensity I_S (mW/cm^2)	8.8	810
saturation parameter $S=I/I_S$	1.26	5.2×10^{-3}
interaction time t_{int} (ns)	30	56
excitation probability p	0.075	0.16
transverse velocity v_P (m/s)	1.1×10^3	5.7×10^2
Doppler cooling limit (mK)	0.089	1.08

* The laser intensity is calculated by assuming that the laser beam is focused to a rectangular spot, with *L=5 cm* and *D=1 mm.*

** The number of longitudinal modes and the laser cavity length is calculated by considering also the power broadening and the short interaction time.

Alignment and Divergence Problems.

The minimum achievable temperature is bound to the frequency detuning between resonance frequency (center of Doppler profile) and that of the sharp edge $\Delta\nu_o$:

$$T_{\min} = \frac{1}{k_B}\frac{mc^2}{8\ln 2}\left(\frac{\Delta\nu_0}{\nu_0}\right)^2 \qquad (5)$$

The ultimate transverse temperature is also affected by the precision of the $90°$ angle between laser and ion beams. If ϕ is the (small) deviation of this angle from $90°$, the 1^{st} order Doppler shift is:

$$\nu_l' = \nu_l\,(1+\beta\phi) \qquad (6)$$

Taking this effect into account, the detuning from resonance of the sharp edge side of the laser profile becomes:

$$\Delta\nu = \Delta\nu_o + \nu_l\beta\phi \qquad (7)$$

This means that, due to this small deviation, the frequency of the laser can be moved either towards the blue region, giving origin to heating process, or towards red, corresponding to a smaller possible reduction of the Doppler profile of the ion beam.

For the practical situation of ASTRID, the angle ϕ must be smaller than 0.36 *mrad* in order to have $\Delta\nu - \Delta\nu_o < 1$ *GHz*. A realistic value for alignment precision is *1 mrad*. The effect can be compensated in experiments by properly varying the laser frequency in order to drive the displacement of the laser frequency back to its reference value $\Delta\nu_o$.

Another source of error is the unavoidable divergence of a gaussian laser beam $\theta = \dfrac{\lambda}{\pi\omega_L}$. This effect has the following consequences in the cylindrical focalization system (*5 cm x 2 mm*). In x - y plane, where the waist is smaller the divergence is about *1 mrad*, taking into account the initial transverse velocity of the ions, a starting Doppler shift of less than *5 MHz* has to be expected, and this value is decreasing as the cooling proceeds. In x - z plane the divergence of the beam is much less (< 0.02 *mrad*), due to its larger waist, accounting for the longitudinal velocity of the ions the expected Doppler shift is less than *100 MHz*. This can cause a small heating in the longitudinal direction, where in any case it is counteracted by the strong laser cooling force.

Longitudinal Cooling with Broad Band Laser

The use of a white laser may drive to a sensitive improvement in laser cooling in longitudinal direction. An experiment employing a white laser in the longitudinal direction is foreseen to be implemented at TSR in Heidelberg.

Longitudinal laser cooling of a coasting beam at TSR is performed in a scheme which employs a fixed frequency single mode laser in combination with an auxiliary force realized with an induction accelerator (see section on TSR progress). A loss of cooled ions out of the velocity capture range of cooling force occurs, which can be explained by single binary collisions transferring a large amount of kinetic energy out the transverse direction of motion into the longitudinal one. For $^9Be^+$ the problem was solved by extending the capture range of the force by means of the method of FBE; the same method was not as successful with $^7Li^+$. The use of a white laser will be an optimal solution to extend the capture range of the force and to increase the number of laser cooled ions.

For the case of a bunched beam, the extension of the capture range of the force leads to a decrease of the cooling time. Bunched beam laser cooling with a single mode fixed frequency laser presents two distinct regions depending on ion energy (see section on TSR progress). The first one, of slow cooling corresponds to the region where the RF-force is stronger than spontaneous force, so that the ion oscillates with the slow synchrotron frequency (*140 Hz*) spiralizing through the center of the phase space bucket. In the second region, being the spontaneous force stronger than RF-force, the ions are very rapidly driven to a stable point with the reference energy. Sensitive improvements have been obtained in cooling times for $^9Be^+$ with the use of FBE.

The use of a white laser should allow a reduction of cooling times also for $^7Li^+$, overcoming the problem of waiting for slow synchrotron oscillation to bring ion in resonance with the laser.

Laser Characteristics

We shall now discuss how it is possible to produce a laser whose frequency spectrum suites the requirements for transverse laser cooling as indicated above. The "white-light" atom cooling has been proposed by Moi [MOI1] and successfully achieved by many groups [GOZ1, STR1, ZHU1, LIT1], which adopted different solutions for the practical realization of the broad-band laser.

Here it is proposed to realize the "white" cooling by means of "long-cavity" multi-mode dye laser with a total linewidth $\Delta\nu_L$ and a frequency separation between the longitudinal modes $\Delta\nu_M = c/2L_c$, L_c being the laser cavity length. If the laser is resonant with a two level atom or ion, whose homogeneous absorption linewidth is $\Delta\nu_H$, then the "white-light" condition is reached when $\Delta\nu_M < \Delta\nu_H$ and $\Delta\nu_L > \Delta\nu_D$, with $\Delta\nu_D$ = Doppler linewidth. All ions are instantaneously on resonance, regardless of their speed, and all ions experience the radiation pressure during all the time they cross the laser beam. Standard dye lasers have a $\Delta\nu_M$ of the order of $300\text{-}400\ MHz$, i.e. too large for most cases (for example $\Delta\nu_H$ for sodium is $10\ MHz$). Therefore the length of the laser cavity L_c has to be prolonged in order to afford every longitudinal mode to be sufficiently close to its neighbors, according to the equation:

$$L_C = c/2\Delta\nu_H = \pi\, c\, \tau \qquad (8)$$

Such kind of laser has been realized by Liang et al. [LIA1] and by Moi and collaborators [MOI2] and laser cooling of a Na beam has been experimentally observed [GOZ1]. In this case the laser cavity length was $L_c = 15\ m$.

In *Table 2.10* the length of the laser cavities for transverse laser cooling of the two selected ions are reported. The laser cavity for $^7Li^+$ should be, according to equation (*8*), $L_c=40$ m but, when the power broadening of the absorption line and the line broadening due to transient interaction time are taken into consideration, L_c is reduced to less than *7 m*. In order to cool an ion beam with a transverse temperature of about *500 K*, the bandwidth of the laser should be of the order of *2 GHz* (see *Table 2.10*).

Sharp edge Problem

One of the problems of white-lasers, whose bandwidth shows, in general, a Gaussian profile, is the lack of a natural sharp edge in the frequency domain, which limits the achievable lowest temperature. Many solutions can be adopted as already checked through experimental investigation, [GOZ1, HOF2]. Here a possible approach is given as an example. If the laser cavity length is reduced, the frequency mode separation becomes larger than the homogeneous linewidth of the ions and the cooling process stops because the automatic shift from one node to the next one does not work any more. But, if the laser power density W_L is high enough to broaden the atomic line, the condition of white light can be again established. W_L can be chosen in such a way that only the central modes satisfy the white light condition, while all others do not. The ions are decelerated, switching from one mode to the next, until the mode intensity is large enough, then the cooling stops suddenly.

Progress in Laser Cooling Experiments at TSR

Experiments concerning laser cooling of energetic ions at the TSR have been continued. Laser cooling was concentrated on quantitative investigation of heat transfer between the hot transverse degree of freedom and the directly cooled longitudinal one. This process takes place due to Coulomb collisions in the beam ("intrabeam scattering"). The direct longitudinal cooling in combination with the heat exchange between the coupled degrees of freedom leads to an indirect but remarkably efficient transverse cooling. Accordingly, one observes an increasing longitudinal temperature because of stronger heating due to equilibration.

In addition to these studies on coasting beams a new cooling scheme was established at the TSR: bunched beams, laser cooling where the electric field in a RF-cavity provides the auxiliary force in addition to the resonant scattering force. In this scheme, the cooling experiments are no longer limited in time and the capture range is extended by about two orders of magnitude.

Indirect Transverse Cooling.

The Coulomb interaction between the ions leads to a coupling between the longitudinal and the transverse degrees of freedom which becomes stronger by increasing the particle density. The heat-exchange between the degrees of freedom drives, by means of direct longitudinal cooling, to a reduction of the the beam transverse temperature.

The mechanism of indirect transverse cooling has been studied on a coasting beam of about 10^7 ions of $^9Be^+$ at an energy of $7.3\ MeV$. Suitable starting conditions for the laser cooling process are reached by electron precooling the beam for about $6\ s$. This reduces the ion beam temperature to about $T_{long} = 300\ K$ for the longitudinal degree of freedom, $T_{hor} = 4000\ K$ and $T_{vert} = 500\ K$ for the transverse ones. Laser cooling is then performed in the following way: the ions are decelerated by an induction accelerator (INDAC) until they come into optical resonance with a fixed frequency cooling laser. Here the laser cooling sets in and the ions are kept in a force balance between the resonant accelerating laser force and the costant decelerating INDAC force. A loss of laser cooled ions out of the velocity capture range of the cooling force occurs. This can be explained by single binary collisions transferring a large amount of kinetic energy out of the transverse motion into the longitudinal one. In order to maintain the high densities necessary for indirect transverse cooling, the method of the Extended Capture Range (FBE) has been adopted [WAN1]. The FBE is based on the adiabatic excitation of the ions by means of properly shaped and biased drift tubes and drives to a drastic reduction of particles losses (see *Fig. 2.15*).

The transverse temperatures of the ion beam have been derived from measurements of the transverse beam radius, performed by means of a Beam Profile Monitor (BPM) [HOC1].

The longitudinal velocity distribution has been detected by means of HV-scans [PET1]. *Fig. 2.16* shows the time development of the beam temperature for 2×10^7 stored ions. An effective cooling in the transverse degree of freedom, due to coupling of the degrees of freedom, can be clearly seen. Thermalization brings together an enhancement of the longitudinal temperature, as the coupling causes an enhanced heating rate. Although by this measurements with extended

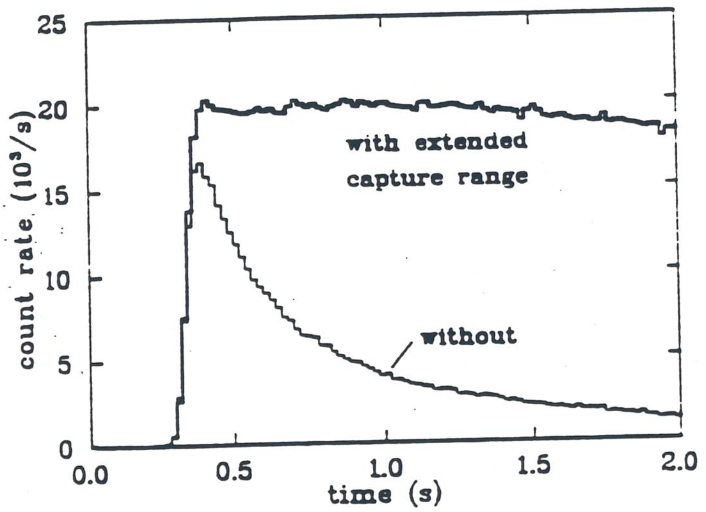

Fig. 2.15 - Temporal evolution of laser fluorescence intesity of cooled ions which is proportional to the number of cooled ions.

capture range only a relatively low cooling rate can be obtained ($\Lambda_{long}=100\ s^{-1}$), equilibrium temperatures have been measured in all three degrees of freedom to be below those observed with electron cooling alone. The estimated transverse cooling rate, calculated as ratio between transversal heating rate and equilibriium temperature, is $\Lambda_{tr} = 1\ s^{-1}$.

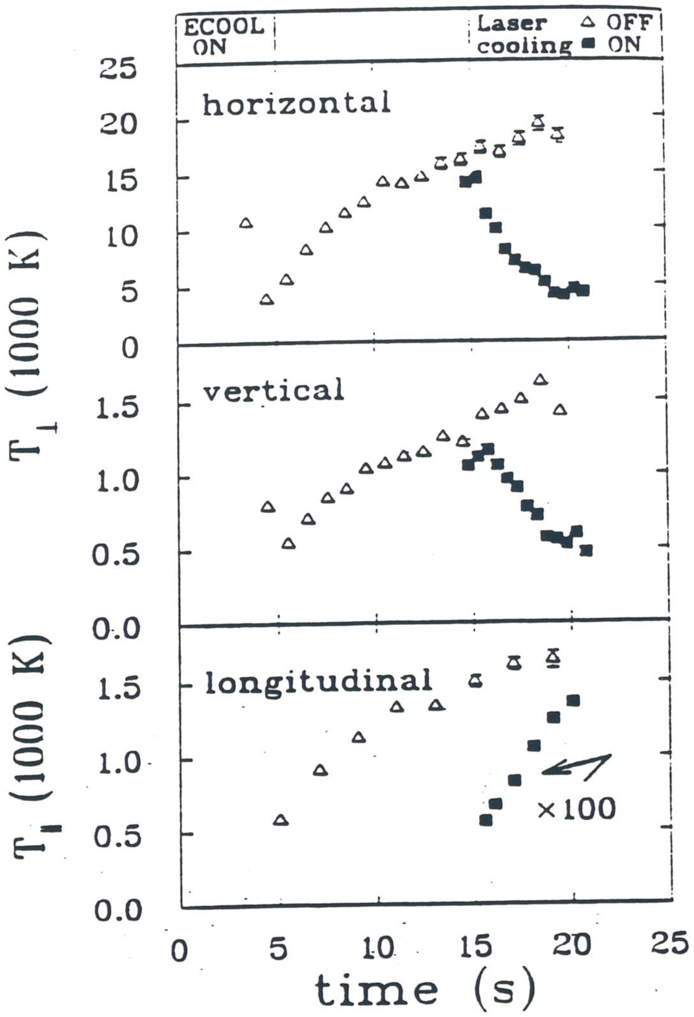

Fig. 2.16 - Temporal evolution of the beam temperature in the three dimensions for $2x10^7$ stored ions of $^9Be^+$.

Laser Cooling of Bunched Ion Beams

Laser cooling of bunched ion beams is a new and very promising techinque for longitudinal phase space compression. The velocity capture range can be extended by a factor *100* with respect to the old cooling scheme with the induction accelerator. By increasing the particle density the cooling rate can be increased as well as the indirect transverse cooling.

The method makes use of the electric field of an RF-cavity to obtain the auxiliary force necessary to reach the stable point. The RF-cavity is used to bunch the injected ion beam. The frequency of the RF potential defines an ideal velocity (the synchronous velocity) for ions in the storage ring. For ions having velocity (or phase) errors relative to the synchronous particle, the RF potential represents a quasi harmonic restoring force in the longitudinal phase space. These particles undergo oscillations (synchrotron oscillations) in energy and phase relative to the synchronous particle. Ion motion in the single bucket can be described in longitudinal phase space by ΔE (distance from synchronous energy) and $\Delta\psi$ (distance from synchronous phase). Let us consider now the case in which ions interact with a copropagating laser beam, which is red detuned with respect to the synchronous particle. By means of synchrotron oscillations the ions come periodically into resonance with the laser, absorb photons and are slightly accelerated. This process alters the phase space trajectory, making the ion run in a more internal trajectory and making it spiralize towards the center of the bucket. Since the RF-restoring force becomes weaker as $\Delta\psi$ decreases, when the ions reach a given phase with respect to the synchronous particle they cannot move any longer through laser resonance. They are then driven by the laser force to a stable point where they possess the sychronous energy ($\Delta E=0$) and have a definite phase $\Delta\psi\neq 0$. In this point they experience equilibrium between spontaneous and RF forces. The whole process leads to a damping of synchrotron oscillations and to a reduction of the temperature of the particles (see *Fig. 2.17*).

Fig. 2.18 shows the configuration used for bunched beam cooling at TSR. The ring itself is described in *Ref.* [PET1]. The employed beam consisted of about 10^7 ions of $^{9}Be^{+}$ at *7.3 MeV* properly precooled by electron cooling. The RF-cavity was operated at the 8th harmonic of revolution frequency (*225 KHz*). Due to very low longitudinal emittance of the beam after electron cooling, the RF-cavity was operated at very low voltages, typically less than *5 V* peak. This last is a very crucial parameter, as the cooling time exhibits a strong dependence on the peak voltage and decreases decreasing it.

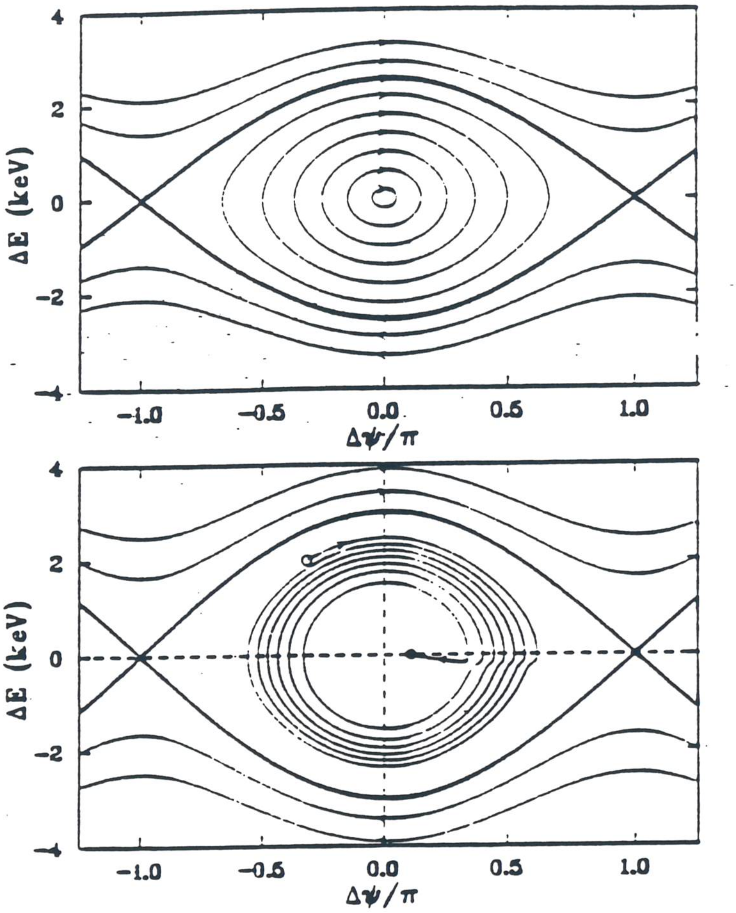

Fig. 2.17 - Ion motion in phase-space for bunched beams without cooling (above) and with laser cooling (below).

Measurements have been carried out for different laser detunings ΔE_L [MAD1]. The space structure and the velocity distribution of the bunched beam have been monitored by means of pick-ups and HV-scans respectively. In *Fig. 2.19* a typical velocity distribution can be seen. In this measurement a single bunch shows a cooled ion distribution on a hot ground of uncooled ions, composed by *2/3* of all the ions. Despite the spatial compression of about *1/3*, with a correspondingly enhancement of the longitudinal density, the high cooling rate

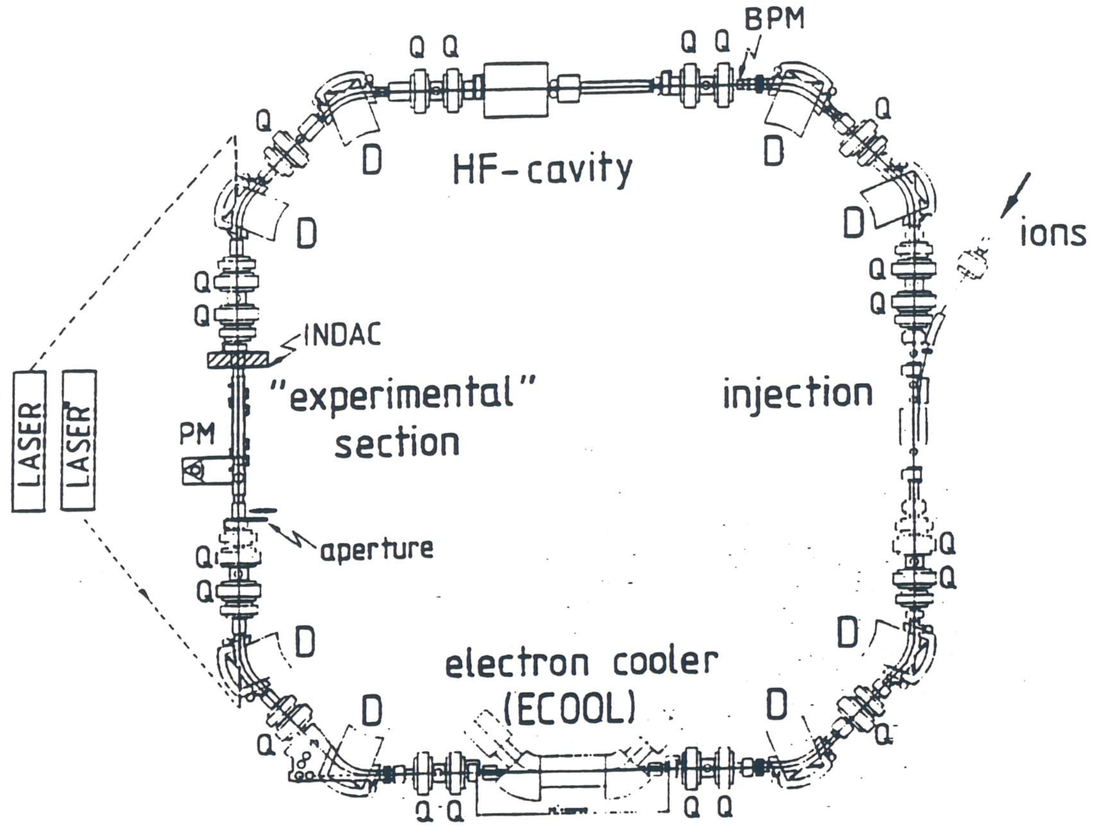

Fig. 2.18 - The storage ring configuration used for bunched beam cooling at TSR.

of $\Lambda_{long} > 50000\ s^{-1}$ allowed to obtain of a longitudinal temperature below $100\ mK$ for the cooled distribution. In the same picture also the dependence of the longitudinal temperature on the detuning of the laser ΔE_L from the synchronous energy is shown. An optimum cooling is reached for $\Delta E_L = -5\ eV$. *Fig. 2.20* shows the spatial structure of the ion distribution.

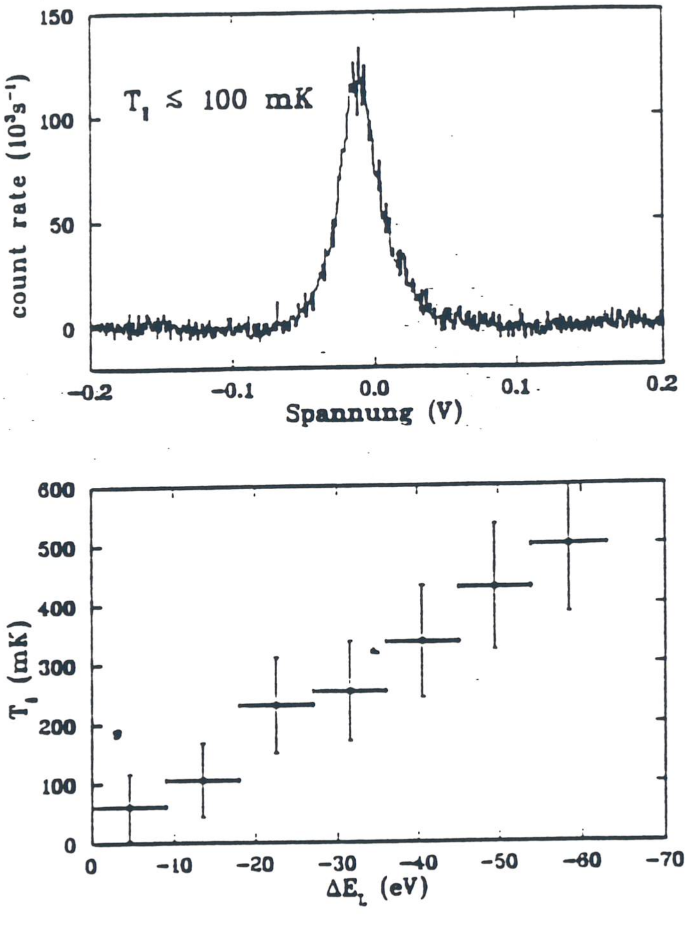

Fig. 2.19 - HV diagnostic scan of the bunched laser cooled $^9Be^+$ ion beam for optimum detuning of the laser: $\Delta EL=-5\ eV$ (above) and longitudinal temperature in function of laser detuning (below).

By means of indirect cooling a significant reduction of transverse temperature has to be expected. At the moment, however, no device exists which could allow a direct measurements of the transverse temperature (beam profile monitor measurements do not allow to investigate temperatures below *1000 K*).

Most recent experiments exhibits cooling of all the ions to a longitudinal temperature lower than *200 mK*.

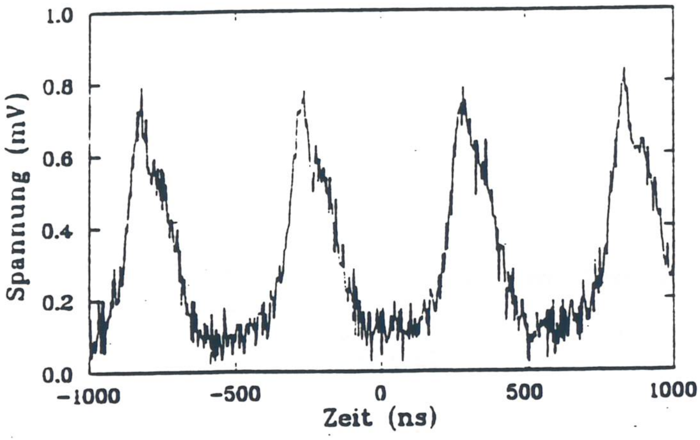

Fig. 2.20 - Typical output of the Pick-ups for the spatial distribution of the laser cooled beam (ΔE_L=-5 *eV*).

2.5 The Vacuum System

In many cases the lifetime of a beam is limited by reactions with residual gas (see chapter *6* in *Ref.* [TEC1]). The most important effects are the loss, and the capture, of electrons by scattering on residual gas. Single and multiple Coulomb scattering are also limiting the ion beam lifetime.

In order to avoid considerable beam losses, the storage ring is designed for operation in the 10^{-12} *Torr* region. This vacuum level can be achieved and mantained in a *2.5 mm* thick stainless steel vacuum chamber. The bending magnets aperture give a good conductance over all their length. Dipole magnets are connected by a cylindrical pipe of *13 cm* radius which extends through the quadrupoles. The vacuum chamber in the straight sections is also cylindrical with the same radius of *13 cm*. To reach such a vacuum level all equipment inside the vacuum environment has to be designed and treated very carefully. Only stainless steel and aluminum oxide had to be used, as well as copper seals in all flanges. In order to remove mainly H_2 hidden inside the materials, the whole equipment has to be heated to $900\ ^0C$ before the installation. In addition after the installation the system should be baked to $300\ ^0C$ with simultaneous pumping.

The pumping system makes use of conventional pumps for ultrahigh vacuum, namely cryogenic and ion pumps with the addition of non-evaporable getters. Vacuum ports are located in each of the bending magnets, with an aperture of about *10 cm* to which ion pumps are attached. Four cryogenic pumps would be sufficient for all the system.

Vacuum pressure gauges can be located in the wall facing the vacuum port, in principle at every location, though probably one reading per arc and one per straight section will be sufficient. One gas analizer is necessary to determine the chemical composition of the residual gas.

Vacuum valves have to be located with the goal to provide easy access and operation and to leave sections of the beam pipe under vacuum when specific locations are opened at atmospheric pressure for maintenance or repair. Considering the size of the ring and its geometry, it is sufficient to provide high quality remotely controlled vacuum valves in each straight section as well as at each end of the electron cooling device.

References

[ALE1] A.V. Aleksandrov et al.; Phys. Rev. A 46 (1992) 6628.

[ALE2] A.V. Aleksandrov et al.; Meas. Sci. Technol. 4 (1993) 764.

[BIS1] G. Bisoffi et al., Nucl. Instr. Meth. A287 (1990) 320-323.

[BJO1] J.D. Bjorken and S.K. Mtingwa; Part. Acc. 13 (1983) 115.

[CON1] M. Conte and M. Martini; Part. Acc. 17 (1985) 1.
R. Giannini, INTRABS Computer code, CERN PS 1993.

[CRA1] K.R. Crandall and D.P. Rusthoi, TRACE-2D: An Interactive Beam Transport Code, LA-10235-MS, UC-32.

[DAN1] H. Danared et al.; Phys. Rev. Lett. 72 (1994) 3775.

[DIK1] N.S.Dikansky et al.; Report INP 88-61.

[GOZ1] S. Gozzini et al.; Appl. Phys. B 54 (1992) 428.

[GRO1] H. Grote, The MAD Program, CERN/SL/90-13 (AP).

[HAN1] T. Hänsch and A. Schawlow, Opt. Com. 13 (1975) 68.

[HER1] W.B. Herrmannsfeldt SLAC electron optics programm M.Sedlack Vax-Version. CERN January 1985.

[HOC1] B. Hochadel et al.; Nucl. Instrum. and Meth. A 343 (1994) 401.

[HOF1] I. Hofmann, L.J. Laslett, L. Smith and I. Haber; Particle Acc. 13 (1983) 145.

[HOF2] J. Hoffnagle; Opt. Lett. 13 (1988) 102.

[KUD1] V.I Kudelainen et al.; Sov. Phys. Techn. Phys 16 (1972) 1821.

[KUD2] V.I Kudelainen et al.; Sov. Phys. JETP 56 (1982) 1191.

[LAP1] R. Lapik et al.; Proc. of the Workshop on Beam Cooling and Related Topics; Ed; J. Bosser CERN 94-03 (1994) 164.

[LIA1] J. Liang, L. Moi, C. Fabre; Optics Comm. 52 (1984) 131.

[LIT1] I.C.M. Littler et al.; Zeit. Phys. D 18 (1991) 307.

[MAD1] M. Madert; MPI Heidelberg, Diplomarbeit (1995).

[MYA1] D.G. Myakishev et al.; Int. J. Mod. Phys. A 2B (1993) 915.

[MOI1] L. Moi, Opt. Comm. 50 (1984) 349.

[MOI2] L. Moi, M. Allegrini, P. Bicchi, S. Gozzini, J.H. Xu, SPIE 701 (1987) 176.

[NIE1] J.S. Nielsen et al.; Proc. of the Workshop on Beam Cooling and Related Topics, Yell. Rep. CERN 94-03 p. 339 and references therein.

[NIE2] J.S. Nielsen to be published.

[PET1] W. Petrich et al., Phys. Rev. A 48, 2127 (1993).

[PIE1] J.R. Pierce; Theory and Design of Electron Beams, (ed. D. Van Nostrand Company, Princeton)

[POT1] H.Poth; Phys.Rep. 196 (1990) 135.

[SHA1] A.N. Sharapa and A.V. Shemyakin; Nucl. Instrum. Meth. A 351 (1994) 295.

[SHA2] A.N. Sharapa and A.V. Shemyakin; Nucl. Instrum. Meth. A 336 (1993) 6.

[SHA3] A.N. Sharapa and A.V. Shemyakin; Electron Cooling Device without Bending Magnets, INP Preprint 90-110, Novosibirsk 1990.

[STE1] K. Steffen; High Energy Beam Optics, Wiley, New York.

[STR1] P. Strohmeier et al.; J. Opt. Comm. 73 (1989) 451.

[TEC1] L. Tecchio et al. (CSR Collaboration); CRYSTAL: A Storage Ring for Crystalline Beams; LNL-INFN (REP) 80/94.

[WAN1] B. Wanner et al.; Proc. Workshop on Beam Cooling and Related Topics, Montreaux 1993, ed. J. Bosser, CERN 94-03, Geneva 1994.

[WAT1] S. Watanabe et al.; Nucl. Instr. Meth. A271 (1988) 359.

[ZHU1] M. Zhu et al.; Phys. Rev. Lett. 67 (1991) 46.

3

Beam Instabilities

A variety of instabilities (transverse and longitudinal) can occur in a storage ring. The existing literature [LAC1] discusses all of them quite extensively.

The most important instabilities to be considered are the transverse ones, since they lead to immediate particle losses. When the beam emittance is reduced, space-charge shifts the working point towards a resonance, leading to a fast transverse beam growth and loss.

Coulomb scattering between particles in the beam can couple one phase plane to another and transform the common longitudinal motion of the particles into transverse energy spread.

Landau damping is largely decreased by cooling and it cannot always compensate the blow-up of the ion beam.

The cooling of the momentum spread to very low values can also produce longitudinal instabilities. They are mainly related to the resistivity of the walls surrounding the beam.

Reactions between the ion beam, the residual gas and the electron beam also cause important beam losses in a storage ring.

Non-linear, single-particle phenomena and collective effects have been studied in connection with their implications on the design of the storage ring lattice.

All these phenomena were quite extensively studied in a previous report [TEC1]. Here, instability phenomena connected to the ring impedance, that more strongly influence the formation of Crystalline Beams, are discussed in details.

Estimations are given for $^{7}Li^{+}$ and $^{24}Mg^{+}$ that can be laser cooled to very low temperatures. As an example of ion with high charge state, the $^{197}Au^{51+}$ is also considered.

3.1 Ring Impedances and Instabilities

The performances of a storage ring, especially in the case of very cold and intense beams, is limited by coherent instabilities. Ions generate an electromagnetic field that acts back on the beam after interaction with its surroundings. If a perturbation exists, that could be enhanced by this field causing an unstable process.

The parameter that takes into account beam-surrounding interaction is the coupling impedance. Therefore the estimation of transverse and longitudinal coupling impedances is very important in order to evaluate the stability limits.

Measurements carried out show that impedances can be modeled as follows [LAC2]:

A) - the space charge impedance.

B) - the resistive wall component;

C) - the parasitic low $Q \approx 1$ resonators with broad band component such as: 1) bellows, 2) vacuum pump ports, 3) kicker and septum, 4) vacuum chamber cross-section variation, 5) diagnostic devices like beam profile monitors and, 6) electron beam impedance (electron cooler);

D) - the parasitic high $Q >> 1$ resonators with narrow band component (higher longitudinal mode in cavities);

In addition, the impedance contribution of bellows and strip line beam position monitors have to be taken into account. Electron beam impedance will be calculated in a dedicated section.

Storage ring and beam parameters are shown in *Table 3.1* and *Table 3.2*, (symbols are defined in *Table 3.3*).

Calculations are carried out considering different cases: string and zig-zag configurations, two beam radii and a certain range for ion speeds.

Table 3.1 - Storage Ring Parameters.

Max. Magnetic Rigidity	4 Tm	Number of Ions N	$10^5 \div 10^7$
Circumference	68.8 m	Chromaticity	-0.72
Gamma Transition	1.76		
Beam Pipe Radius *b*	0.065 m		

Table 3.2 - Beam parameters. Beam radii are related to ion beams having horizontal and vertical emittances of $\varepsilon_x = \varepsilon_y = 1\,\pi$ *mm mrad* and $\varepsilon_x = \varepsilon_y = 10^{-3}\,\pi$ *mm mrad*. Radii have been calculated by using TRACE-2D code. Parameters are related to minimum (first three rows) and maximum ion speed (last three rows).

		β	γ	Frequency (kHz)
	Mg_{24}^{+1}	0.03÷0.0535	1.00045÷1.00143	131÷233
Ions:	Li_{7}^{+1}	0.03÷0.181	1.00045÷1.0168	131÷789
	Au_{197}^{+51}	0.1÷0.316	1.005÷1.054	436÷1379

Ions	Beam Radius max (m)	Beam Radius min. (m)	g max	g min	Phase slip factor	Skin depth (m)
Mg	3,00E-03	1,00E-04	13,43	6,63	0,6763	1,18E-03
Li	3,00E-03	1,00E-04	13,43	6,63	0,6763	1,18E-03
Au	3,00E-03	2,00E-04	12,04	6,63	0,6672	6,48E-04
Mg	3,00E-03	1,00E-04	13,43	6,63	0,6743	8,81E-04
Li	3,00E-03	1,00E-04	13,43	6,63	0,6444	4,79E-04
Au	3,00E-03	1,00E-04	13,43	6,63	0,5773	3,62E-04

Table 3.3 - Symbols used.

P=Harmonic of the perturbing wave;
b=Radius of the beam pipe;
R_S=Shunt impedance of resonators;
ω_0=Revolution frequency;
a=Average beam radius;
R=Average radius of the storage ring;
A=Ion mass;
I=Ion current;

δ_0=Skin depth;
Z_0=377 Ω;
ω_c=Cut-off freq.
$\omega=P\omega_0$;
g=1+2ln(b/a);
K=Wave vector;
q=Ion charge;
$|\eta|=\frac{1}{\gamma^2}-\frac{1}{\gamma_{tr}^2}$;

$Z_{L,T}$=Longitudinal and transverse impedance.

3.1.1 Coupling Impedance

The problem of impedance estimation previously solved in the ultra-relativistic limit [CHA1], has been treated for non relativistic beams in *Ref.* [BUR1]. The equations show that the resistive wall impedance (RW) and the resonator one can be represented with their ultra-relativistic relations multiplied by a non-relativistic damping factor:

$$f(\kappa)=\kappa\frac{K_1(\kappa)I_0(\kappa)-K_0(\kappa)I_1(\kappa)}{I_0^2(\kappa)} \qquad \text{RW damping factor}$$

$$\frac{1}{1+g/g_{eff}}\frac{1+\beta^2}{2}f(\kappa) \qquad \text{Resonator damping factor}$$

where $\kappa=Kb/\gamma$, K_m and I_m are modified Bessel functions and g/g_{eff} is related to the field penetration depth into the wall as a function of beam speed.

Let us now estimate the non relativistic damping factor for these two cases [BUR1]:

1) the RW impedance reaches its maximum for $\kappa=0.43$. For this value, $f(\kappa)=0.73$ and harmonic $P=94.16\gamma$;

2) at resonance, near the pipe cut-off frequency, $f(\kappa)\approx\pi\ exp(-4.8/\gamma\beta)$. Broad Band (BB) impedance is completely negligible since even for higher ion speed, $\beta=0.316$, $f(\kappa)=1.7x10^{-6}$.

In the following RW impedance will be evaluated at its maximum.

Longitudinal impedance

According to *Ref.* [LAC2] it is possible to estimate longitudinal impedance from the following relations*:

A) $$\frac{Z_{RW}}{P}=(1-j)\frac{Z_0\beta}{2b}\delta_0\frac{1}{\sqrt{P}} \qquad 1a)$$

B, C) $$Z_{BB}=\frac{R_s}{1-jQ\left(\frac{\omega}{\omega_r}-\frac{\omega_r}{\omega}\right)} \qquad 1b)$$

for broad band impedance the resonance frequency results to be $\omega_r=\omega_c$ and three cases may be distinguished:

$\omega << \omega_c$ $$\frac{Z_{BB}}{P}=-j\frac{R_s\omega_0}{Q\omega_c} \qquad 1b_1)$$

$\omega = \omega_c$ $$\frac{Z_{BB}}{P}=R_s\frac{\omega_0}{\omega_c} \qquad 1b_2)$$

$\omega >> \omega_c$ $$\frac{Z_{BB}}{P}=j\frac{R_s\omega_0\omega_c}{Q\omega^2} \qquad 1b_3)$$

D) $$\frac{Z_{sc}}{P}=j\frac{Z_0 g}{2\beta\gamma^2} \qquad 1d)$$

---

*perturbing wave has the form exp[jK(z-vt)]

The impedance contribution from parasitic high *Q* resonators is not negligible [LAC2, CHA1, LED1]. Actually, shunt impedances of *MΩ* and *Q*-values up to several tens of thousands are reached. Even for non relativistic speed, such an impedance at resonance is very high. It is not possible to get a small momentum spread and the growth rate of instability is very high. As a result, accelerating cavities should be "shielded" or dismounted, when the storage ring is operated in the Crystalline working mode with coasting beams.

The calculated coupling impedances, for the different cases are reported in *Table 3.4*.

Table 3.4 - Coupling impedances (ohm).

Ions	Resistive.Wall	Space charge: g max.	Space Charge:g min
Mg	9,99E-03	8,43E+04	4,16E+04
Li	9,99E-03	8,43E+04	4,16E+04
Au	1,83E-02	2,25E+04	1,24E+04
Mg	1,33E-02	4,72E+04	2,33E+04
Li	2,42E-02	1,35E+04	6,68E+03
Au	3,08E-02	7,21E+03	3,56E+03

The estimation of impedance contribution of bellows is done at cut-off frequency and in the low frequency range [BRI1]. According to *Ref.* [KEI1] it is possible to consider each convolution as a small resonant cavity.

Calculation are performed by using ZOVERN code [RUG1]; a total of *20* bellows, having each one *15* identical convolutions *12 mm* high and *20 mm* wide, are considered. The results of calculations gives:

$$Z_{bell}/P=-j7\ \Omega \qquad \omega \ll \omega_c$$

$$Z_{bell}/P=3770\ \Omega \qquad \omega=\omega_c$$

The impedance at cut-off is not negligible. Assuming non identical convolutions, there is not a single sharp resonance line but a distribution of resonating frequencies. Furthermore, if the frequencies are randomly distributed with a spread equal to $\pm 10\%$, then, at resonance, it results:

$$Z_{bell}/P = 4.46\ \Omega \qquad \omega = \omega_c$$

This value of impedance has to be multiplied by the damping factor $f(\kappa) = 1.7 x 10^{-6}$ calculated before, and the total impedance associated to the bellows results negligible.

The ZOVERN program calculates strip line beam-position monitor impedance too. Here *8* B.P.M., *15 cm* long with *4* electric plate each one, are considered. Their termination impedances are assumed to be matched to the characteristic impedance of *50 Ω*. Their contribution to the impedance is:

$$Z_{bpm}/P = -j0.02\ \Omega$$

Transverse impedance

The transverse impedance is given by [LAC2]:

A) $$Z_{RW} = (1-j)\frac{RZ_0}{b^3}\delta_0\frac{1}{\sqrt{P}} \qquad 2a)$$

B, C) $\omega \ll \omega_c$ $$Z_{BB} = -j\frac{2c}{b^2}\frac{R_s}{Q}\frac{1}{\omega_c} \qquad 2b_1)$$

$\omega = \omega_c$ $$Z_{BB} = \frac{2c}{b^2}\frac{R_s}{\omega_c} \qquad 2b_2)$$

$\omega \gg \omega_c$ $$Z_{BB} = j\frac{2c}{b^2}\frac{R_s}{Q}\frac{\omega_c}{\omega} \qquad 2b_3)$$

D) $$Z_{sc} = j\frac{RZ_0}{\beta^2\gamma^2}\left(\frac{1}{a^2} - \frac{1}{b^2}\right) \qquad 3d)$$

The calculated transverse impedances are shown in *Table 3.5.*

Table 3.5 - Transverse impedances (ohm/m).

Ions	Space Charge	Space charge	Res. wall
	a min	a max	
Mg	4,58E+14	5,07E+11	3,88E+04
Li	4,58E+14	5,07E+11	3,88E+04
Au	1,02E+13	4,52E+10	2,14E+04
Mg	1,44E+14	1,59E+11	2,91E+04
Li	1,22E+13	1,35E+10	1,58E+04
Au	9,30E+11	4,12E+09	1,20E+04

3.1.2 Longitudinal Beam Stability

The Keil-Schnell criterion gives the minimum momentum spread required for ion beam stability at given coupling impedance and ion current. It reads:

$$\left(\frac{\Delta p}{p}\right)^2_{FWHM} \geq \frac{qI}{A|\eta|\left(\frac{m_0c^2}{e}\right)\beta^2\gamma}\left|\frac{Z_L}{P}\right| \qquad 4)$$

Table 3.6 shows the momentum spreads calculated for different beam intensities, beam radii and kind of ions.

Notice that *Eq.4* has been obtained for a gaussian beam distribution. Actual beam distribution is not well defined and, if below transition, any incoherent processes make the distribution edges smoother allowing Landau damping.

Table 3.6 - Longitudinal stability limit. *Δp/p* should be greater than the calculated numbers. *Max.* and *min. Δp/p* correspond to max. and min. space charge impedance, since RW one is negligible.

Ions	Δp/p max	Δp/p min	Δp/p max	Δp/p min
	N= 1E7	N= 1E7	N=1E5	N=1E5
Mg	3,60E-05	2,53E-05	3,60E-06	2,53E-06
Li	6,66E-05	4,68E-05	6,66E-06	4,68E-06
Au	1,82E-04	1,35E-04	1,82E-05	1,35E-05
Mg	2,02E-05	1,42E-05	2,02E-06	1,42E-06
Li	1,10E-05	7,76E-06	1,10E-06	7,76E-07
Au	6,09E-05	4,28E-05	6,09E-06	4,28E-06

3.1.3 Transverse Beam Stability

The transverse stability criterion is related to the Landau damping as the longitudinal one. The source of the frequency spread are transverse non-linearities and chromaticity. For the first case, the stability criterion reads:

$$\Delta\omega_{NL} = \Delta Q_L \omega_0 > \frac{qIc}{\pi A Q_x \left(\frac{m_0 c^2}{e}\right)\gamma} \left|Z_T(P)\right| \qquad 5a)$$

or in other words:

$$\frac{\Delta Q_L}{\Delta Q_{sc}} > 4 \qquad 5b)$$

where ΔQ_L is the incoherent tune spread due to amplitude spread, ΔQ_{SC} is the space-charge (Laslett) tune shift, and Q_x is the horizontal tune.

From *Ref.* [HOF1] we get that equations *5a,b)* are never fulfilled for every kind of ions distribution densities. A tune shift of this magnitude could be accomplished with the use of octupole magnets although one have to take into account high order resonances introduced by the octupole itself.

The main source for Landau damping is the momentum spread. Stability condition is [LAC2]:

$$\Delta\omega_{FWHM} > \frac{qIc}{4AQ_x\left(\frac{m_0c^2}{e}\right)\gamma}\left|Z_T(P)\right| \qquad 6a)$$

which impose the condition that:

$$P > \frac{\left(Q_x\omega_0 - \omega_\xi\right)}{\omega_0} + \frac{1}{\omega_0|\eta|\left(\frac{\Delta p}{p}\right)_{FWHM}} \frac{qIc}{4AQ_x\left(\frac{m_0c^2}{e}\right)\gamma}\left|Z_T(P)\right| \qquad 6b)$$

where $\omega_\xi = Q_x\omega_0\frac{\xi}{\eta}$ and $\Delta\omega_{FWHM} = |\eta|\left(\frac{\Delta p}{p}\right)_{FWHM}\left[(P - Q_x)\omega_0 + \omega_\xi\right]$.

In *Table 3.7* are shown the minimum stable azimutal harmonic and the tune spread needed for stability.

Table 3.7 - Transverse stability conditions. *Min.* and *max.* values correspond to min. and max. space charge impedance. RW impedance is negligible.

Ions	P	P	P	P	ΔQ_L	ΔQ_L
	N = 1E5	N = 1E5	N = 1E7	N = 1E7	N = 1E7	N = 1E7
	min.	max.	min.	max.		
Mg	5	1241	13	12374	2,693E-01	2,981E-04
Li	6	2294	22	22908	9,233E-01	1,022E-03
Au	4	36	5	329	3,731E-02	1,652E-04
Mg	4	698	9	6947	8,451E-02	9,356E-05
Li	4	390	7	3861	2,456E-02	2,719E-05
Au	4	15	4	112	3,397E-03	1,527E-05

3.2 Growth Rates and Cooling Process

The limits for stability conditions can be overcome by means of the cooling process. According to *Ref.* [COS1], cooling acts enlarging the stability diagram, and if the condition

$$\tau_{inst} \geq 2\tau_{cool} \qquad 7)$$

is verified, then both longitudinal and transverse instabilities can be avoided.

The growth rate of instability for the longitudinal case is given by [COS1]:

$$\tau_L^{-1} = P\omega_0 \frac{qI|\eta|}{2\pi\left(\frac{m_0c^2}{e}\right)\beta^2\gamma} \frac{\mathrm{Re}\left(\frac{Z_L}{P}\right)}{2\left|\mathrm{Im}\left(\frac{Z_L}{P}\right)\right|^{0.5}} \qquad 8)$$

In the same way, for the transverse case we have [COS2]:

$$\tau_T^{-1} = \frac{qIc}{4\pi AQ_x\left(\frac{m_0c^2}{e}\right)\gamma}\mathrm{Re}\left[Z_T(P-Q_x)\omega_0\right] \qquad 9)$$

Observing that such relations are obtained for the case of a beam without momentum spread and well below the threshold value given by Landau damping. However this is the case of a cooled beam, so previous assumptions are valid. The calculated growth times are shown in *Table 3.8* and *Table 3.9.*

The estimations show that longitudinal and transverse instabilities can be damped by cooling process. In fact the equation *7)* is easily fulfilled for both cases since the calculated growth time of instabilities are never less than cooling time available from electron or laser cooling [PET1, MAD1].

For the transverse case, the coherent motion for lower mode number can be damped by a feed- back system [LAC2].

Table 3.8 - Growth time for longitudinal instability multiplied by azimutal harmonic. *Max.* and *min.* correspond to max. and min. space charge impedance.

Ions	N= 1 E5	N= 1 E5	N= 1 E7	N= 1 E7
	τ (s) max	τ (s) min	τ (s) max	τ (s) min
Mg	2,18E+06	1,53E+06	2,18E+05	1,53E+05
Li	1,18E+06	8,26E+05	1,18E+05	8,26E+04
Au	1,90E+04	1,41E+04	1,90E+03	1,41E+03
Mg	9,15E+05	6,43E+05	9,15E+04	6,43E+04
Li	8,12E+04	5,70E+04	8,12E+03	5,70E+03
Au	3,87E+03	2,72E+03	3,87E+02	2,72E+02

Table 3.9 - Growth time for transverse instability.

Ion	τ (s) N = 1E+05	τ (s) N = 1E+07
Mg	9,29E+06	9,29E+04
Li	2,41E+06	2,41E+04
Au	1,43E+04	1,43E+02
Mg	6,97E+06	6,97E+04
Li	9,97E+05	9,97E+03
Au	8,46E+03	8,46E+01

3.3 Electron Beam Impedance and Growth Rate

The estimation of electron cooler beam impedance is required because some ions, like Gold in our case, can be cooled only by electron cooling. It is according to reference [BUR2],, possible to get the real part of longitudinal and transverse electron beam impedances from the following equations:

$$|\mathrm{Re}\, Z_L| \approx 0.1 Z_0 \frac{\omega_e t_f}{\beta} \qquad 10)$$

$$|\mathrm{Re}\, Z_T| = \frac{Z_0 \omega_e t_f}{4\beta a} S_P \qquad 11)$$

where ω_e is electron plasma frequency, t_f is time of flight of ions through the cooler, S is a sum factor over m modes.

The calculated real part of the electron cooler impedance is displayed in *Table 3.10*; while the growth times of longitudinal and transverse instabilities in the cooler are shown in *Table 3.11* and *Table 3.12*.

The growth times of instabilities caused by electron beam impedance are several orders of magnitude greater than growth time due to RW or space charge impedance. Especially for the longitudinal instability, very short cooling times are required for high charge state ions.

Table 3.10 - Real part of the electron cooler impedance. Electron density=3×10^7 cm^{-3}, cooler length is *1 m*.

Ions	Longitudinal (ohm)	Transverse a max (ohm/m)	Transverse a min (ohm/m)
Mg	4,18E+04	3,49E+07	1,05E+09
Li	4,18E+04	3,49E+07	1,05E+09
Au	3,77E+03	3,14E+06	4,71E+07
Mg	1,31E+04	1,10E+07	3,29E+08
Li	1,15E+03	9,59E+05	2,88E+07
Au	3,77E+02	3,15E+05	9,44E+06

Table 3.11 - Growth times for longitudinal instability. *Max.* and *min.* are related to max. and min. space charge impedance.

Ions	Pτ (s) max	Pτ (s) min	Pτ (s) max	Pτ (s) min
	N= 1 E5	N= 1 E5	N= 1 E7	N= 1 E7
Mg	5,04E+00	3,54E+00	5,04E-01	3,54E-01
Li	2,72E+00	1,91E+00	2,72E-01	1,91E-01
Au	8,98E-01	6,66E-01	8,98E-02	6,66E-02
Mg	9,00E+00	6,32E+00	9,00E-01	6,32E-01
Li	1,67E+01	1,17E+01	1,67E+00	1,17E+00
Au	3,15E+00	2,21E+00	3,15E-01	2,21E-01

Table 3.12 - Growth times for transverse instability.

Ions	τ (s) a max	τ (s) a min	τ (s) a max	τ (s) a min
	N= 1E5	N= 1E7	N= 1E5	N= 1E7
Mg	2,67E+04	2,67E+02	8,90E+02	8,90E+00
Li	6,92E+03	2,32E+02	2,31E+02	2,31E+00
Au	2,51E+02	2,51E+00	1,67E+01	1,67E-01
Mg	1,24E+04	4,77E+02	1,59E+03	1,59E+01
Li	4,24E+04	4,24E+02	5,46E+03	1,41E+01
Au	8,31E+02	8,31E+00	2,77E+01	2,77E-01

3.4 Secondary Electron Impedance

Because the ionization of the residual gas by the circulating ion beam, secondary electrons are stored untill a certain level in its potential well. This electron media may produce perturbations on the ion beam which give rise to instabilities. The interaction process [CHI1, KOS1, LAS1, ALV1] can also be described in terms of a wake potential and an impedance of the electron media. The dipole oscillations are the most dangerous and here are discussed in detail.

The transverse displacement of the center of mass of electrons satisfy the following equation:

$$\ddot{y}_e + \omega_{ei}^2 (y_e - y_i) + \lambda_{ei} \dot{y}_e = 0$$

where $\omega_{ei} = \sqrt{2\pi n_i Z_i e^2 / m_e}$ is the frequency of the dipole oscillations of electrons in the ion field, $\lambda_{ei} \cong \Delta\omega_{ei}$ is the decrement of the coherent oscillations due to the frequency dispersion $\Delta\omega_{ei}$ in the non-linear potential well. As usual, n_i, Z_i are the density and the charge state of ions, and m_e is the electron mass.

The electron reaction in the point of ions dipole moment $q_i y_i$ is determined by the following equation:

$$y_e(t) = \frac{2eq_i y_i}{m_e v \omega_{ei} a_i^2} \sin(\omega_{ei} t) \exp(-\lambda_{ei})$$

where a_i is the radius of the ion beam. Representing the force $F = 2\pi n_e e q_t y_e$ acting on a test particle of charge q_t as $F = q_t q_i y_i W(t) / L$, the wake potential $W(t)$ per unit length L is given by [CHA1]:

$$\frac{W(t)}{L} = \frac{2\sigma\omega_{ei}}{v a_i^2} \sin(\omega_{ei} t) \exp(-\lambda_{ei})$$

with $\sigma = n_e / (Z_i n_i)$ denoting the degree of the space charge compensation (n_e is the electron density). From here, the transverse impedance

$$Z_\perp(\omega) = -j\int_0^\infty W(t)\exp(j\omega t)dt$$

can be written as:

$$\frac{Z_\perp(\omega)}{L} = \frac{2\sigma}{va_i^2}\frac{\omega_{ei}}{\omega}\frac{Q}{1+jQ\left(\frac{\omega_{ei}}{\omega}-\frac{\omega}{\omega_{ei}}\right)}$$

where $Q = \frac{\omega_{ei}}{2\lambda_{ei}}$ is the quality factor of the electron oscillations.

The growth rate of the instability [CHA1] induced by this impedance is given by:

$$\Lambda_\perp = \frac{N_i Z_i^2 r_p c^2}{4\pi\gamma A_i Q_{x,y}}\frac{\operatorname{Re} Z_\perp}{C}$$

Here, A_i is the ion mass, r_p is the classical proton radius, $Q_{x,y}$ is the betatron tune and C is the ring circumference. The maximum growth rate achieved when $Q|\omega - \omega_{ei}| / \omega_{ei} < 1$ can be written in the following compact way:

$$\Lambda_\perp = Q\delta\omega_{be}$$

where

$$\delta\omega_{be} = \frac{\pi n_e Z_i r_p c^2}{A_i\omega_b}\frac{L}{C} = \delta\omega_{bi}\sigma\frac{L}{C}$$

is the shift of the betatron frequency on the electron space charge. $\delta\omega_{bi}$ denotes the shift on the space charge of ions. In presence of a hot ion beam, the dispersion of the revolution frequency $\Delta\omega_0$ is large enough, i.e.:

$$\omega_{ei}\frac{\Delta\omega_0}{\omega_0} > \Lambda_\perp$$

and the instability is Landau damped [KOS1]. For cooled ions the stability can be achieved because the decrement $\lambda_c \cong \tau_c^{-1}$ introduced by the cooling, where τ_c is the cooling time. The stability condition reads:

$$Q\delta\omega_{be} < \lambda_c .$$

Because the non-linearity of the potential well of the ion beam, the electron quality factor is usually not very large: $Q = 2 - 5$. Taking, for instance, $\tau_c = 1ms$, $Q = 3$, and $\omega_0 = 3x10^6$, the region of stability is: $\delta\omega_{be} / \omega_0 < 10^{-4}$. To be below such low threshold values a careful secondary electron clearing is necessary.

References

[ALV1] R. Alves Pires et al.; Proc. of Particle Accelerators Conference, Chicago (1989) 800.

[BRI1] R.Briggs and V.Neil; Plasma Physics 8, 255 (1966).

[BUR1] A. Burov; Wall Impedance for Low and Moderate Beam Energies, CSR Internal note (1995).

[BUR2] A. Burov; "Electron Cooler Impedances", CSR Internal note (1995).

[CHA1] A.W. Chao; Physics of Collective Beam Instabilities in High Energy Accelerators, Wiley & sons, Inc., New York 1993.

[CHI1] B.V. Chirikov; Atomnaja Energija, 19 (1965) 239.

[COS1] S. Cosher and I. Hofman; Part. Acc. 34 (1990) 189.

[COS2] S. Cosher; PhD Thesis, "Effets collectifs d'un faisceau refroidi d'ions lourds dans un anneau de stockage" GSI (1989).

[HOF1] I. Hofmann and S. Coscher, GSI Scientific Report (1987), 388.

[KEI1] E. Keil and B. Zotter; Part. Acc., 3 (1972) 11.

[KOS1] D.G. Koshkarev et al.; Part. Acc. 3 (1972) 1.

[LAC1] J.L. Laclare, Proc. CERN Accelerator School, CERN 85-19, (1985) 377.

[LAC2] J.L. Laclare; Proceeding of Fifth General Accelerator Physics Course, Jyvaskyla (1992), pag.349 and 385.

[LAS1] L.J. Laslett et al.; Nucl. Instrum. Meth. 121 (1974) 517.

[LED1] J. Le Duff; Proceeding of Fifth General Accelerator Physics Course, Jyvaskyla (1992), pag 259.

[MAD1] M. Madert; Diplomarbait (1995) MPI Heidelberg.

[PET1] W. Petrich et al., Phys. Rev. A48 (1993) 2127.

[RUG1] A.G. Ruggiero; Informal Reports: BNL-27756 (August 1979) and KEK 80-16 (March 1981).

[STR1] J. Struckmeier; PARMT Code, GSI-ESR-87-03 (1987).

[TEC1] L. Tecchio et al.; CRYSTAL: A Storage Ring for Crystalline Beams (Feasibility Study); LNL-INFN (REP) 80/94 (1994).

4

Diagnostics of Ordered Beams

4.1 Beam Diagnostics and Instrumentation

The beam diagnostics is, perhaps, the most fundamental, and challenging, sub-system of the project. Two different goals have to be fulfilled by the diagnostic system. The first goal is to provide conventional readout of the beam parameters when the beam is still in its hot (conventional) phase. The second, and more important, goal is to obtain a clear signature of the beam ordering.

In the Feasibility Study of the CRYSTAL Storage Ring [TEC1], different techniques have been described to detect both conventional and ordered ion beams.

Direct imaging of ordered structures or indirect techniques, like the stroboscopic laser diagnostics seems to be most promising. Here, a particular attention will be devoted to non-conventional techniques now under study and development for the ordering detection. Namely the Direct or Indirect Deflection able to convert longitudinal separation in transverse space separation and the stroboscopic laser diagnostics.

The direct imaging of an ordered beams is one of the key diagnostics for the CSR proposal. At first approach, the most simple configuration, the string, is considered. With the foreseen ion velocity, in the order of some percent of β, and the ion separation of the order of $100\ \mu m$, the time separation of two subsequent ions turns out to be some tenths of picoseconds. Therefore devices acting in the picosecond range have to be developed.

4.2 Direct Beam Deflection

This method of diagnostics is based on the fast deflection of the Crystalline Beams properly ejected from the CSR. The fast deflection system is designed for a high speed scanning of the Crystalline Beam in the transverse direction in order to transform its longitudinal space structure to the transverse one to find out this structure. The main elements of the diagnostic system are a fast kicker and a detector of high space resolution sensitive enough to detect each single ion. The kicker and the detector are separated by a drift space. The kicker provides a fast beam scanning in the vertical direction. As a result, the beam track moves with a high velocity over the receiving surface of the detector, the space structure of the track repeating the longitudinal structure of the beam. The drift space length is chosen such that the distance between the tracks of neighboring ions safely exceeds the detector resolution over its coordinate. *Fig. 4.1* shows a sketch of the diagnostic device, while its main parameters are reported in *Table 4.1*

The kicker has a form of a *20 cm* long segment strip line, it has a wave resistance of *50 Ohm* and is operated in the regime of the counter-traveling wave. A grounded plate both at the input and the output of the kicker has openings for the beam to pass. The kicker aperture is $8x3\ mm^2$. A high voltage pulse is fed to the kicker input by a coaxial cable. Since the ions have a positive charge and the pulse polarity is also positive, the beam is deviated upwards.

The generator of high voltage nanosecond pulses (*40 kV*) for the kicker power supply consists of an energy storage capacitor, a spark gap switch with a triggering circuit and a charge circuit. The high voltage pulse, with short rise time ($< 3\ ns$), flat top (*20 ns*) and exponential decay (*80 ns*), is formed at the expense of the discharge of the capacity to the input of the coaxial cable, matched at the end through the spark gap switch. The rise time is determined by the time of commutation of the switch and the quality of the wide-band matching of the generator elements.

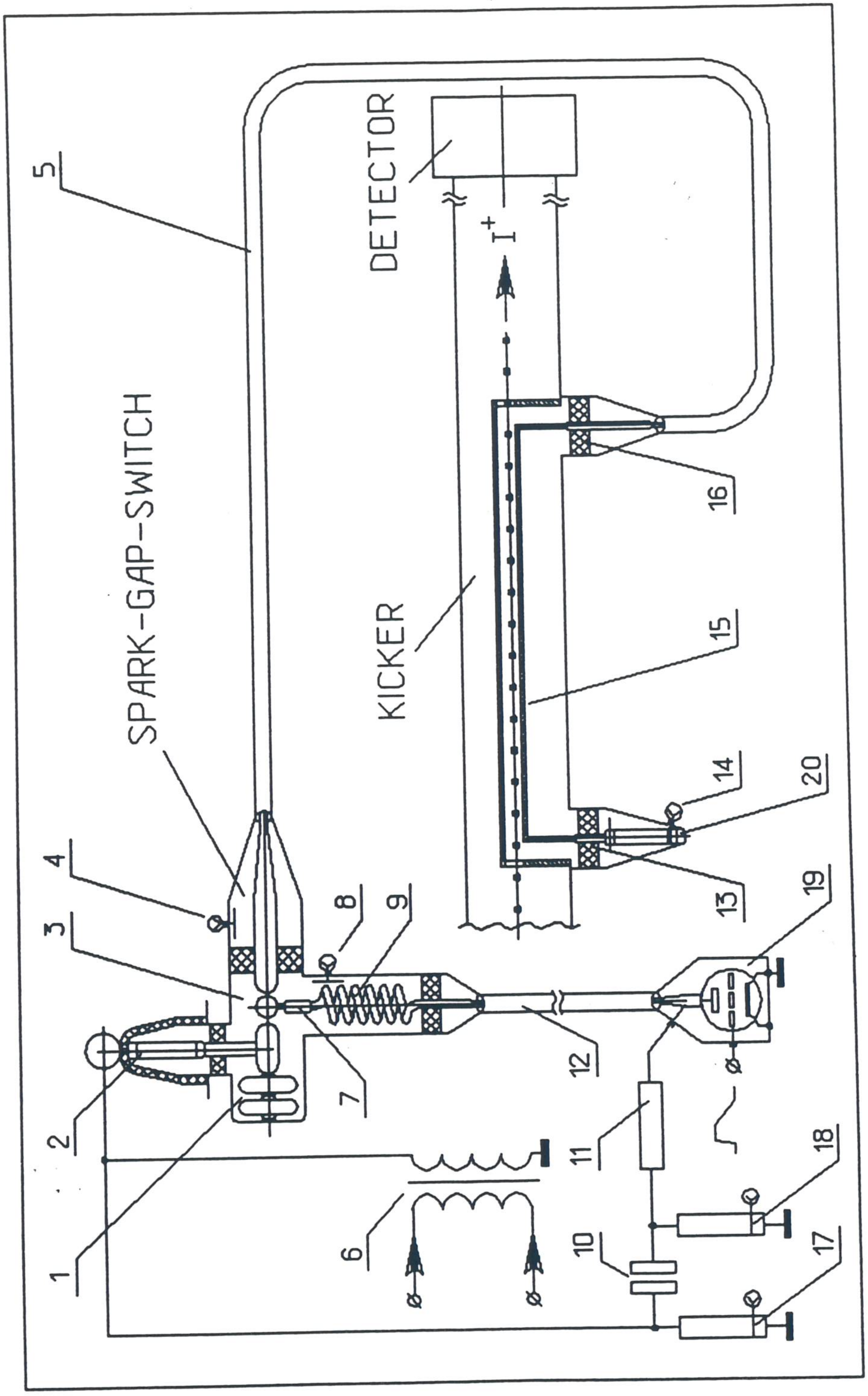

Fig. 4.1 - A sketch of the fast deflection diagnostic device.

Table 4.1 - Main parameters for the fast deflecting system.

Kicker:	
length	0.2 m
aperture	8x3 mm^2
wave resistance	50 Ohm
drift space	3 m
field in the gap	130 kV/cm
Pulse generator:	
pulse amplitude	40 kV
rise time	< 3 ns
flat top duration	20 ns
fall time constant	80 ns
jitters time	< 3 ns
wave resistance	50 Ohm
repetition frequency	2 Hz
Detector:	
space resolution	10 μm
n. of particle per sample	> 100
sensitive region	> 5 mm

The detector for observing the Crystalline structure of the beam has a space resolution of about *10 μm* and a high enough sensitivity for a reliable detection of a single ion. A CCD-matrix detector associated to a Micro Channel Plate (MCP) gives the required performances.

Typically, for a string of $^9Be^+$ with $\beta = 0.07$ the expected maximum angle deflection is *0.063* and the distance between the deflected particles on the detector is the same as in the string itself (*100 μm*), thus the transformation coefficient is close to unity. Since the transformation coefficient is inversely proportional to β^2, it can be increased considerably by decreasing the ion energy. This will improve the performances of the detector system.

4.3 Indirect Beam Deflection

The basic idea of the method is the same as for the classical streak camera, where usually a bunch of photons is converted into electrons by a photo-cathode; then the electrons, which maintain the same time structure of the parent photons, are deflected in order to convert the longitudinal time separation in transverse space separation detected over a scintillator and CCD camera. Time resolution of the order of some picoseconds can be reached in normal operation.

In principle, one can maintain the same classical configuration of the streak camera and use a scintillator to produce the bunch of time correlated photons to be converted by the photocathode. Unfortunately, the decay time of the faster scintillator (BaF, $800\ ps$ decay time) is too high in comparison with the ion separation foreseen for ordered ions ($10 \div 50\ ps$) and therefore it does not allow the use of the classical streak camera.

To employ the same method with ordered ions a different conversion mechanism have to be used. The faster and most efficient conversion mechanism is based on the secondary emission effect from a thin foil of carbon, eventually enriched with LiF to enhance the effect.

In order to define an efficient method of detection, investigations have been focused on two separated subject: *i)* the production of secondary electrons, correlated in time with incident ions; *ii)* the Fast Transverse Deflecting device (Open Streak Camera) with Discharge or RF method.

4.3.1 Secondary Emission Electrons

The secondary emission effect of electrons from a thin foil hitted by ions has been extensively studied from the experimental point of view in a large variety of conditions [CLE1] and, although the refined details of the mechanism are still to be well understood, nevertheless the main experimental parameters of the effect can be summarized in *Table 4.2* and in the pictures of *Fig. 4.2* and *Fig. 4.3*.

Table 4.2 - Average number (4π solid angle) of secondary emission electrons produced on one and two parallel carbon foils, for different projectiles [CLE1].

Ion	E [MeV]	1 Foil	2 Foils
^{4}He	3.5	8.1	16.4
	6.1	5.5	11.2
	8.8	3.9	8.3
^{16}O	1.8	43	86
	2.8	50	104
	5.7	55	114
	9.6	53	113
	19.6	45	91
	29.5	40	83
^{32}S	7.5	81	187
	14.5	95	220
	22.5	97	225
	29.6	96	217
	39.3	-	208
	43.3	91	-
^{127}I	10.2	83	-
	20.1	124	-
	33.8	163	-
Light fission fragments (Z_{av}=43)	73	192	520
Heavy fission fragments (Z_{av}=55)	46	170	451

When an ion with kinetic energy in the range of some tenths of *MeV* passes through a thin carbon foil many secondary emission electrons are produced with an energy spectrum which ranges from few *eV* to some *keV*. The main production process is called Cascading Ionization where the electrons extracted from the higher bands of the lattice

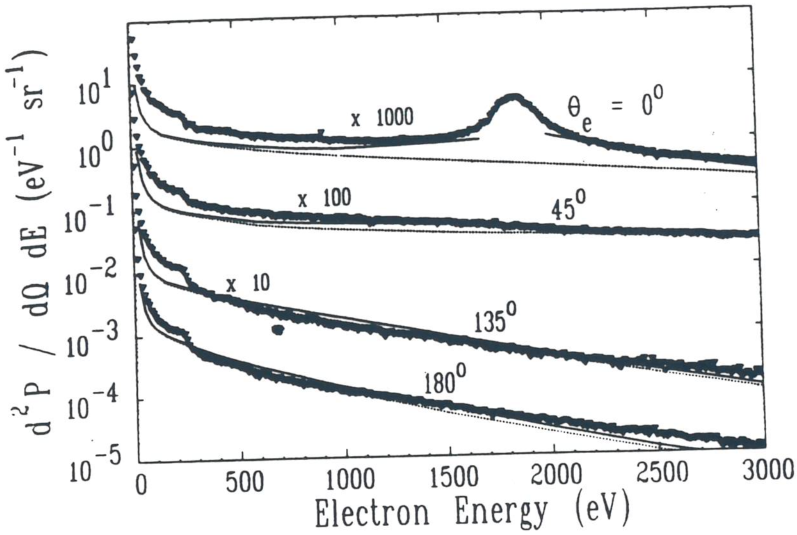

Fig. 4.2 - Energy spectra of secondary emission electrons from a thin carbon foil [GAI1].

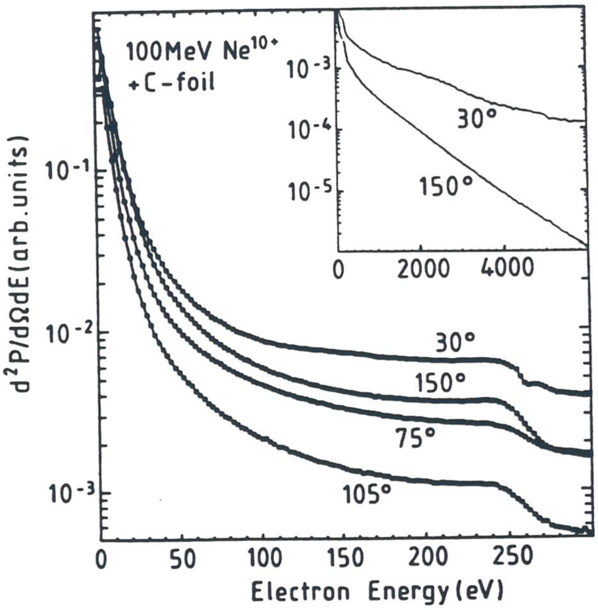

Fig. 4.3 - Energy spectra of secondary emission electrons from a thin carbon foil, Auger component [KRO1].

participate to the subsequent extraction of further electrons. The only electrons which are able to reach the foil surface are those extracted in the last 300 Å (about 5 mg/cm^2 for the Carbon).

Two further effects have been identified in the energy spectra of the emitted electrons. The first one is the group of electrons which are produced with the same velocity (as a vector, absolute value and direction) of the impinging ion (see *Fig. 4.2,* curve with $q_e=0$). They are called "Convoy Electrons" and seems to be produced and extracted by the wake field of the ion itself or eventually they are remnants of "Rydberg ions". The second relevant effect is the peak due to the "Auger Effect", corresponding to the low energy electrons.

The fundamental request for the conversion device is the time correlation of the extracted electrons with the impinging ion. Different effects contribute to the possible lost of time correlation, namely:

a) the angle of emission;
b) the kinetic energies of the extracted electrons;
c) the transit time of the impinging ion across the last layer of the carbon foil.

The transit time across the last layers ($5\ \mu g/cm^2$) of the foil has been evaluated with different energies of the impinging ion and it results to be of the order of few femtoseconds and then can be neglected.

To increase the efficiency of the device it is worthwhile to collect all the emitted electrons up to at least $85°$ emission angle. This can give a not negligible contribution to the lost of time correlation of the order of some tenths of picoseconds.

To overcome possible contributions to the poor correlation due to both angle of emission or the energy spectrum, an extraction grid with an acceleration voltage of at least $20\ kV$ have to be placed in front of the foil. This allows the collection of almost all the electrons emitted in the forward angle ($2p$) and reduces the time spread between the mono-energetic electrons emitted at 0° and the $85°$ to less than $5\ ps$. Note that with the acceleration grids at *20 kV* the electrons emitted at *85°* emerge from the grid with an angle smaller than *1.8 °*.

The set-up of the conversion device is described in *Fig. 4.4* where the carbon foil is maintained at a negative potential of *20 kV* while two grids, at earth potential, are symmetrically placed *5 mm* apart in order to reduce the stress on the foil due to the electric field. In the final set-up, the electrons, produced on the carbon foil and accelerated to *20 keV* by the grid, will be sent to an open streak tube or to an RF deflecting device as described below.

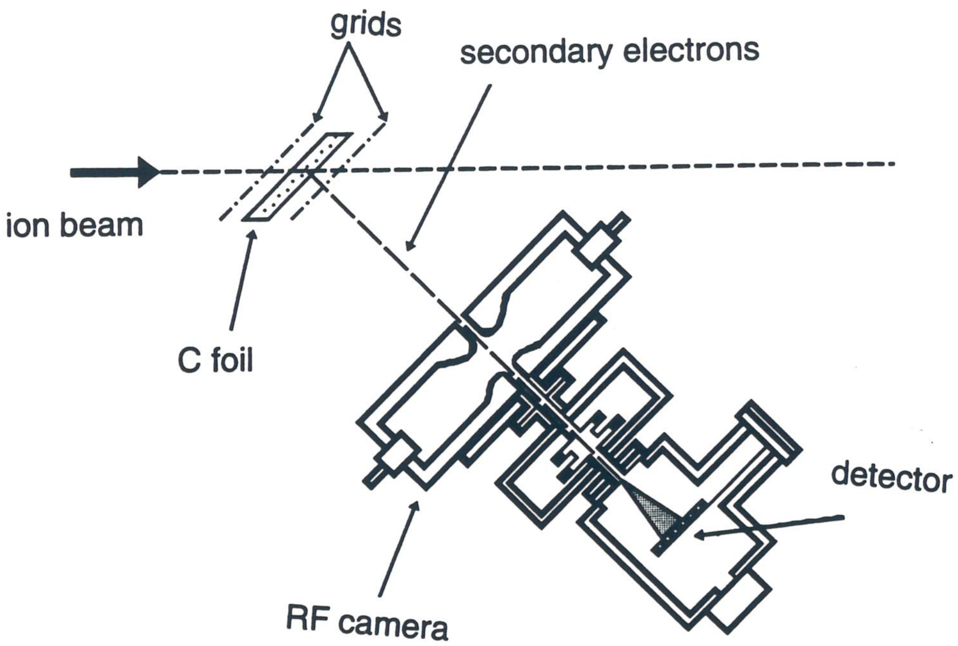

Fig. 4.4 - Schematic set-up for the conversion device based upon the secondary emission effect.

4.3.2 Techniques for Indirect Deflection

As anticipated above two different techniques can be used for the deflecting device. The first one is the classical one, nowadays available for commercial streak cameras, based on the deflection obtained with an electrical field linearly variable across two deflecting parallel plates. The time resolution limit of this technique is of the order of few picoseconds.

The second technique, already successfully tested [ALE1], is based on the deflection by a rotating RF magnetic field. In the RF deflection the electrons produced by the secondary emission process on the carbon foil is sent towards an RF cavity, where a TM_{110} configuration produces a rotating magnetic field which deflects the incoming electrons. Actually, the cavity is supplied by two equally powered RF inputs placed $90°$ apart in azimutal angle and phase shifted also by $90°$. The generated magnetic field rotates in a plane perpendicular to the incoming electron trajectory, with an angular velocity equal to the RF frequency of the cavity itself (*2.46 GHz*).

The deflection on the incoming electrons depends on the arrival time and, because of the rotating magnetic field, the longitudinal structure is converted into an angular distribution in the transverse plane. At a distance L from the RF cavity a MCP will be used to multiply the electrons and give enough power to create photons on a phosphor layer detected then by a CCD camera.

The radius of the circumference at a distance L from the cavity is given by the following relation:

$$R = (eHL)/(p\gamma wmc)$$

with H the module of the rotating magnetic field, γ the relativistic coefficient of the electrons, e and m the electron charge and mass, w the RF frequency of the cavity.

With a spatial resolution of about $50\ \mu m$ on the transverse plane at a distance of $L=30\ cm$, a magnetic field $H=30\ Gauss$, electrons of $60\ keV$ and an RF frequency of $2.46\ GHz$, the resolution of about *0.2 ps* can be reached. A schematic drawing of the RF device is shown in *Fig. 4.5*.

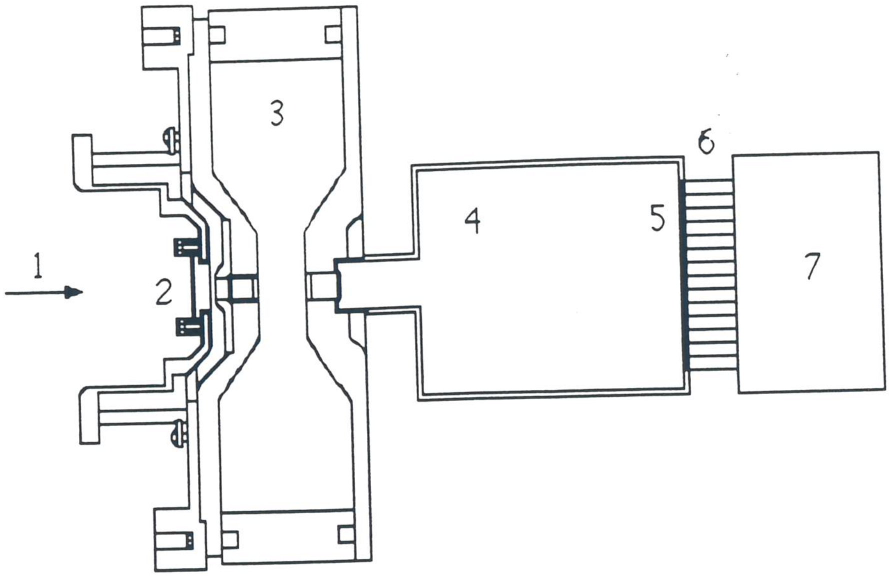

Fig. 4.5 - Schematic drawing of the RF deflecting camera; cylindrical symmetry around the beam axis. (1) ion beam, (2) carbon foil and acceleration grids, (3) RF-cavity, (4) drift space, (5) Phosphorescent screen, (6) Optical system, (7) CCD camera. A MCP electron multiplier or a position sensitive single particle detector may replace the CCD camera and the associated optics.

The advantages of the RF device in comparison with the discharge device (commercial streak camera) are essentially the following:

a) high time variation of the deflecting force based on a resonance field;

b) deflecting force proportional to the electron velocity (Lorentz force).

The first characteristic allows to obtain higher deflecting force with higher time variation with respect to the ones reachable with a discharge method with less technological challenge.

The use of the Lorentz force for the deflection allows the use of much more energetic electrons than in the classical streak cameras and then to overcome one of their resolution limit due to the space charge.

Actually, just because of the nature of the deflection in the classical streak cameras, due to the electric field, and to technological constraints on the maximum deflecting voltage, the electrons produced on the photocathode are accelerated only up to $20\ keV$ and the space charge forces are enough strong to introduce contributions to the final deflection and then to reduce the time resolution.

4.4 Stroboscopic Laser Diagnostic

Besides the diagnostic methods above discussed, a new fluorescence-based method is proposed to detect ordering in a one-dimensional ion beam.

The basic principles of this method and its application to a real storage ring will be presented.

A pulsed laser, resonant with the traveling ions, is split in two parts, which simultaneously cross the ion beam at right angle at two nearby positions along the storage ring (see *Fig. 4.6*). This laser-to-ion crossing area is followed by four photomultipliers which detect the photons emitted by the ions that have previously been excited by the laser beams. The signals recorded by the photomultipliers are analyzed when one laser beam is moved with respect to the other one. In the absence of ordering, no correlation in fluorescence signals should be recorded while changing the relative distance of the two laser beams. On the contrary, if a string were obtained as a result of cooling, a strong correlation between the signals should be observed. Suppose that one of the four photomultipliers detects the fluorescence of an ion excited by one of the laser beams.

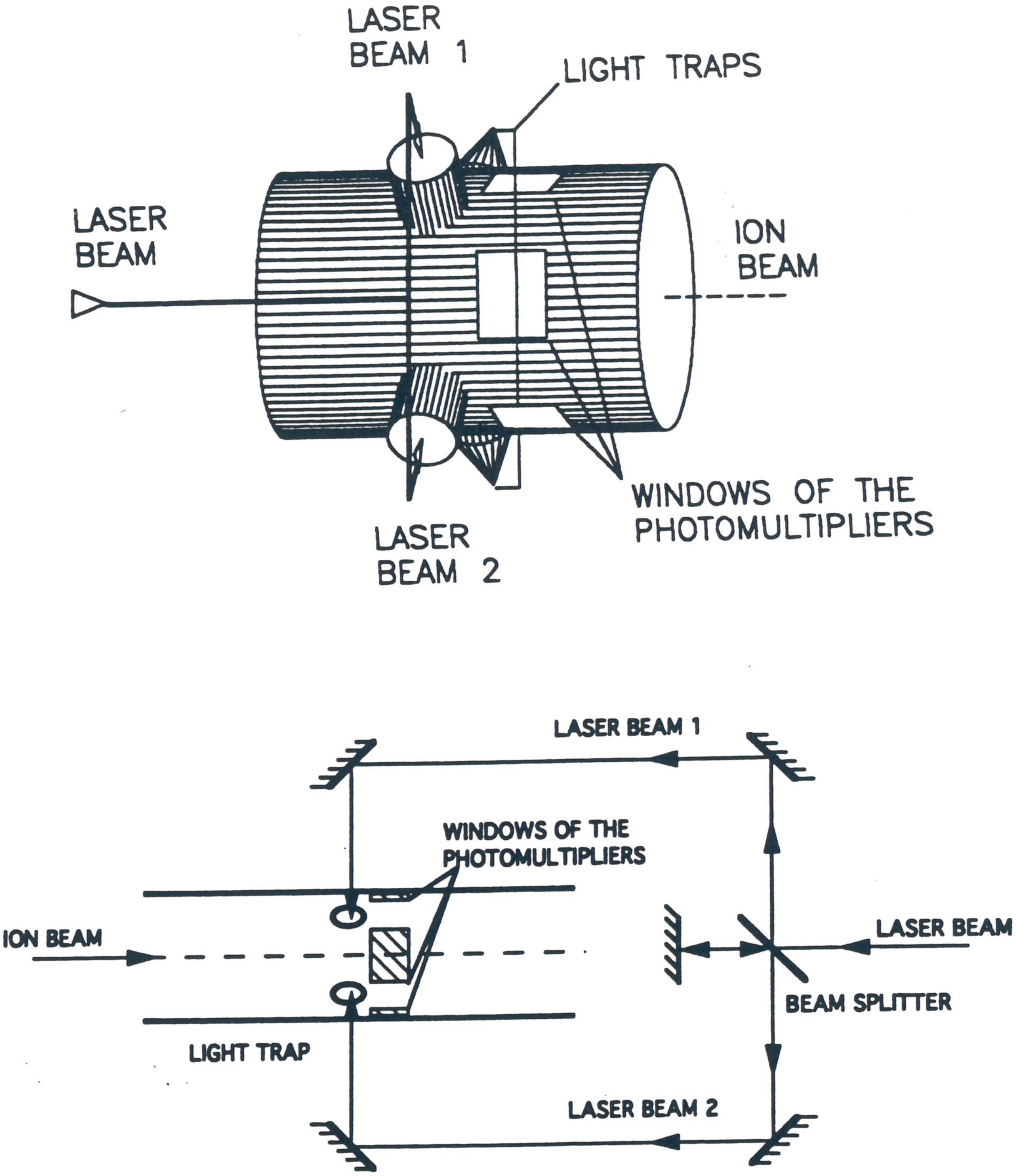

Fig. 4.6 - A sketch of the experimental apparatus: a) general view, b) side view.

If one of the other three photomultipliers detects a simultaneous fluorescence signal, it means that the other laser has interacted with another ion in the string, in turn indicating that the distance between the two ion-to-laser crossing points is an integer multiple of the string interparticle spacing. Then, by slightly moving the second laser beam, the correlation signal should vanish. A sort of periodical dependence on the distance between the laser beams should appear, whose contrast will mainly depend on the detection efficiency.

The diagnostics is conceived with the aim of detecting ordering within a string of ions in a storage ring. Typical values of the interparticle spacing for the string configuration lie between $s=10\text{-}100\ \mu m$; for the following we shall assume $s=50\ \mu m$. At non-zero temperature, ions are expected to oscillate both in the transverse and longitudinal directions (incoherent motion). Moreover, for a string longitudinal oscillations of equilibrium positions can also occur (coherent motion) through long-range waves. For this diagnostic system the distance between the two laser beams can be chosen to match interparticle spacing of the string. In this case, the effect of coherent motion is ineffective as the nearest-neighbor spacing is relatively uniform. The effect of long wavelength on interparticle oscillations is negligible for a relative distance of a few lattice steps. An analytical evaluation of this effect can be found in Ref. [LAN1]. Short wavelengths mostly affect the fluctuations in interparticle spacing, δs. Based on *Ref.* [LAN1], a rough estimate holds: $<\delta s^2>/s^2 r 1/\Gamma$, where Γ is the plasma parameter for the ion beam. When the ion beam is being cooled δs becomes even lower than s; as an example, at $\Gamma=100$, $\delta s=5\ \mu m$. If the distance between the laser beams were larger than one interparticle spacing, the correlation signal should become progressively weaker.

The configuration of the diagnostic device can also compensate for a possible influence of transverse oscillations. Since the laser beams cross the string perpendicularly and their spots are small enough that they do not overlap, the ions suffering transverse oscillations in the direction of the laser can always be resonant, irrespective of their coordinates along that axis. Ion oscillations in direction orthogonal to both the laser and the string could in principle move the target ion outside the laser beam spot. To avoid this effect, and the consequent less efficiency, the laser beam can be focused by a cylindrical lens. This optical element can be arranged to produce a focal segment orthogonal to the directions of both the laser and the string. In this way the locations where the laser beams impinge on the string are two thin regions; these can be as wide as several hundreds of microns in one dimension without overlap between them. Transverse oscillations of a very cold ion beam are expected to be lower than this value.

A single ion of the beam interacts with one of the laser beams for very short time, t_{int}. The probability of excitation to the upper level $P(t_{int})$ is:

$$P(t_{int}) = \sin^2(\omega_R t_{int}/2)$$

where ω_R is Rabi frequency for the transition under consideration, which is proportional to the square root of the laser intensity. Thus, a reasonable interaction probability requests a sufficiently high laser intensity to make up for the short interaction time. However, this is not a problem since pulsed laser are several times as intense as the saturation intensity and a good excitation probability $(\sim 1/2)$ can be achieved with existing lasers. Moreover the focusing lens increases the intensity of the laser beam at the interaction point.

4.4.1 Application to a Real Storage Ring.

We shall discuss a possible implementation of such diagnostic device with reference to the case of a $^{24}Mg^+$ string. In order to provide an example of a possible application, we shall refer to the ASTRID Storage Ring at Aarhus: its main parameters can be found in *Ref.* [HAN1]. With the above assumptions, the velocity of the ion beam is about $v=8.97x10^5$ m/s. The time duration of each laser pulse must be much shorter than the time, $T=s/v=56$ ps, taken by an ion to travel one interparticle spacing. On the other hand, the laser pulse must not be too short because this would lead to a very broad frequency pattern, in turn making more difficult the filtering between laser photons and fluorescence photons, as discussed below. A laser whose pulses are *2 ps* long meets these requirements. In the following we shall refer to a commercially available, frequency tripled $Ti{:}Al_2O_3$ pulsed laser (*50 MHz* repetition rate), with some *nJ/pulse*. This power is sufficiently high to regard the excitation probability of $^{24}Mg^+$ to be about *0.5* for the transition under consideration ($3s\ ^2S_{1/2}$ *to* $3p\ ^2P_{1/2}$). The laser frequency must be resonant with the ion's transition energy in its reference system ($\lambda=279.6$ *nm*). The laser beams need focusing to spot much smaller than the interparticle spacing (*50* μm). This can be done since it is experimentally possible to focus a laser beam within *5* μm (FWHM). The laser focusing systems need to be placed in the vacuum chamber and should be movable in order to avoid interference with the ion beam during normal operation of the storage ring. The decay region is viewed by four photomultipliers, located each behind its own window. The window length ($2L$) matches the decay length for the ion de-excitation. The four windows cover about *50%* of the azimuthal acceptance of the fluorescence photons. The distance d, between the upstream edge of photomultiplier acceptance and the interaction region between the ion and the laser beam should be as short as possible (see *Fig. 4.7*). We assume $d=10$ *mm*, $2L=20$ *mm*, a beam-pipe radius, $R=35$ *mm*, and the lifetime of the upper level, $\tau=3.5$ *ns*. The photomultipliers are single-photon detectors, which can be assumed to have a quantum efficiency of *23%* and a rate of background counts of about *100 counts/s*.

The signals from the four photomultipliers are discriminated (*20 ns* signal width) and the logical signals are ANDed two by two to form *6* combinations. These are then ORed; a positive logical level for the OR is an event in which the two ions, excited by the laser beams, have both emitted a photon.

Each photomultiplier must be equipped with a filter to intercept stray laser photons. Let θ be the angle between the direction of the ion beam and the direction of a photon emitted by an ion. Due to the finite duration of a laser pulse (*2 ps*), the frequency spectrum is of the order of *500 GHz*. Considering that the laser beams impinge on the string at right angle, the photons of the lasers are overlapped in frequency with those from natural fluorescence between the angles $\theta=85^o$ and $\theta=95^o$. Filters are designed in order to discard all photons impinging with an angle $\theta>70^o$. The geometrical acceptance of the system allows detection of photons only for $\theta>50^o$. This corresponds to a lower limit for the filter bandwidth of *0.25 nm*.

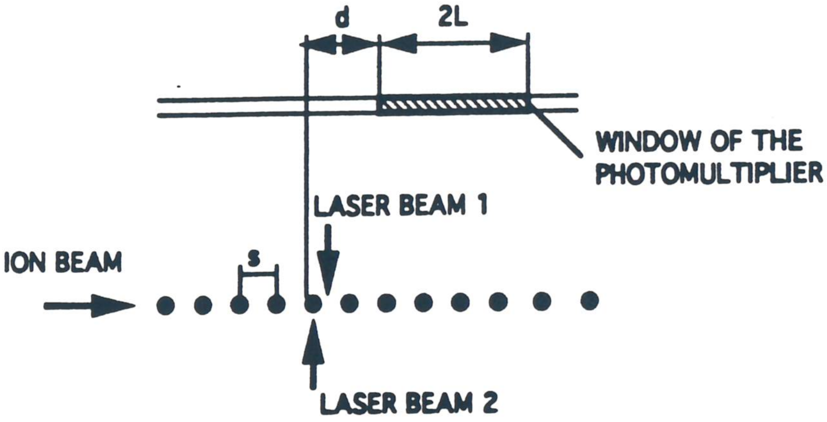

Fig. 4.7 - A sketch of the ion-laser interaction region.

The distance between the two laser beam spots can be varied by moving the optical set-up; this movement can be done with an accuracy better than the range of longitudinal oscillation for interparticle spacing.

As described above, by moving the second laser beam with respect to the first one and counting the coincidence events of the photomultipliers, one can assess if the distance between the two laser-to-ion crossing points is an integer multiple of the string's interparticle spacing. After having met this condition, by slightly moving the second laser, one would record only accidental coincidences; this is true since, if the first laser excites an ion, then the second laser beam can no longer be synchronous with any other ion in the string. Appearance of correlation in the signals with the same periodicity of the string would be firm indication of ordering in the beam.

The total probability that one of the four detectors sees the fluorescence of an ion excited by one of the lasers is about 9.3×10^{-4}. Considering a purely random jitter of the laser, a laser beam spot of $5\ \mu m$ and a typical interparticle spacing of $50\ \mu m$, the probability that a laser pulse crosses an ion in the beam can be roughly estimated as $1/10$.

Therefore, the probability that a simultaneous de-excitation will be recorded by the device is 10^{-6}. Considering a repetition rate of the laser of $5 \times 10^{7}\ Hz$, one expects a counting rate of approximately $50\ Hz$. When the distance of the laser-to-ion beam crossing points is not an integer multiple of the string's step, the rate of accidental coincidences is estimated to be $0.25\ Hz$. On the contrary, a non ordered ion beam would exhibit a coincidence rate of $10\ Hz$ independent of the relative positions of the laser beams.

In order to check these results, we have developed a Monte Carlo simulation. Ion oscillations around their equilibrium positions, the excitation process of an ion by the laser light, the spontaneous emission, the geometrical acceptance and efficiency of the detector (filters + photomultipliers) are taken into account. *Fig. 4.8* shows the counting rate of coincidences versus the position of the second laser. A strong correlation signal is achieved for the case of an ordered string.

The diagnostic method can be easily extended to higher ion velocity provided that the pulse duration of the laser be proportionally reduced. Commercially available lasers in the femtosecond domain could be used as stroboscopic diagnostics of ordering for beams with $\beta \sim 0.1$.

4.4.2 Ion Beam Perturbation

The proposed method of detection of fluorescence makes use of absorption and emission of a photon of the laser and its subsequent re-emission. As for any kind of diagnostics, this technique perturbs the system under consideration; here an

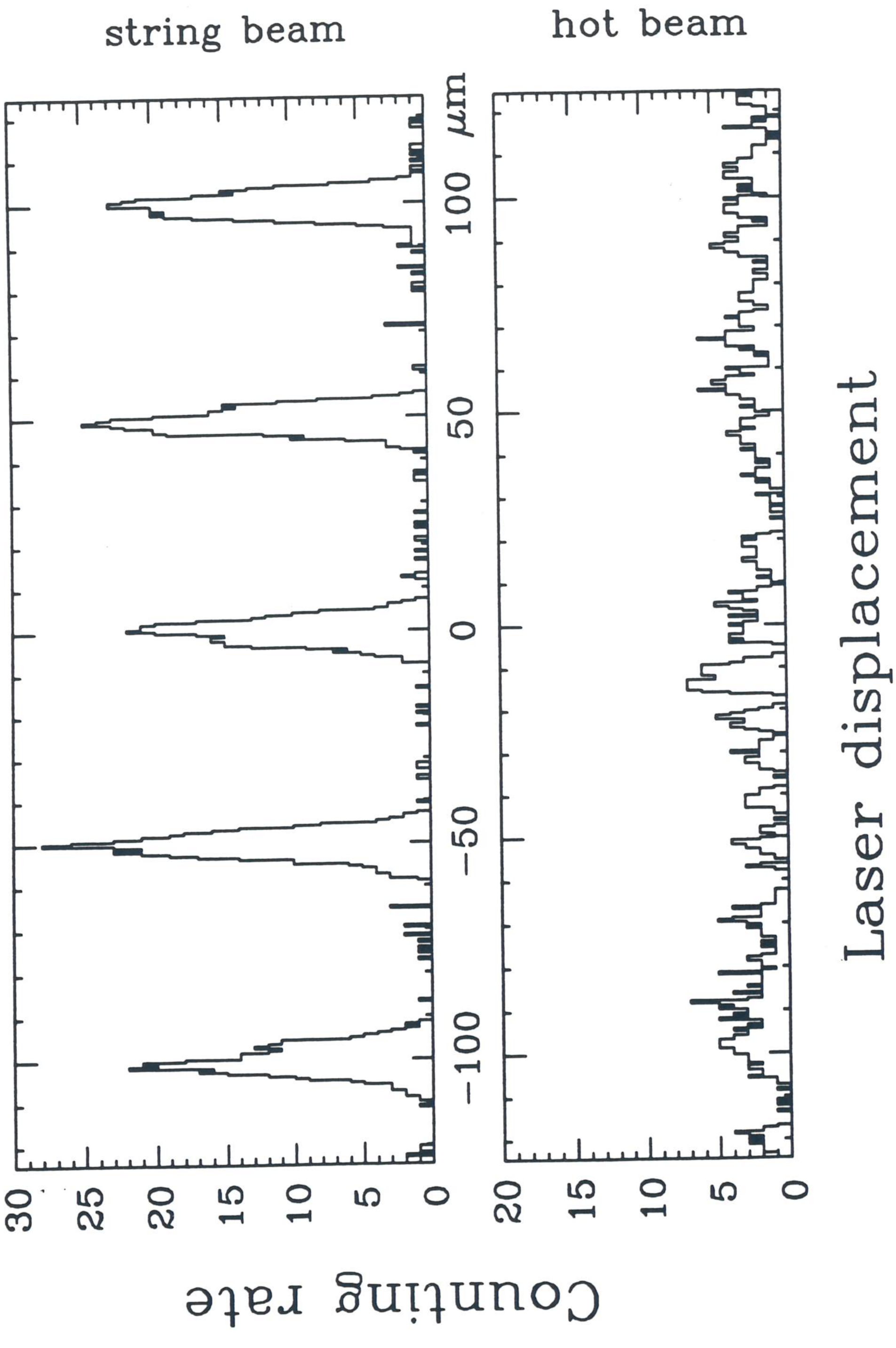

Fig. 4.8 - Counting-rate of coincidences versus second laser position for a string and for a hot beam with the same density. The acquisition time of events for the Monte Carlo is *1 s*.

estimation of the heating rate of the ion beam owing to its interaction time with the laser is given.

Suppose the ion suffering interaction with the light to be at rest in a given frame; when a photon is absorbed the ion receives the impulse of the photon and moves in the direction of the laser beam. Imposing impulse and energy conservation, in the ever valid approximation $\Delta E << mc^2$, where ΔE is the transition energy of the ion and m is the ion's mass, the increase in ion velocity holds:

$$v = \frac{\Delta E}{mc}$$

then the ion emits a photon isotropically. Averaging over several absorption-emission processes, an ion gains a mean transverse velocity according to the previous equation. Thus, each interaction with the laser enhances the transverse kinetic energy by:

$$K = \frac{mv^2}{2} = \frac{\Delta E^2}{2mc^2}$$

This energy is usually referred to as recoil energy.

The energy increase per second of the ion string is K times the frequency of excitations, f, to the upper level for each laser beam. Under the assumption that this energy will be shared to the other particles through intrabeam collisions, the rate of temperature increase for the ion beam is:

$$\frac{dT}{dt} = \frac{2Kf}{N}$$

For the case of $N=8x10^5$ ions of $^{24}Mg^+$ ($K=2.6\ \mu K$) circulating in the ASTRID storage ring and with the above parameters for the diagnostics ($f=2.5x10^6$), it comes out a rate:

$$\frac{dT}{dt} = 1.6x10^{-5}\ \frac{K}{s}$$

From the above calculation it emerges that the perturbation to the ion beam due to the diagnostic device is negligible and should not affect the order within the ion beam.

In the calculation it was assumed that the energy pumped by the laser to the ion beam was perfectly shared by all the ions. In reality, intrabeam scattering for highly cooled beams is expected to be considerably damped and local areas with higher temperature should appear. However, the amount of energy given by the laser to the single ion through excitation is so small that these local temperatures should not affect significantly the order in the beam.

References

[ALE1] A. Aleksandrov et al.; to be Publ. on Rev. Sci. Instrum.

[CLE1] Clerc et al.,;Nucl. Instr. Meth. 113 (1973) 325.

[DEH1] Dehaes et al.; Nucl. Instr. Meth. B13 (1986) 627.

[GAI1] Gaither et al.; Nucl. Instr. Meth. B40-41 (1989) 56.

[HAN1] J.S. Hangst et al.; Phys. Rev. Lett. 67 (1991) 1238.

[KRO1] Kronenberger et al.; Nucl. Instr. Meth. B29 (1988) 621.

[LAN1] L.D. Landau and E.M. Lifshitz, Statistical Physics (Pergamon Press, London, 1958), p. 482.

[STA1] Starzecki et al.; Nucl. Instr. Meth. 193 (1982) 499.

[TEC1} L. Tecchio et al.; CRYSTAL: A Storage Ring for Crystalline Beams (Feasibility Study), LNL-INFN (REP) 0/94 (1994).

5

Performances of the Storage Ring

5.1 The Intrabeam Scattering

The intrabeam scattering is the phenomenon by which particles in the same beam scatter from each other by Coulomb interaction. As they scatter from each other, there is a transfer of longitudinal momentum to the transverse and vice versa, which eventually can lead to an increase of beam dimensions. The amount and the direction of the momentum transfer depends on the lattice properties of the storage ring and on the initial distribution of temperature within the three degrees of freedom.

Intrabeam scattering is a significant effect for heavy ion beam because the large charge state and the relatively low energy. The diffusion rates are calculated with the help of available computer codes which require the lattice functions as input.

The intrabeam scattering diffusion rates are balanced off by the cooling rates for the cooling system. It is important that the balance of the rates occur in all three dimensions at the same time. A stable equilibrium is reached when the diffusion rates, and therefore the cooling rates, in the three directions are all the same.

To simulate the effect of the intrabeam scattering in the CRYSTAL Storage Ring the well known computer code INTRABS [GIA1] has been used. Simulations are done for $2x10^8$ ions of $^7Li^+$, $^9Be^+$ and $^{24}Mg^+$. All ions have the same velocity ($\beta = 0.07$) and the same initial conditions ($\Delta p/p = 10^{-5}$; $\varepsilon = 10^{-8}$ $m\ rad$). *Fig. 5.1a,b,c* shows the intrabeam scattering blow-up for these three kind of ions, in absence of cooling. The two transverse modes are fully coupled.

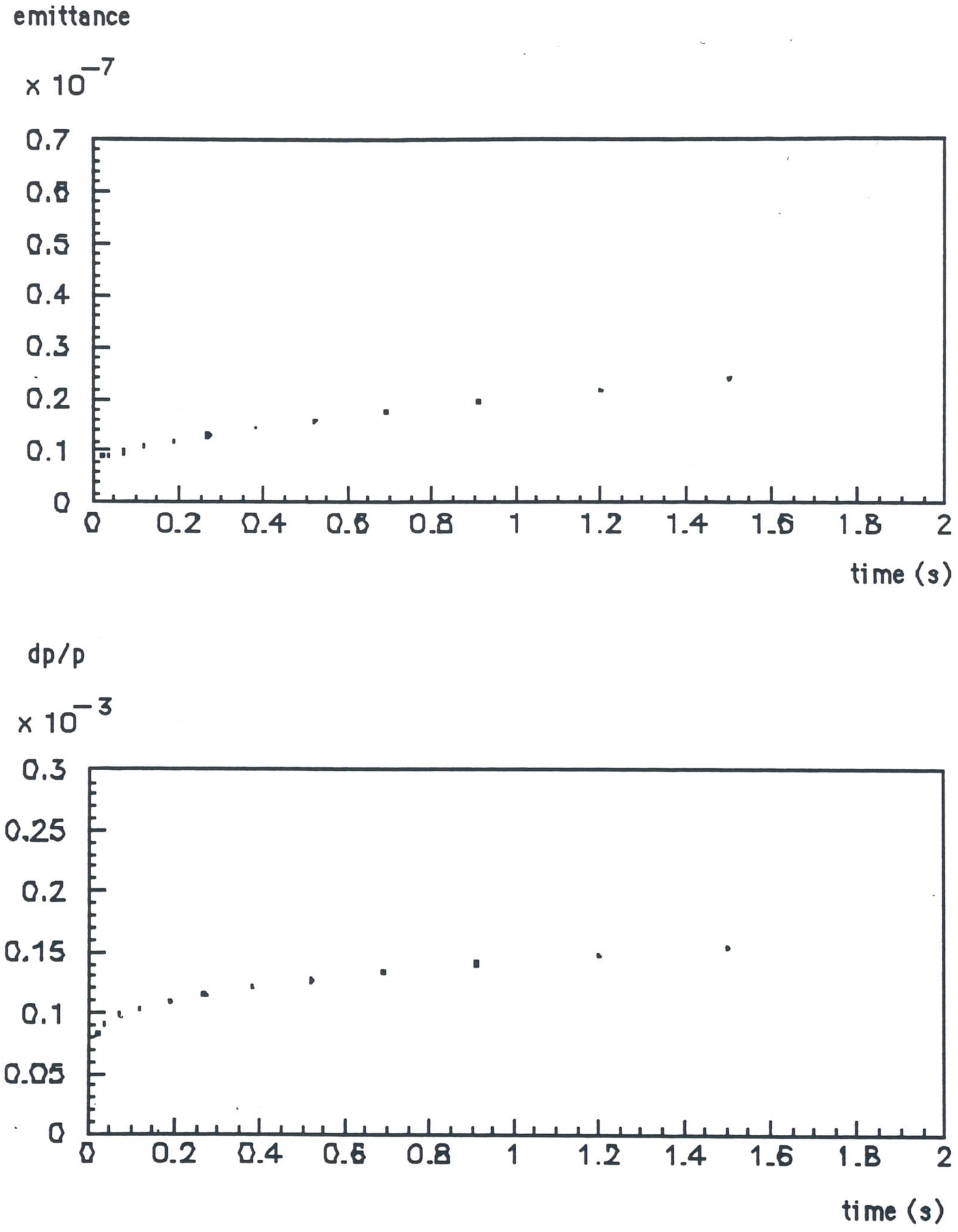

Fig. 5.1a - Intrabeam scattering blow-up for a beam of $^7Li^+$. The initial conditions are: $N = 2x10^8$, $\beta = 0.07$, $\Delta p/p = 10^{-5}$, $\varepsilon = 10^{-8}$ *m rad.*

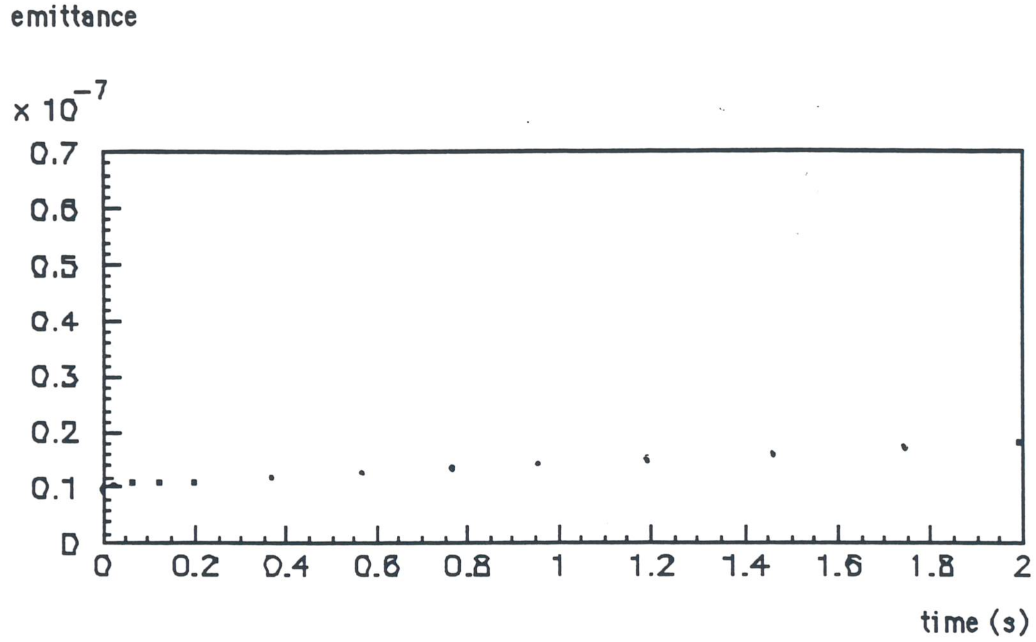

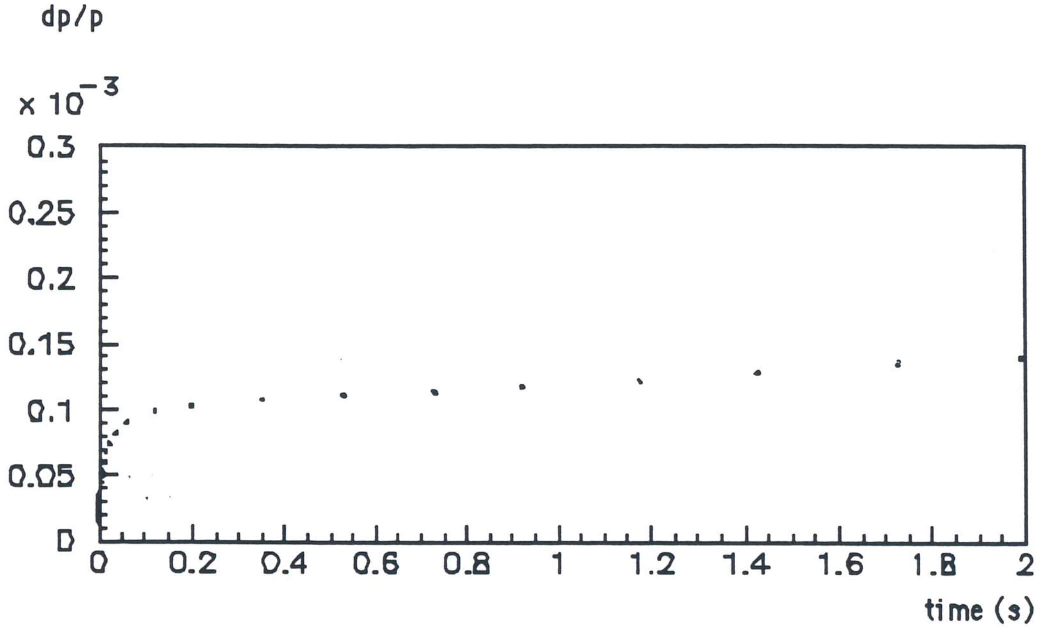

Fig. 5.1b - Intrabeam scattering blow-up for a beam of $^9Be^+$. The initial conditions are: $N = 2x10^8$, $\beta = 0.07$, $\Delta p/p = 10^{-5}$, $\varepsilon = 10^{-8}$ *m rad.*

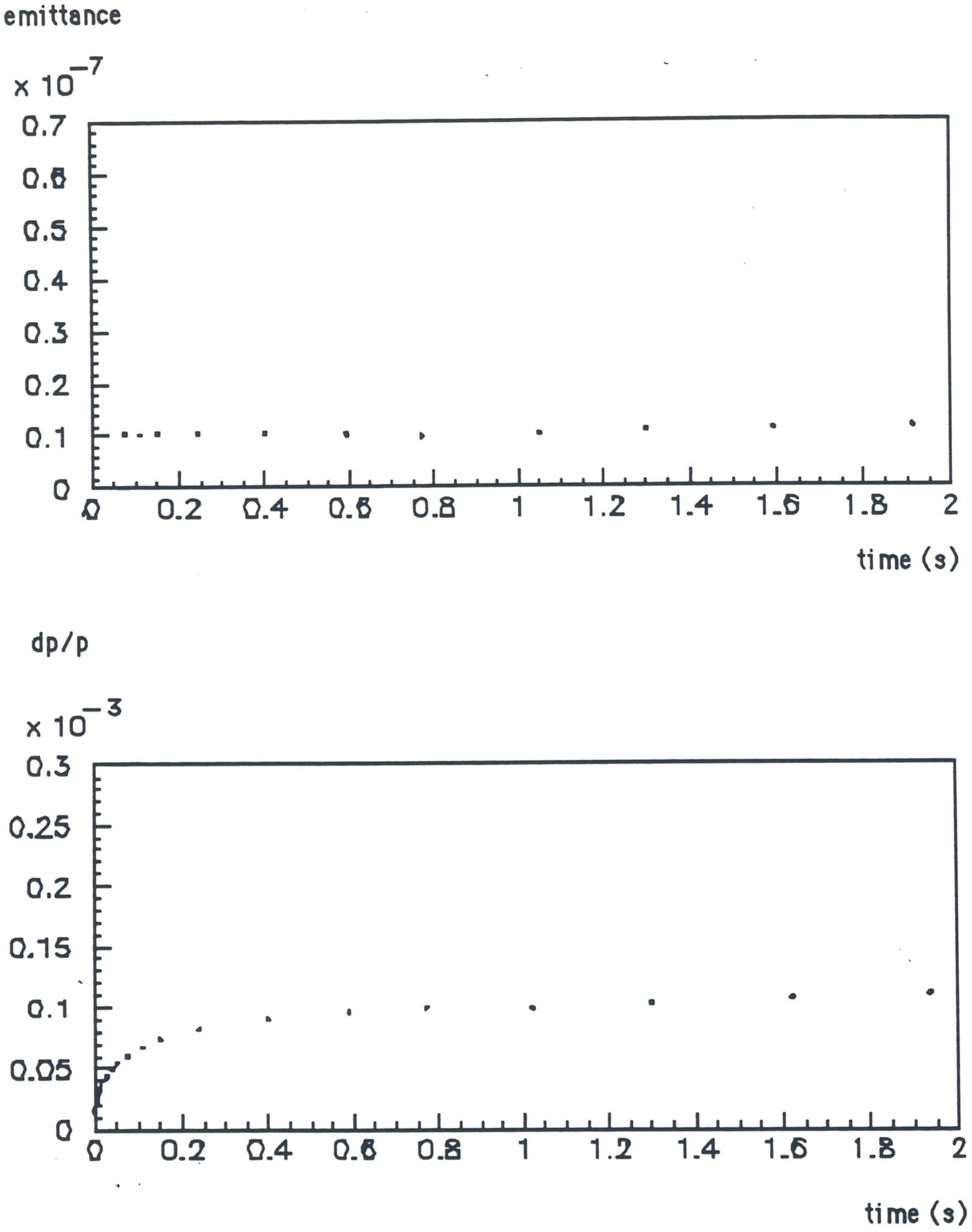

Fig. 5.1c - Intrabeam scattering blow-up for a beam of $^{24}Mg^+$. The initial conditions are: $N = 2x10^8$, $\beta = 0.07$, $\Delta p/p = 10^{-5}$, $\varepsilon = 10^{-8}$ *m rad.*

The intrabeam scattering blow-up times are listed in the *Table 5.1*, for the three kind of ions. Here, the blow-up time is defined as the time needed to increase e-folding times the transverse emittance and the momentum spread.

Table 5.1 - Intrabeam scattering blow-up times for the $^{7}Li^{+}$, $^{9}Be^{+}$ and $^{24}Mg^{+}$. The initial conditions are: $N = 2x10^{8}$, $\beta = 0.07$, $\Delta p/p = 10^{-5}$, $\varepsilon = 10^{-8}$ *m rad.*

Ion	Δp/p Blow-up [ms]	Emittance Blow-up [s]
^{7}Li^{+}	0.680	2.11
^{9}Be^{+}	1.1	2.65
^{24}Mg^{+}	7.1	22.3

The calculated heating times are long enough to be counteract by laser cooling, at least for what concerning the longitudinal mode. Furthermore, more simple Crystalline structures (string and zig-zag) are created with a less beam intensity, so that the heating rate due to intrabeam scattering is lower than the calculated one. New cooling methods for the transverse modes, like the transverse laser cooling and the indirect transverse cooling (see *sect. 2.4.2*), may efficiently counteract the heating on the transverse modes.

Finally, *Fig. 5.2* shows the blow-up times of both transverse and longitudinal modes for the CRYSTAL Storage Ring, in comparison with some of the existing ion storage rings.

A second source of heating, concerning the space charge dominated beams, is connected to the envelope instability (see *sect. 1.*). In CSR this problem is avoided by selecting a proper value for the single particle phase advance per cell, well below *90* degrees.

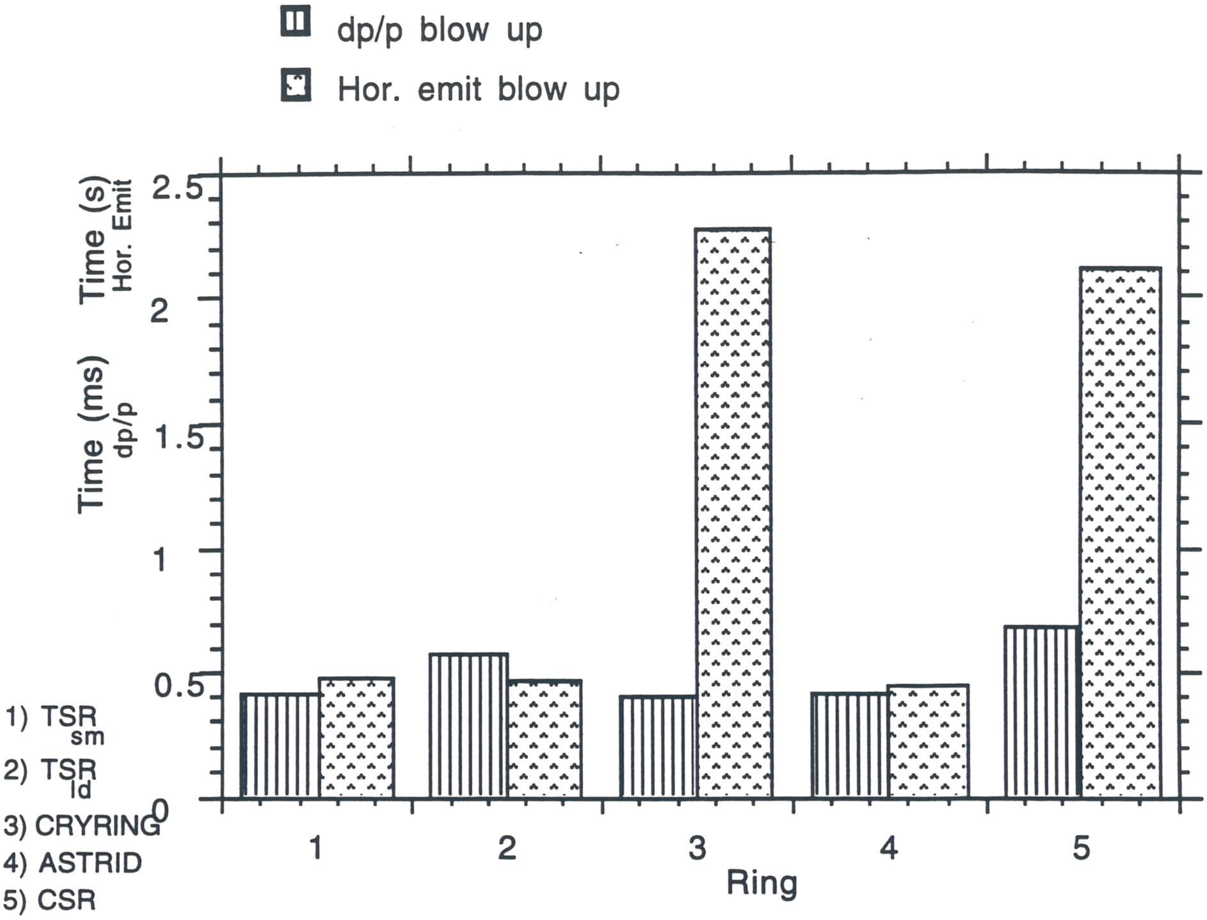

Fig. 5.2 - Blow-up times for the CRYSTAL Storage Ring in comparison with some of the existing ion storage rings. The initial conditions are: $N = 2x10^8$ ions of $^9Be^+$, $\beta = 0.07$, $\Delta p/p = 10^{-5}$, $\varepsilon = 10^{-8}$ *m rad.*. The blow-up times are given in [*ms*] for the longitudinal modes and in [*s*] for the transverse ones.

5.2 Phase Transitions of Cold Ion Beams

Phase transitions in a confined ionic system have been found by computer simulations [RAH1, HAS1] and later experimentally confirmed in ionic traps [BIR1, WAK1]. In the case of the ion traps, the simulations of ground states have been done considering a longitudinal homogeneous and transversally isotropic straight linear focusing channel. For a anisotropic focusing trap, where the transverse focusing is the same in both directions and the longitudinal focusing is different from the transverse ones, phase transitions have been studied as a function of the anisotropy [SCH2].

Particle motion in a storage ring is intrinsically more complicated because of the particle angular velocity and the AG focusing. Recently, analytical and numerical simulation studies have shown that ground states may exist in a storage ring operating below the transition energy and the effect of the curvature (shear) can be overcome [BIS1, RUG1,WEI1].

On the basis of this knowledge the phase transitions of cold ion beams in a storage ring are numerically simulated. The ground states are determined in function of the focusing parameters.

5.2.1 Determination of Ground States

In analogy with the simulations in ion traps, the ground states of Crystalline Beams in a storage ring are determined by solving the equations of motion derived from the general Hamiltonian [BUR1, WEI1]. In the rest frame, particles in a storage ring are described by the following Hamiltonian (see *sect. 1.2*):

$$H = \frac{1}{2}\left(p_x^2 + p_y^2 + p_z^2\right) - \gamma h x p_z + g_x \frac{x^2}{2} + g_y \frac{y^2}{2} + \xi \sum_i \frac{1}{r_i}$$

where p_x, p_y and p_z are the canonical momenta of a particle, x, y, z are they coordinates. $h(\theta)=R/\rho(\theta)$ is the dimensionless curvature, θ is the azimuth (time), $g_x(\theta)=(1-k/h^2)h^2$, $g_y(\theta)=k$ are the focusing functions and r_i is the distance between particles. The last term takes into account the Coulombian interactions between particles, where

$$\xi = \frac{Z^2}{A} \frac{R^2 r_p}{d^3 \beta^2 \gamma^2}$$

is the dimensionless space charge parameter, r_p is the classical radius of the proton, $d=2\pi R/N$ is the inverse longitudinal density where N is the number of particles, Z and A are the ion charge and mass respectively.

Respect to the case studied by Hasse and Schiffer [HAS1] we can derive analogous structure parameters:

$$\lambda_x = \left[\frac{3\xi}{2\left(Q_x^2 - \gamma^2\right)}\right]^{1/3}, \lambda_y = \left(\frac{3\xi}{2Q_y^2}\right)^{1/3}$$

but different in the two planes. In the case of a zero curvature and an isotropic focusing these parameters turn to the parameters introduced in *Ref.* [HAS1].

Both the structure parameters are proportional to the linear density $1/d$, with a constant that depends on focusing, main energy and ion kind. Every ground state configuration is defined in a range in λ_x, λ_y domain, and therefore in a range of density. The extreme values (critical values) of such range correspond to the stability limits. When the limit is reached the ground state in examination became unstable and a new structure appears. At very low densities the particles are aligned along the direction of motion and at higher densities more complicated structures appear.

The ground states have been investigated by mean of the computer code PARMT [STR1]. The code generates a semi-Gaussian distribution of particles, i.e. homogeneous point density in the transverse position space and gaussian density distribution in the transverse velocity phase. A periodically repeating segment of given length is used as simulation ensemble to calculate interaction forces. The cooling force is applied at appropriate location in the ring and the beam temperature is reduced each turn. The effect of cooling on the ions is simulated by reducing in each turn the ion divergencies by a given factor K.

As an example, a beam of $^9Be^+$ with $\beta = 0.07$ and initial emittance $\varepsilon = 1\pi$ *mm mrad* is studied. The results are very general, and can be extended to every ion species of different charge state and energy.

For the simulation of particle beams, the Coulomb forces have to be taken into account. Considering the integral form of the Poisson equation, for the discrete distribution of a single specie of ions with the charge Z, result:

$$\vec{E}(x) = \frac{Z}{4\pi\varepsilon_0}\sum_i \frac{\vec{x} - \vec{x}_i}{\left|\vec{x} - \vec{x}_i\right|^3}$$

To obtain the correct fields at the beam boundaries, the equation has to include also the image charges. Assuming the radius of the beam much less than the beam pipe radius, the transverse image forces can be neglected. For coasting beams the simulation can be confined to a beam unit of a length L that is periodical along the beam. Then, the equation for the z-component of the electric field at the location of the j-th particle reads:

$$E_{z,j} = \frac{Z}{4\pi\varepsilon_0}\sum_{i\neq j}\left\{\frac{z_j - z_i}{\left[\left(x_j - x_i\right)^2 + \left(y_j - y_i\right)^2 + \left(z_j - z_i\right)^2\right]^{3/2}}\right.$$

$$\frac{z_j - L - z_i}{\left[\left(x_j - x_i\right)^2 + \left(y_j - y_i\right)^2 + \left(z_j - L - z_i\right)^2\right]^{3/2}} +$$

$$\left.\frac{z_j + L - z_i}{\left[\left(x_j - x_i\right)^2 + \left(y_j - y_i\right)^2 + \left(z_j + L - z_i\right)^2\right]^{3/2}}\right\}$$

For completeness the lattice perturbations, i.e., misalignments, fringe fields, etc., are also included in the simulation.

Ground states can be described in function of the linear density and structure parameters λ_x, λ_y. Introducing the anisotropy parameter α, defined as:

$$\alpha = \frac{\lambda_y}{\lambda_x}$$

every Crystalline structure can be described in terms of linear density and of anisotropy parameter. Simulations are made for

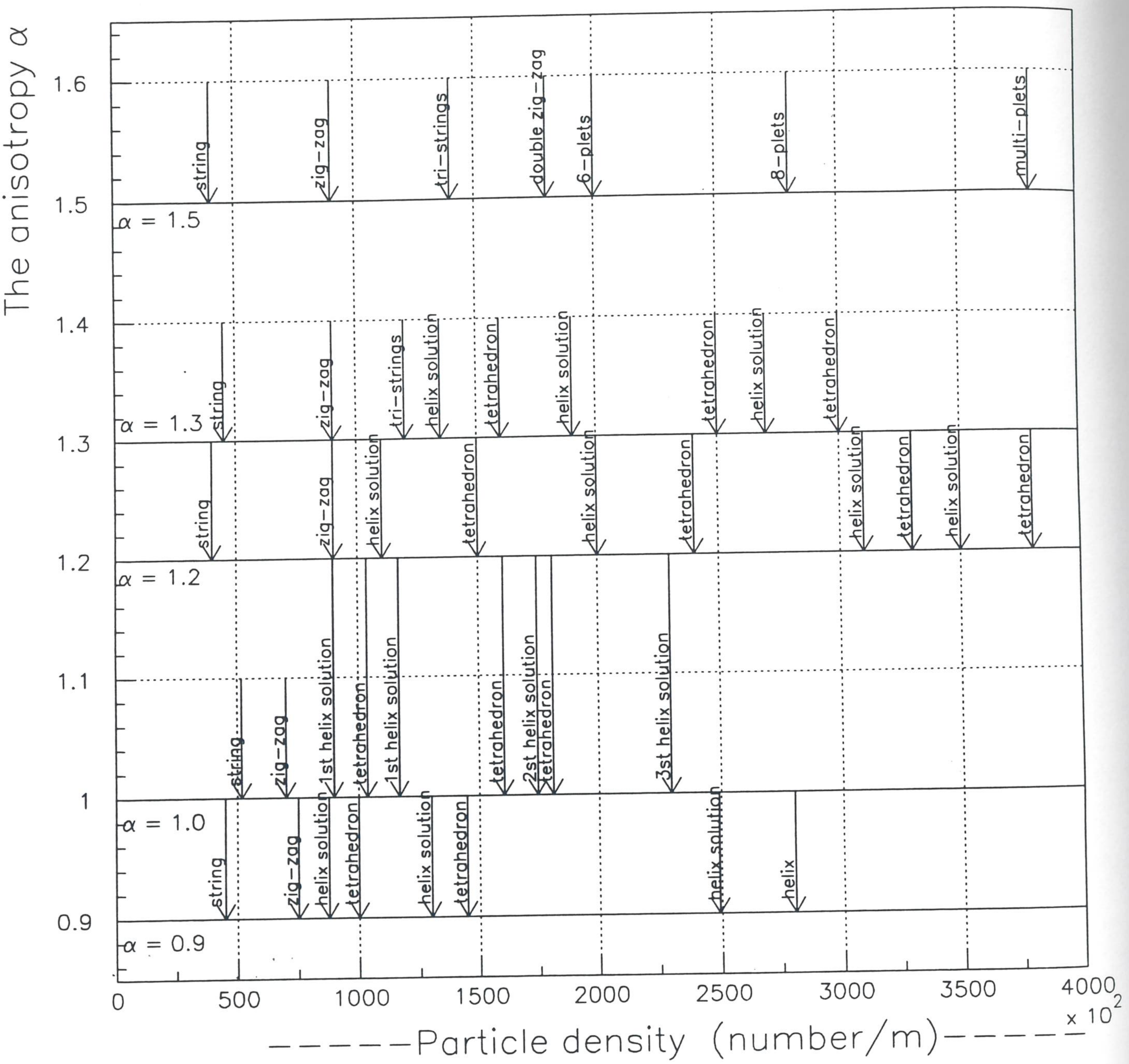

Fig. 5.3 - Phase transitions of different ground states, in function of the linear density and of the anisotropy parameter.

different linear density and $0.9 < \alpha < 1.5$. *Fig. 5.3* shows the phase transition diagram, in which the thresholds for different ground states are indicated. In other words, the phase transitions for different crystalline structures are defined only by the machine tunes and the particle linear density. The basic structures are the helix and twisted multiplets; some of them are displayed in *Fig. 5.4-8*, for different α-parameters and linear densities.

In all cases considered, at very low linear density the particles are always strung out along the z-axis as a string, then increasing the density a zig-zag appears and so on, up to obtain $3D$-structures. Structure configurations different than string and zig-zag are not unique and depend on the value of the parameter α.

Simulations have been done for large linear density structures up to double shells, for $\alpha = 1.2$. Their transverse projections are shown in *Fig. 5.9a*; inside the first shell the particles again start to appear on the axis, the new string turns into a multiplet as the linear density increases. *Fig. 5.9b* shows a side view of a typical structure where the particles from the outer shell are plotted as if the mantle were the plane of the drawing. This picture clearly shows the hexagon patterns that are typical of Crystalline structures. Furthermore, the dependence of the transverse beam sizes on the particle density is plotted in *Fig. 5.10*.

In a storage ring, usually the focusing conditions in the two transverse planes are different. From the Hamiltonian, assuming the transverse emittance of Crystalline Beams very small, it is possible to derive the ratio of maximum transverse sizes (a_x, a_y) of ground states in function of α-parameter. This can be written as:

$$\alpha^3 = \frac{a_y}{a_x}$$

and thus, the ratio is completely defined by the α-parameter. *Fig. 5.11* compares analytical results with numerical simulations.

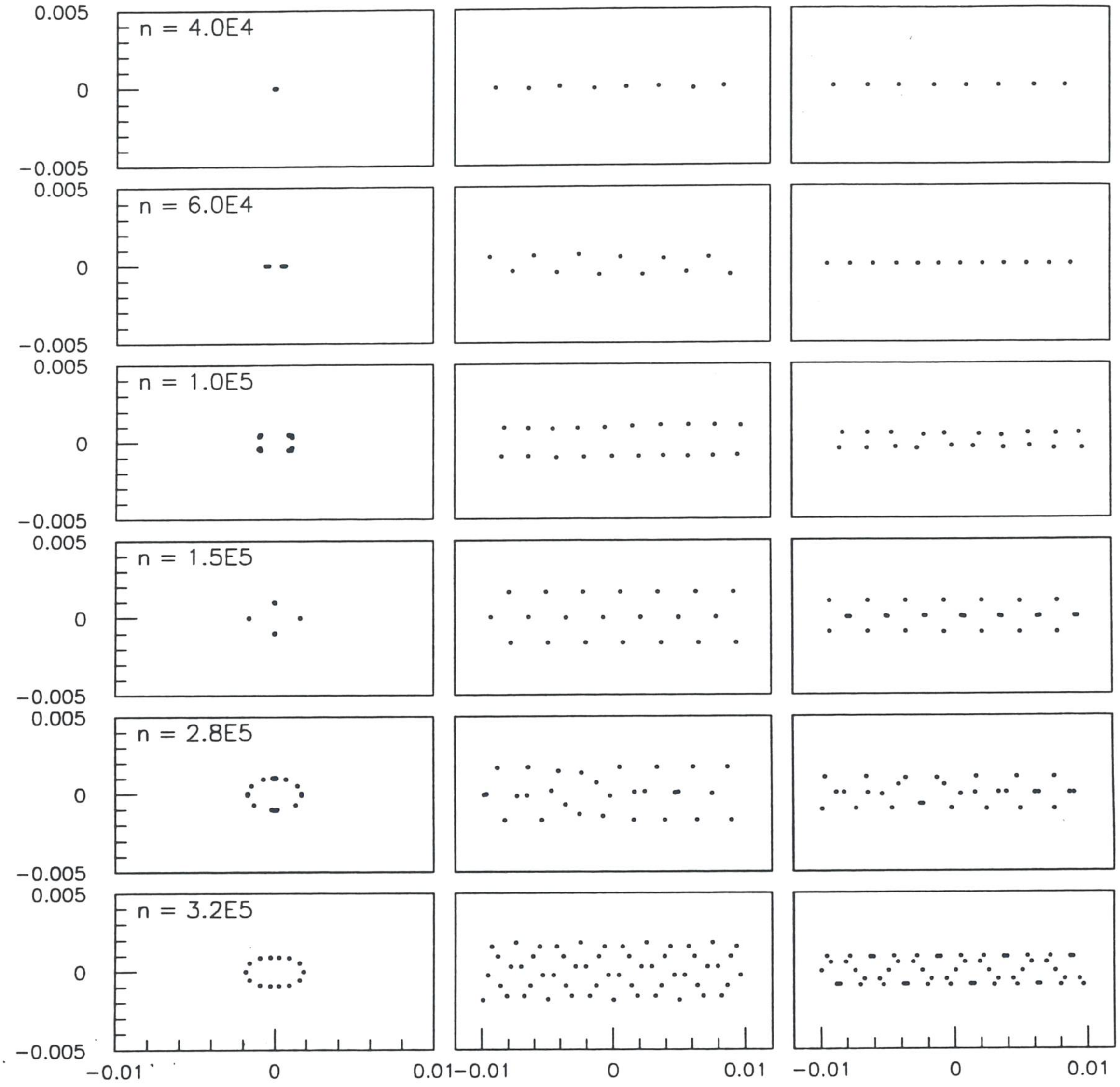

Fig. 5.4 - Ground state configurations for $\alpha = 0.9$. From left to right, projection of particles onto the x-y, z-x and z-y planes. The dimensions are in centimeters.

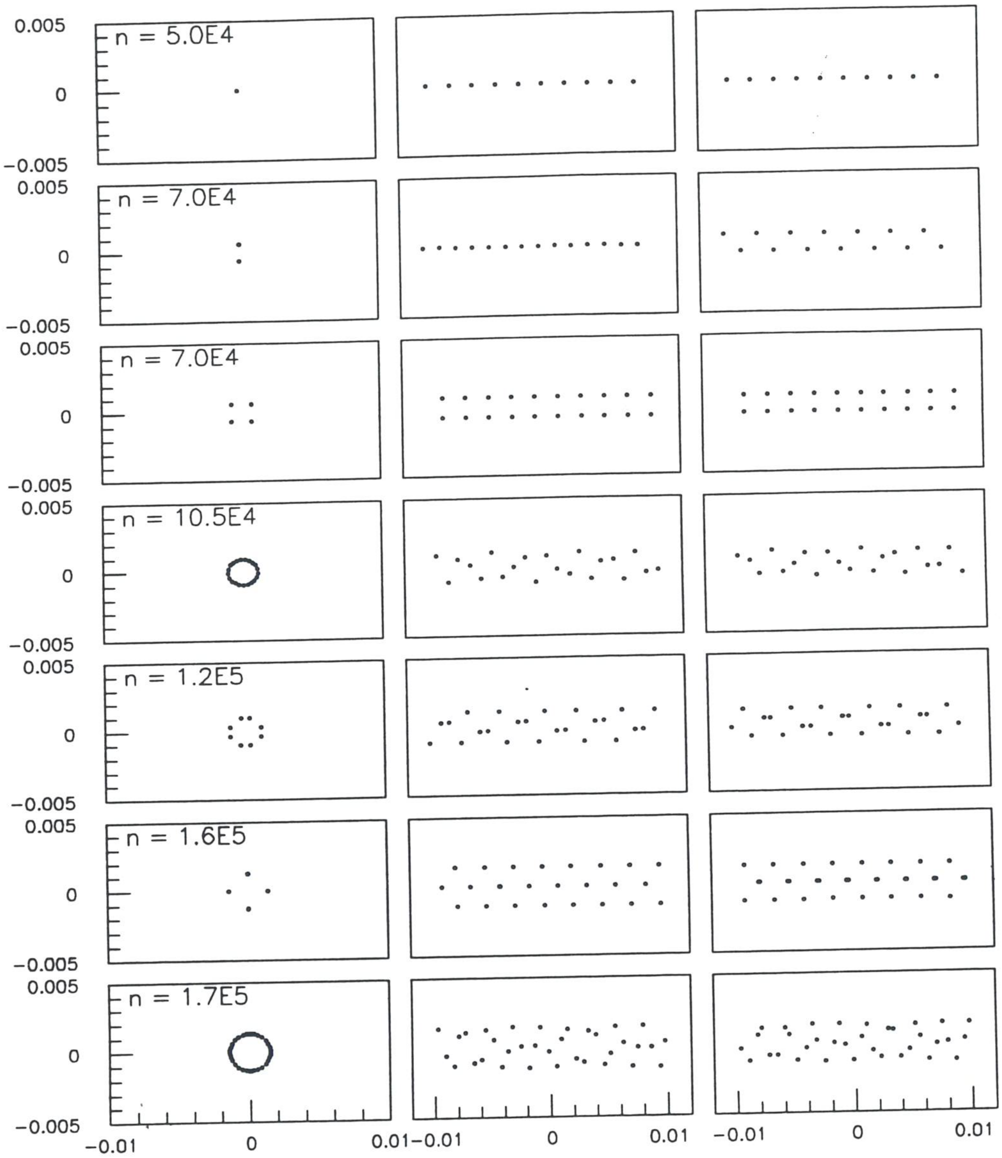

Fig. 5.5 - Ground state configurations for $\alpha = 1.0$. From left to right, projection of particles onto the x-y, z-x and z-y planes. The dimensions are in centimeters.

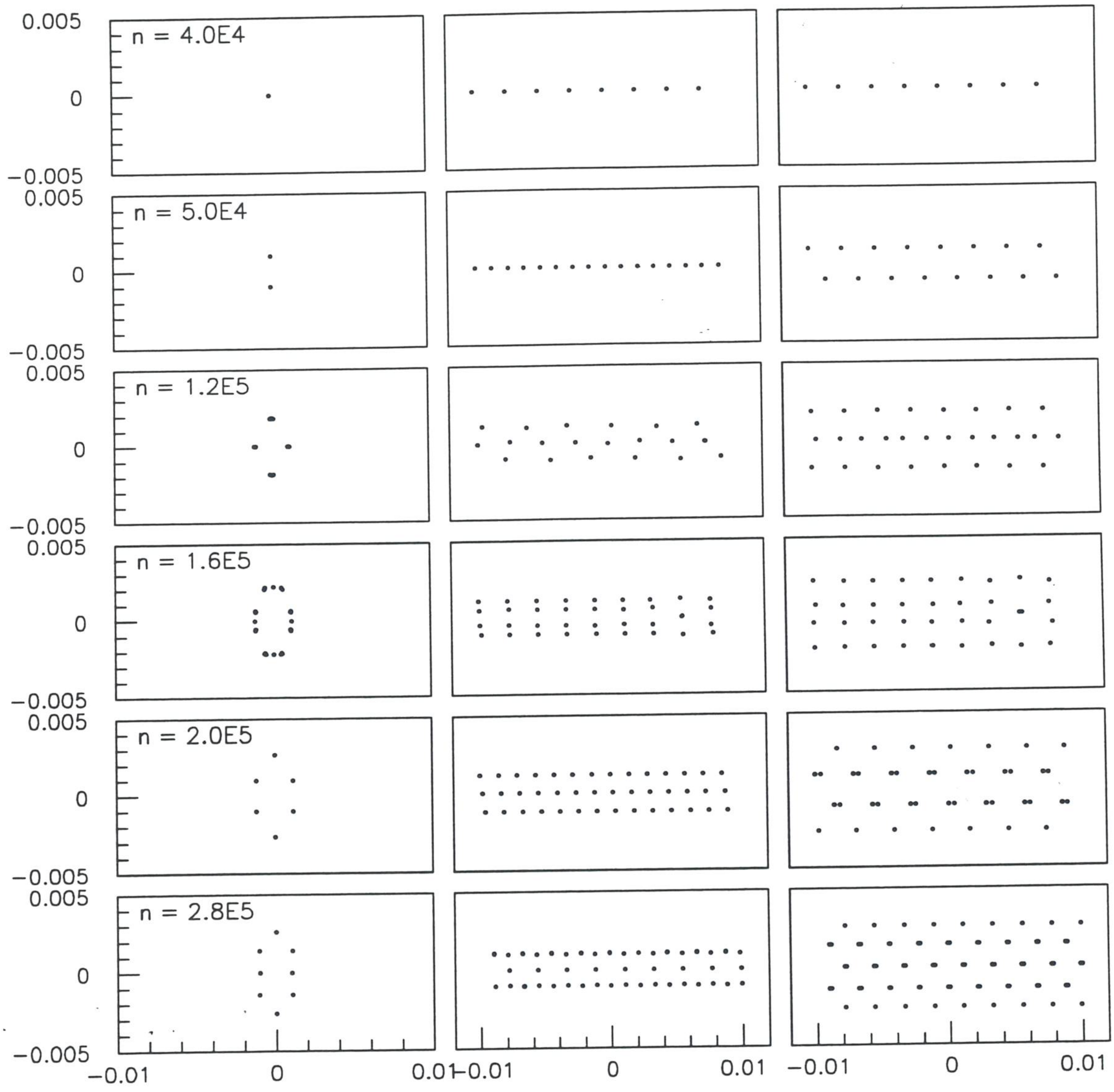

Fig. 5.6 - Ground state configurations for α = *1.2*. From left to right, projection of particles onto the x-y, z-x and z-y planes. The dimensions are in centimeters.

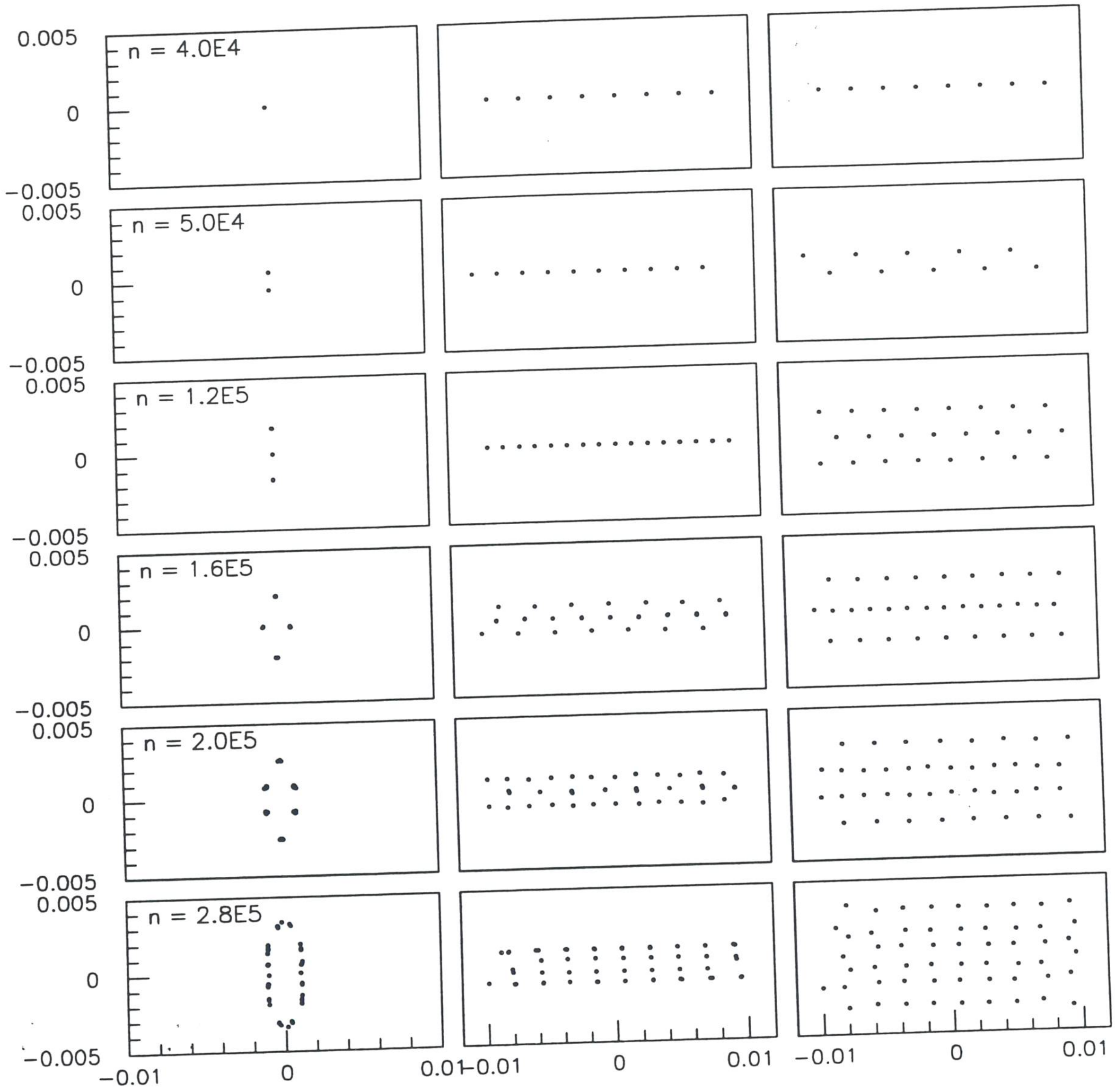

Fig. 5.7 - Ground state configurations for $\alpha = 1.3$. From left to right, projection of particles onto the x-y, z-x and z-y planes. The dimensions are in centimeters.

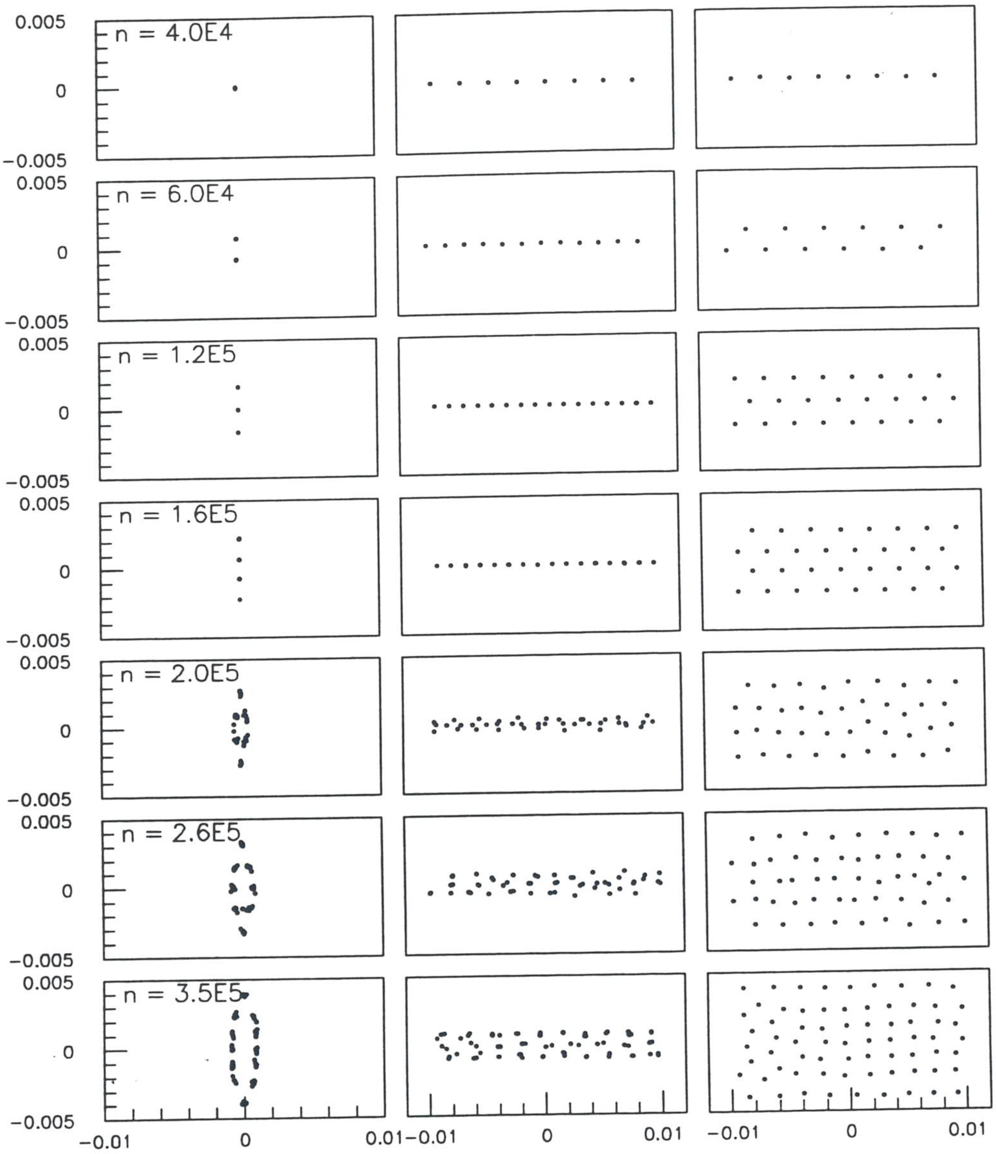

Fig. 5.8 - Ground state configurations for $\alpha = 1.5$. From left to right, projection of particles onto the x-y, z-x and z-y planes. The dimensions are in centimeters.

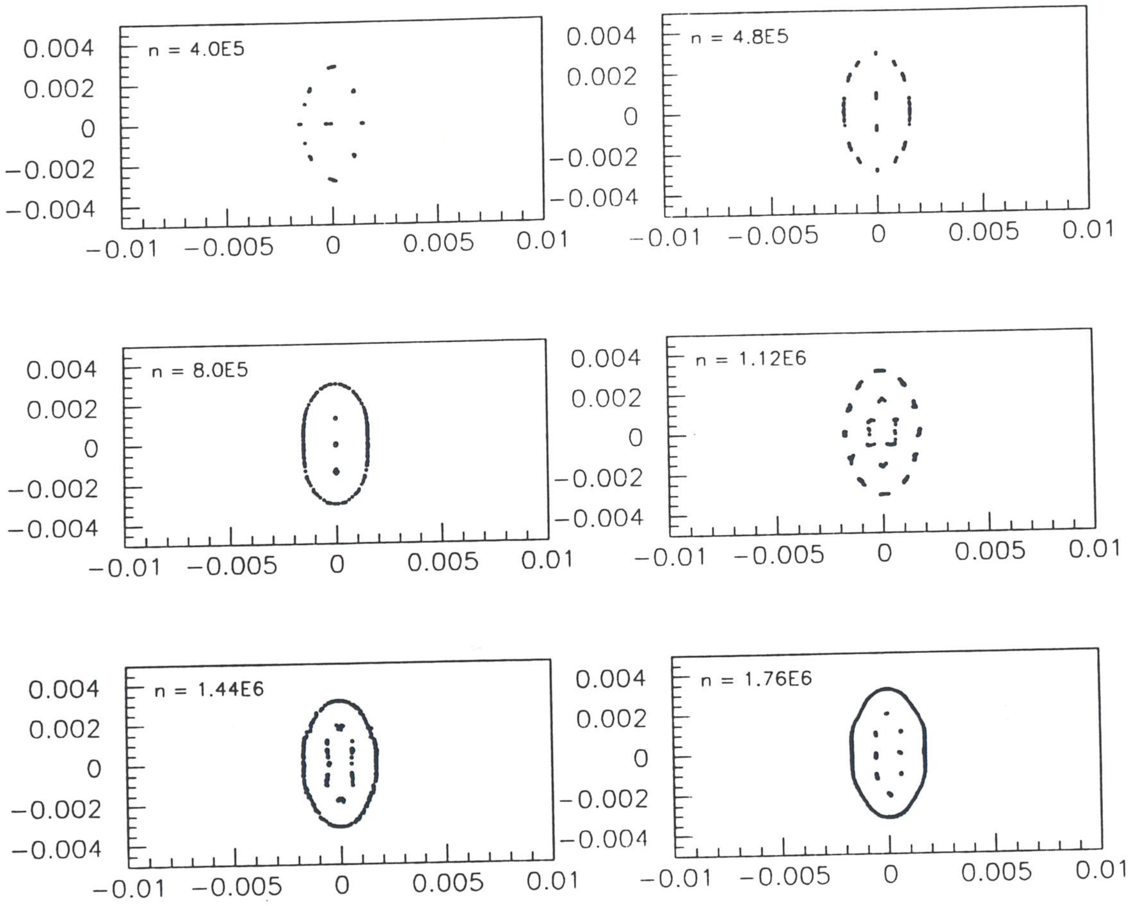

Fig. 5.9a - Double shell configurations in function of different densities, for $\alpha = 1.2$. Particles are projected on the transverse plane. The dimensions are in centimeters.

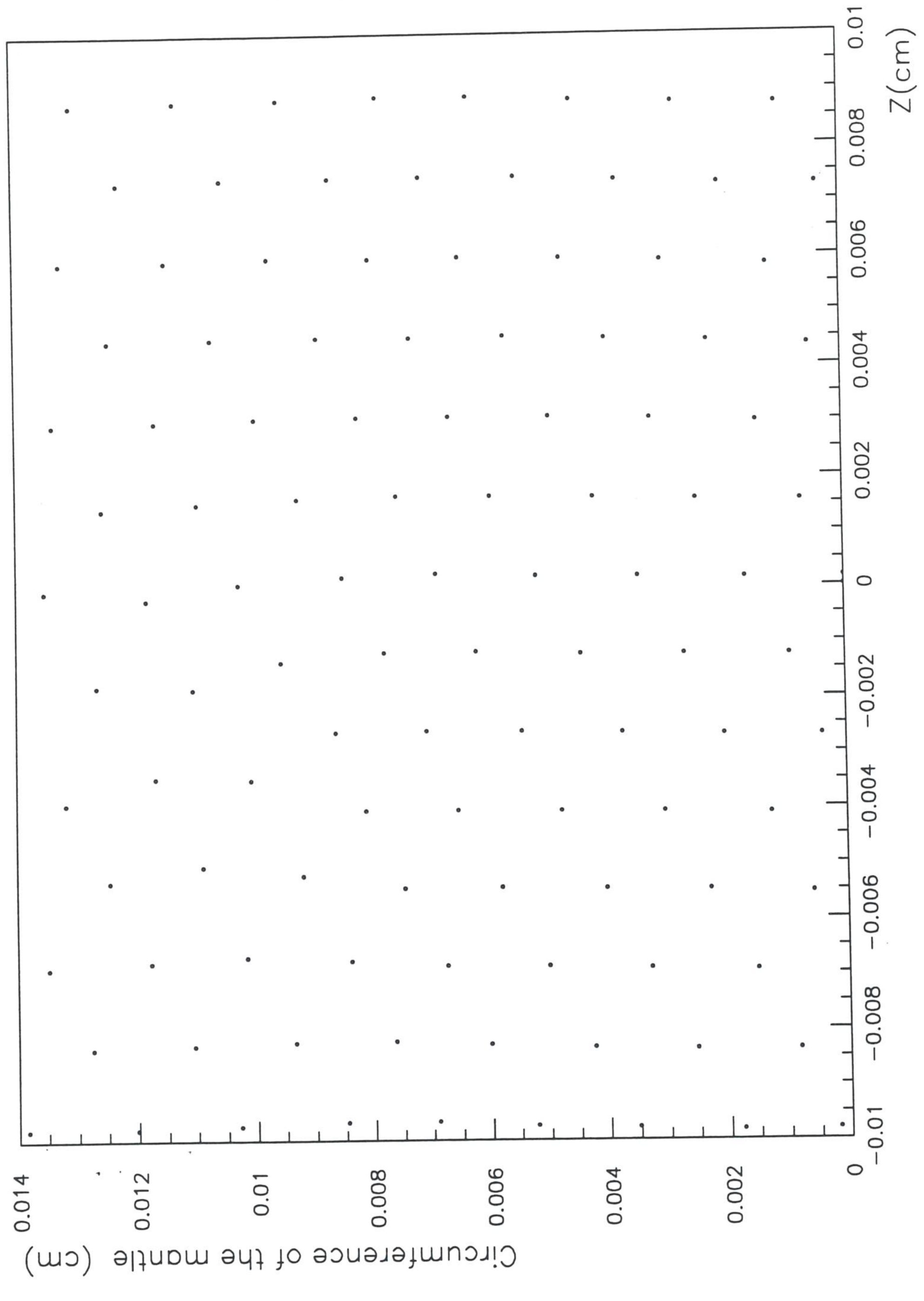

Fig. 5.9b - Double shell configurations in function of different densities, for $\alpha = 1.2$. Particles of the outer shell are plotted as if the mantle were the plane of drawing. The dimensions are in centimeters.

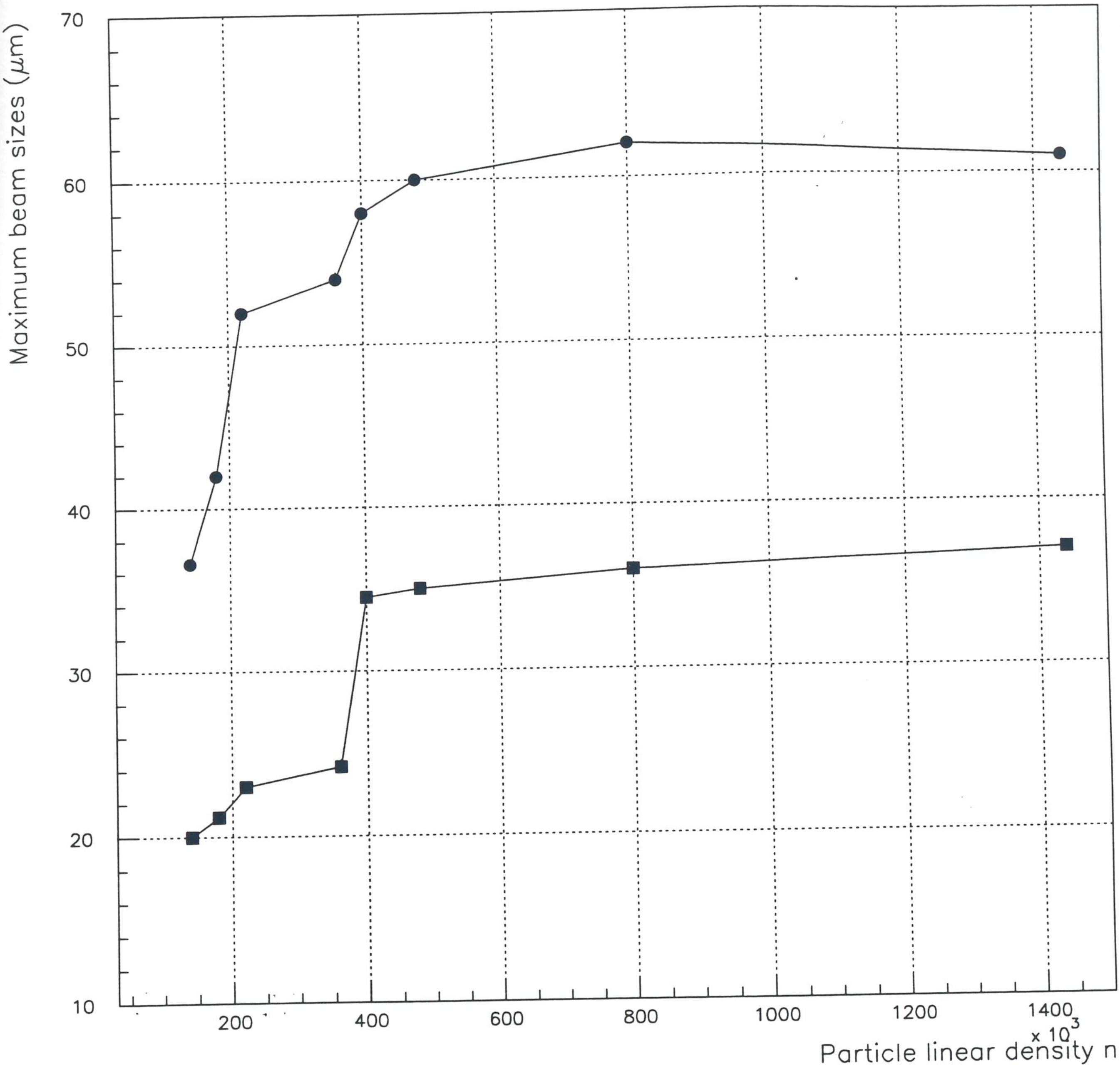

Fig. 5.10 - Transverse beam size in function of the linear density, for α = *1.2.* ■ horizontal dimension and ● vertical dimension.

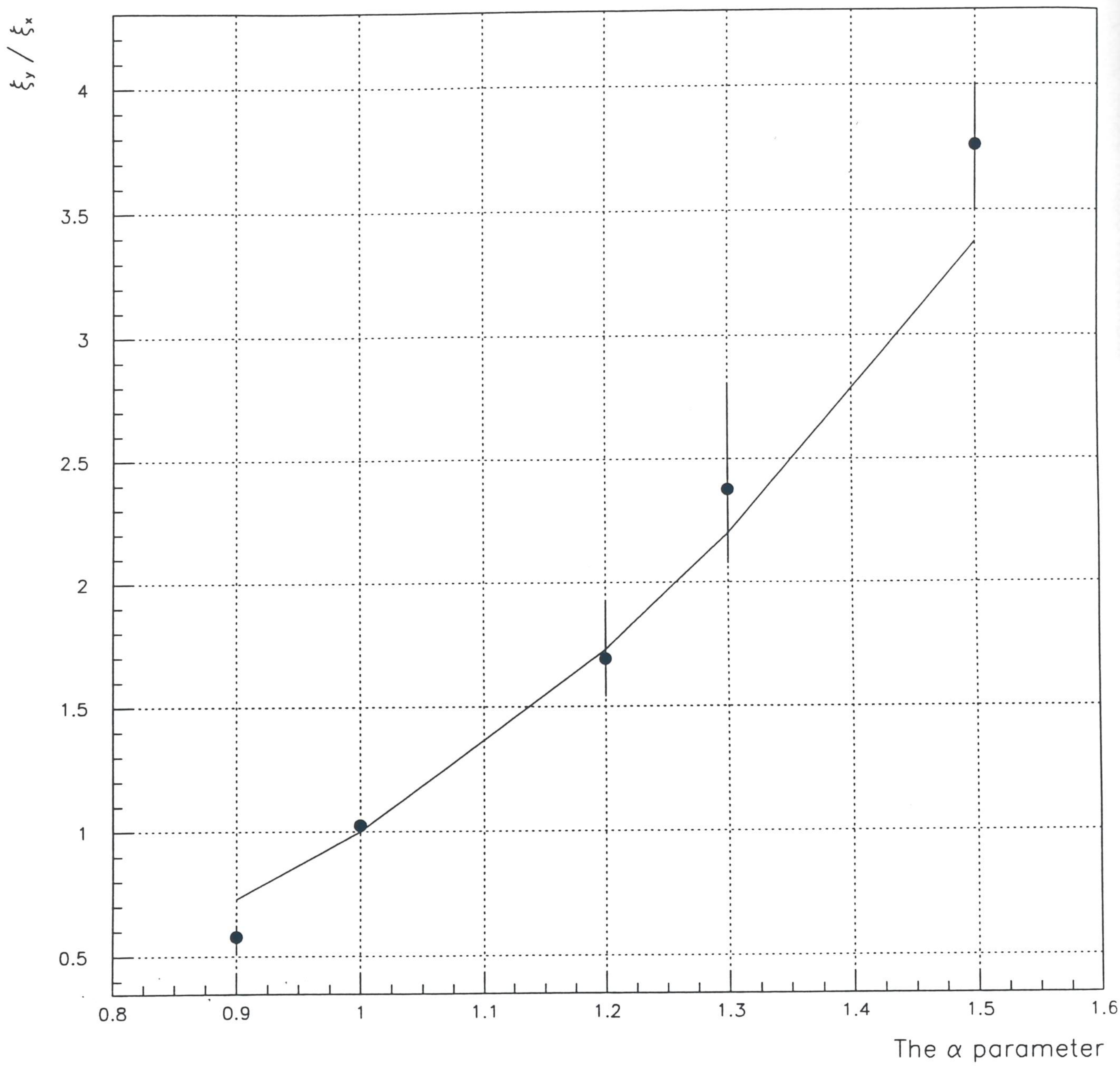

Fig. 5.11 - Ratio of the maximum transverse beam sizes as a function of the α-parameter. Comparison between numerical simulations (dots) and analytical calculations (full line).

5.2.2 The String and the Zig-zag Cases

In the previous section the possible existence of ground states in the CSR beams has been demonstrated. The ground states have been obtained by simulating the cooling of a hot beam until reaching Crystalline structures. To avoid the huge computing time demanded to obtain such complex structures an unrealistic cooling factor has been used. To demonstrate the possibility to reach Crystalline Beams using a realistic cooling factor the simple case of string and zig-zag configurations are investigated.

Numerical simulations are done by using the computer code PARMT. A typical laser cooled $^9Be^+$ ion beam is considered; the initial condition at the injection are the following: $\varepsilon = 1\pi$ *mm mrad*, $\Delta p/p = 10^{-4}$, $\beta = 0.07$, $N = 2.7x10^5$ - $3x10^6$. The cooling factor used in the simulation is $K = 1.0004$ for the string and $K = 1.003$ for the zig-zag, corresponding to *11 ms* and *1 ms*, respectively. Compared with the experimental values for the longitudinal laser cooling, the cooling factors are quite close to the realistic ones. The difference is that here the same cooling rate is applied in the longitudinal direction as well as in transverse one. The simulations are done for the realistic storage ring and take into account misalignments, fringe fields, orbit perturbations, fiels errors, etc.

Fig. 5.12 shows both the results relative to a string and a zig-zag configuration, while *Table 5.2* summarizes the main parameters of the simulation.

For the string a plasma parameter $\Gamma = 11$ has been obtained, which corresponds to a beam temperature *of 1.8 mK.* The interparticle distance results to be $260\ \mu m$. The critical ion spacing for a string is $L_0 = 75\ \mu m$, corresponding to about 10^6 circulating ions. At the critical ion spacing the string configuration becomes unstable and a new Crystalline structure (zig-zag) appear.

Since the focalization is predominant in the horizontal plane the resulting structure is a vertical zig-zag. The simulation for the zig-zag gives a plasma parameter $\Gamma = 46$, which corresponds to a beam temperature of *7.6 mK*. The interparticle distance is *30 μm* longitudinally and *8 μm* vertically.

Table 5.2 - Main parameters from the simulation of string and zig-zag configurations.

Parameter	String	Zig-zag
Number of Ions	2.7×10^5	3×10^6
Initial Emittan. [π mm mrad]	1	1
Reduction Factor (cooling)	1.0004	1.003
Long. Interpart. Dist. [μm]	260	30
Trans. Interpart. Dist. [μm]	-	8
Plasma Parameter Γ	11	46
Beam Temperature [mK]	1.8	7.6

Notice that the zig-zag configuration, as well as the string one, is not affected by the curvature when traveling across the dipole magnets.

Similar results can be obtained simulating different ion species. The $^9Be^+$, as well as $^7Li^+$ and $^{24}Mg^+$, are the more probable candidates for Crystalline Beams. Laser cooling associated to other cooling techniques (indirect cooling, RF cooling, etc.) offers a good possibility to attain Crystalline Beams.

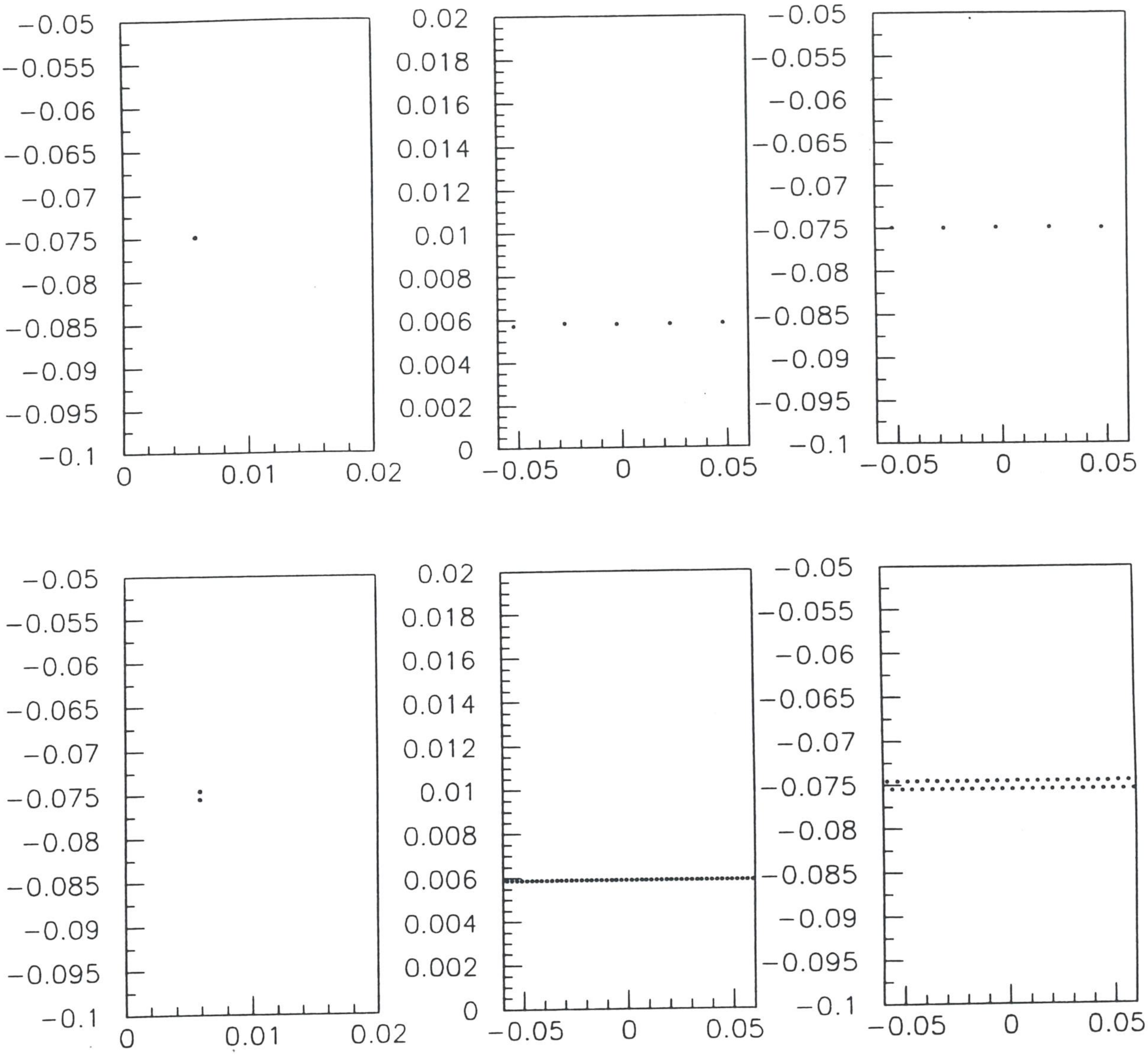

Fig. 5.12 - Simulations of string and zig-zag configurations, for the realistic storage ring. The ions are $^{9}Be^{+}$ with $\beta =$ *0.07*. The dimensions are in centimeters.

References

[BIR1] G. Birkl et al.; Nature 357 (1992) 310.

[BIS1] G. Bisoffi et al.; "CRYSTAL: A Dedicated Storage Ring for Ion Beam Crystallization", Proc. of the Workshop on Beam Cooling and Related Topics, Montreux (1993), ed. J. Bosser, CERN 94-03, Geneva 1994.

[BUR1] AV. Burov; "Steady States and Eigenmodes of a Crystal Beam in a Storage Ring", Submitted to Part. Acc.

[GIA1] R. Giannini and D. Moehl; "INTRABS Computer Code", CERN PS 1993.

[HAS1] R.W. Hasse and J.P. Schiffer; Ann. Phys. 203 (1990) 419.

[RAH1] A. Rahman and J.P. Schiffer; Phys. Rev. Lett. 57 (1985) 1133.

[RUG1] A.G. Ruggiero et al.; Matrix Formulation of the Particle Motion in Crystalline Beams, EPAC 94 (1994) 1382.

[SCH2] J.P. Schiffer; Phys. Rev. Lett. 70 (1993) 818.

[STR1] J. Struckmeier and I. Hoffman, GSI-ESR-87-03 (1987).

[WAK1] I. Waki et al.; Phys. Rev. Lett. 68 (1992) 2007.

[WEI1] J. Wei et al.; Phys. Rev. Lett. 73 (1994) 3089.

6
Cost Estimate and Schedule

6.1 Cost Estimate for the CSR Project

This conceptual design report is adequate to provide a baseline for a cost estimate of the project. The estimate is also based on a comparison with similar projects. Finally, experience gained in the design and construction of the ALPI post-accelerator has also been useful for the estimation of the cost of many components.

The detailed costs estimate of the main components are shown in *Tables 6.1-2* and summarized in *Table 6.3*. Cost estimate is done only for the CSR operating in the Crystalline mode. Here, the possibility to implement the storage ring for other applications is not considered.

In first analysis, the construction of the transfer line ALPI-CSR is disregarded. A dedicated low energy injector for $^{7}Li^{+}$, $^{9}Be^{+}$ and $^{24}Mg^{+}$ is more suitable for Crystalline Beams. The CHORDIS source can supply a variety of ions (up to Bismuth) with different charge state.

The total cost is *28 billion Italian Lire* in *1995* estimate, of which *26 billion Lire* are required for the completion of the storage ring and *2 billion Lire* for the R&D.

Table 6.1 - Cost Breakdown of the Storage Ring.

Magnets:	8 Dipoles	4.3	GL
	32 Quadrupoles		
	32 Sextupoles		
	Correcting Dipoles		
DC Power Supply		1.5	
Injection/Abort Systems		0.7	
Vacuum		3.3	
Diagnostics:	Schottky Pick-ups	3.0	
	Magnesium Jet		
	Laser		
	BPM		
Electron Cooling 20 KeV		1.2	
Laser Cooling		1.5	
Control System		2.0	
Injector		1.5	
Storage Ring	**Total**	**19.0**	**GL**

Table 6.2 - Cost of Civil Engineering.

Building		4.0	GL
Engineering Plant:	Electrical	1.5	
	Cooling	1.5	
Civil Engineering	**Total**	**7.0**	**GL**

Table 6.3 - Total Cost of the CRYSTAL Storage Ring Project.

Civil Engineering.	7.0	GL
Storage Ring (Crystalline Mode)	19.0	
R&D Program	2.0	
Total Cost of the Project	**28.0**	**GL**

6.2 Construction Time Schedule

The scale of the project is such that it can be built over a five-years period. It is proposed that the construction of the Storage Ring itself will begin in *January 1997,* while the construction of the building will begin in the *1996*. *Table 6.4* shows the time construction schedule and *Fig. 6.1* shows the funding profile. Commissioning of the CRYSTAL Storage Ring begins at the end of the year *2000*, and is expected to take one year.

This profile assumes an adequate period *(1995-98)* of design and of R&D program, required to freeze major parameters and details of components, expecially in the area of diagnostics for Crystalline Beams and laser cooling. The funding required for this R&D program amounts to about *2.0 GLit* divided as shown in *Fig. 6.1*.

Table 6.4 - Construction Schedule of the CRYSTAL Storage Ring.

	1996	1997	1998	1999	2000
Magnets		• • • • • • • •	• • • • • • • •		
Power Supply		• • • •	• • • • • • • •		
Vacuum			• • • • • • • • •	• • • • • • • • •	
Electron Cooling			• • • •	• • • • • • • • •	• • • •
Laser Cooling			• • • •	• • • • • • • • •	• • • •
Injector				• • • • • • • • •	• • • • • • • • •
Diagnostic			• • • •	• • • • • • • • •	• • • •
Injection/Abort					• • • • • • • • •
Control System				• • • • • • • • •	• • • • • • • • •
Building	• • • • • • • • •	• • • • • • • • •	• • • •		
Engineering Plant		• • • • • • • • •	• • • • • • • • •		

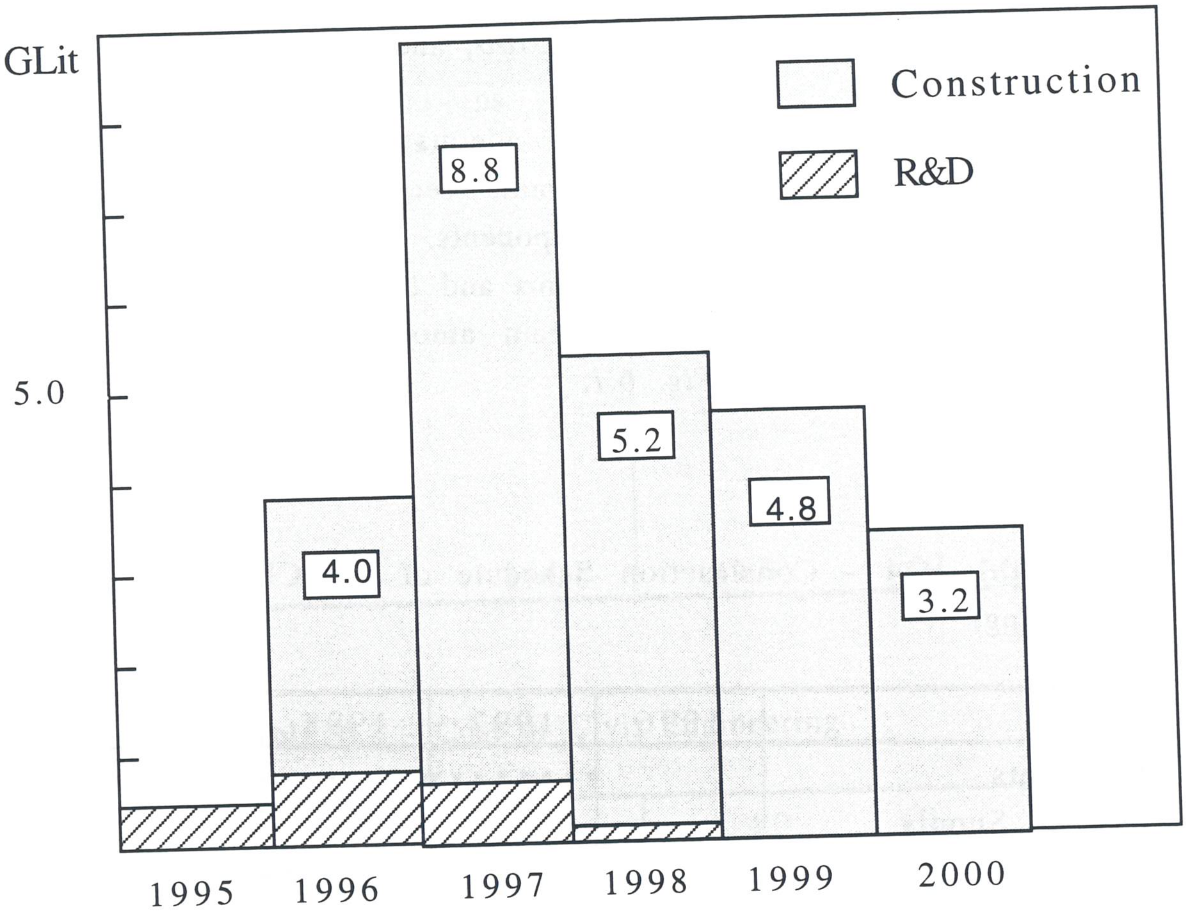

Fig. 6.1 - Funding Distribution for Construction of the CSR Project.